NOTE TO USERS

DISSERTATION

IMPACT OF SECONDARY BARRIERS ON $CuIn_{1-x}Ga_xSe_2$ SOLAR-CELL OPERATION

Submitted by

Alexei O. Pudov

Department of Physics

In partial fulfillment of the requirements

for the Degree of Doctor of Philosophy

Colorado State University

Fort Collins, Colorado

Spring 2005

COLORADO STATE UNIVERSITY

February 22, 2005

WE HEREBY RECOMMEND THAT THE DISSERTATION PREPARED UNDER OUR SUPERVISION BY ALEXEI O. PUDOV ENTITLED IMPACT OF SECONDARY BARRIERS ON $CuIn_{1-x}Ga_xSe_2$ SOLAR-CELL OPERATION BE ACCEPTED AS FULFILLING IN PART REQUIREMENTS FOR THE DEGREE OF DOCTOR OF PHILOSOPHY.

Graduate Committee

Advisor

Department Head

ABSTRACT OF DISSERTATION

IMPACT OF SECONDARY BARRIERS ON $CuIn_{1-x}Ga_xSe_2$ SOLAR-CELL OPERATION

Thin-film solar cells based on $CuInSe_2$ (CIS) absorber with a band gap of $E_g = 1.0$ eV and also based on $CuIn_{1-x}Ga_xSe_2$ (CIGS) alloy absorbers with a band-gap range of $E_g = 1.0 - 1.67$ eV are investigated in this work. Intermediate "buffer" semiconductor layers in p-n junctions of CIGS solar cells often improve photodiode properties of the devices. Several buffer-material selection criteria are discussed. The primary goal of the thesis is to study secondary barriers in the conduction band at the buffer/absorber interface, which may limit current transport and thus reduce the efficiency of the solar cells. The secondary goal is to explore potential benefits of alternative wide-band-gap buffers in CIGS cell structures. CIGS cells with standard CdS buffer layers, and alternative ZnS(O,OH) and InS(O,OH) buffer layers were studied.

$CdS/CuIn_{1-x}Ga_xSe_2$ solar cells with variable Ga content have a range of conduction-band offsets (ΔE_c) in the junction from moderately positive (spike offsets) in $CdS/CuInSe_2$ to moderately negative (cliff offsets) in $CdS/CuGaSe_2$. Large conduction-band spikes cause distortions in diode current-voltage (J-V) curves of solar cells. No CIGS-alloy forms a sufficient spike with CdS to create J-V distortions under regular white-light illumination. Even small spikes, however, can create substantial current-limiting barriers and cause J-V distortions in the dark or under "red" illumination when no photons with

energy above the buffer band gap E_g(buffer) are present. The higher barrier in this case is caused by the common heavy compensation of the buffer layer(s), such as CdS. These predictions were confirmed in experiments, in which the largest distortions in J-V measured under red light, also known as the "red kinks", were seen in CdS/CIS or low-Ga CdS/CIGS that have largest ΔE_c, but the distortions were reduced for increasing Ga concentrations in the cells as the ΔE_c decreased. The kinks were absent for cells above a certain critical Ga concentration, at which CdS/CIGS ΔE_c is near zero. The corresponding value of E_g(CIGS) at that Ga concentration was near 1.2–1.3 eV.

The value of the CIGS band gap correlates with white-light performance of these cells. It has been observed, earlier by others and also in this work, that CdS/CIGS cells with E_g(CIGS) above $\sim$ 1.2 eV are limited in their open-circuit voltage V_{oc}. Our results show additional evidence supporting an earlier study, which explained the V_{oc}-limitation by increased recombination in structures with small-spike or cliff offsets, such as high-Ga CdS/CIGS.

According to these results, the best buffer-material choice depends on Ga concentration in CIGS, since the buffer/absorber E_c-offset is important and it changes with Ga. Thus, it is unrealistic to expect a single buffer material to be the optimal match for the entire absorber-alloy range. CdS, for example, is a good buffer for CIGS with E_g $\sim 1.1 - 1.2$ eV.

$CuInSe_2$ is a good candidate for the absorber material in the bottom cells of thin-film solar-cell tandems. Since the bottom cells are exposed to practically only "red" photons, it is important that red-light J-V of CIS solar cells be distortion-free. It was shown that one approach to reduce secondary barriers in such cells is to thin the buffer layer(s). Experimental CdS/CIS cells with reduced CdS thickness demonstrated decreased amounts

of red-light J-V distortion, and the thinnest-CdS (20-nm) cells studied had little or no red kink. This principle was also confirmed on CIGS cells with alternative buffers.

Sufficient flux intensity of blue photons ($h\nu$ above E_g(buffer)) induces photoconductivity in the otherwise compensated buffers, which also results in lowering of the secondary barriers. In general, it was shown that CIGS cells with CdS, InS(O,OH), and ZnS(O,OH) buffers have a similar response to blue photons so that the J-V distortion, if present under red light, is reduced or entirely disappears with blue-light exposure. 'Blue' photons in each case are taken to mean energies above the buffer band gap.

Buffers with different band gaps absorb different fractions of solar spectrum. Using wider-gap buffers, such as InS(O,OH) and ZnS(O,OH), was shown to produce higher photocurrents in solar cells. This photocurrent improvement is a central direction in the effort of further increasing efficiencies of thin-film solar cells. Reduced photon flux absorbed in the wide-gap buffer may result in slightly slower transition between the red-kink behavior and the normal diode J-V curve in the case when a substantial E_c-spike is present. In general, however, the solar cells with all studied buffer types showed relatively quick J-V recovery with exposure to the standard solar spectrum that contains blue photons, on the order of minutes, and relatively slow relaxation to the initial J-V kink without blue light, on the order of hours.

Alexei O. Pudov
Department of Physics
Colorado State University
Fort Collins, CO 80523
Spring 2005

Acknowledgements

" 'For in him we live and move and have our being.'..."[1]

Professional collaborators

Jim. Thank you for your continuous encouragement and belief that I could achieve the set goals. For the great professional opportunities presented to me, for your scientific insight and wisdom. I appreciated your hospitality, generosity and all other support from you when I was beginning my graduate work here.

Committee. Thank you to Bob Leisure, Richard Eykholt, and Carl Wilmsen for review of the manuscript and helpful suggestions along the way.

Collaborators at other departments and institutions. Special thank you to Miguel Contreras, Falah Hasoon, and Hamda Al-Thani of the U.S. National Renewable Energy Laboratory (NREL), Prof. Nakada and other colleagues at the Aoyama Gakuin University, Japan, and Prof. Schock and other colleagues at the Institute of Physical Electronics, Germany, who prepared the solar cells described in this work. Thank you to W. Sampath, Kurt Barth, Al Enzenroth and the rest of the U.S. CIS and CdTe R&D Teams, and many others who shared their experience along the way. You have been an invaluable part in my work; thank you for your time and energy.

[1]The Holy Bible, New International Version (in English), Acts 17, vs. 28.

Other students and staff past and present. Pam Johnson, Jason Hiltner, Caroline Corwine, Samuel Demtsu, Tim Nagle, Markus Gloeckler, Alan Davies, Ana Kanevce, Karen Bockel, Jamiyanaa Dashdorj, and Bob Adame. Needless to say that this work would be impossible without your help. Caroline, thank you for taking your time to help me at the end of my thesis writing.

Thank you to the many faculty members that were instructors in the classes I took as a part of the program. I appreciated the practical 'problem-solving' approach in the classrooms that was essential. Thank you, Brian, for the great experience that I had teaching alongside with you during my first two years of graduate school.

I would also like to acknowledge my instructors at Kharkov Polytechnic Institute, Kharkov, Ukraine. You gave me a very solid background in mathematics, and physics and material science of semiconductors.

Here is to the fun times

Samuel and Jamy, I appreciated the times spent with you outside of the curriculum laughing, eating, traveling, and other things. Hunter and Karen, thank you for your continuous encouragement and friendship both inside and outside of the department walls. Tim and Ana, and also Sam, Alan, and Sangita, thank you for the fun times on Thursday afternoons at the University Club.

Friends and family outside of the department

Garrett, thank you for creating the relaxed, fun atmosphere in our place for the last two plus years. My being over-concentrated on school disappeared many a time as soon as I crossed the threshold of our apartment. Keep up the 'good jorb'.

Church. Jaime, Holly, Leora, Joey, Wes, Sara, Chad and many others, you provided me with a safe zone for all these years, helped me to re-focus on true values of life. Hans

and Ann, I am thankful for your considerate hearts and hospitality when I needed it on my arrival to the states. Darcy, Steve, Dave, Travis, Glenn, Mark and Beth, Mike and Doreen, Leroy and Nicole, Gayle... The names are too many to list and include the members of the Church of Christ here in the Fort Collins, Loveland, etc. area, and also campus ministries at CU, Boulder, School of Mines, Golden, and the Church in Denver. My friends in the Ukrainian, Russian, Georgian and other churches — you were present in my life even though I was away.

My college and high school friends and other friends. Even the memories of you and the infrequent but cherished contacts with you were a source of motivation.

Mom. Many times I wished the distance between the two countries was shorter so that I could see you and other friends and family a lot more often. These years in the graduate school, however, taught me great many things, and the chances are that without your support and encouragement I wouldn't have done it. Thank you for the many words of wisdom and love.

Contents

List of Figures

List of Tables

Chapter 1

Introduction

1.1 Role of solar cells among energy sources

1.1.1 Role of solar cells and other alternatives

Finding alternative sources of energy is a vital issue in the modern world for many reasons. One reason is that traditional energy sources like coal, gas, and oil may be depleted relatively soon. Many analysts project serious depletion will happen within several decades from now. Another reason is that from the environmental point of view, burning of fossil fuels causes air and water contamination. More importantly, however, CO_2 from fossil fuels will almost certainly increase the average temperature on the planet — the phenomenon known as the global warming.

Solar energy, wind energy, hydrogen fuel energy and other alternatives are not only renewable, but also overall more environmentally friendly. Power obtained from both wind and sun finds more and more utilization both in the U.S. and abroad.

Solar energy can be converted into electricity or utilized directly for heating. Devices

that convert solar power directly into electricity are collectively termed as the photovoltaic devices, often abbreviated as PV, or referred to as solar cells. It's been shown that solar cells covering approximately 0.4% of the U.S. land area can supply its entire energy demand. The price per kW for the PV-electricity, however, remains somewhat higher than that for the traditional energy. Despite the higher price of solar electricity, solar cells have an additional unique role in the market of stand-alone energy systems. They supply power to individual houses or even villages that are off the central power-line grid, to space stations or satellites. In addition, small solar panels are used for lighting and to power various small household appliances.

1.1.2 Role of thin-film solar cells

The highest efficiency of conversion of solar light into electricity has been demonstrated in solar cells made from single-crystal semiconductor wafers. Thin-film solar cells, though somewhat behind in efficiency, have several advantages compared to their crystalline counterparts. One advantage is cheaper manufacturing compared to the single-crystal growth that demands high energy consumption. Another advantage is the ability to deposit thin films onto large areas at the same time.

There is a wide variety of thin-film deposition techniques that gives a great flexibility to a manufacturer. The ideal manufacturing scenario would be to have a sequential deposition of all layers of a cell in-line. Thin-film solar cells whose entire thickness is $\sim 5 - 10$ μm can be deposited onto flexible substrates, e.g., metal foils or plastic films. The small total thickness plays a significant role when the total weight of solar panels is critical, as for example in space applications.

1.2 Solar-cell operation

Figure 1.1 shows measured dark and illuminated current density versus voltage (J-V) curves for a typical solar cell. The dark curve is a standard semiconductor-diode curve, and the illuminated curve is shifted down from the dark curve by the value of the photogenerated current density (J_L). The zero-voltage and zero-current intercepts on the illuminated J-V are termed the short-circuit current density (J_{sc}) and the open-circuit voltage (V_{oc}), respectively. The point on the curve with the maximum product of current-density and voltage is referred to as the maximum-power density (P_{max}), and the respective current density and voltage are called the maximum-power current density (J_{mp}) and the maximum-power voltage (V_{mp}). The fill factor (FF) of a solar cell is defined as:

$$FF = \frac{V_{mp} * J_{mp}}{V_{oc} * J_{sc}} \tag{1.1}$$

The geometric meaning of the fill factor is the ratio of the area of the smaller rectangle to the area of the larger rectangle, which are shown with dashed lines in the Fig. 1.1, and is a measure of how 'square' the shape of a diode curve is. The solar-cell efficiency is defined as:

$$\eta = \frac{P_{max}}{P_{incident\ light}} = \frac{V_{oc} * J_{sc} * FF}{P_{incident\ light}} \tag{1.2}$$

where the standard incident-light power density ($P_{incident\ light}$) commonly used is equal to 100 mA/cm^2.

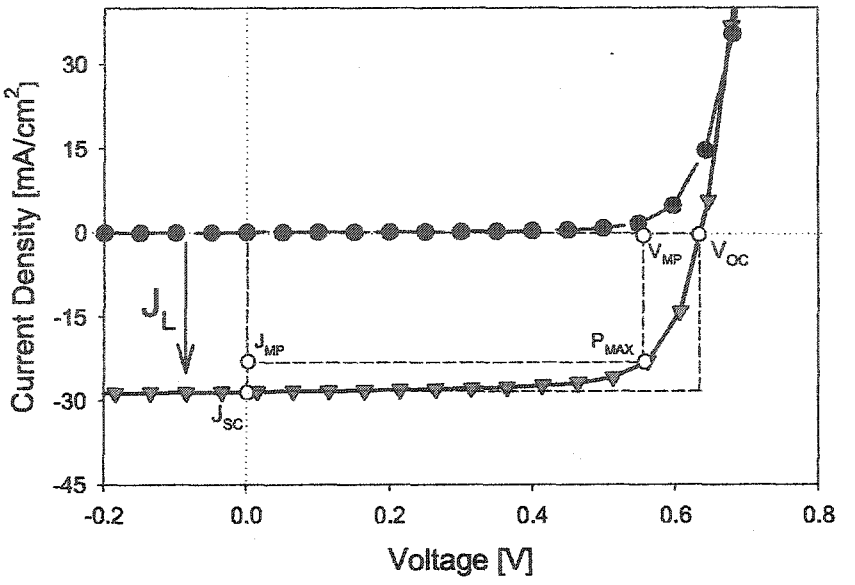

Figure 1.1: Current-density versus voltage (J-V) curve of a thin-film solar cell in the dark (circles) and illuminated (triangles).

1.3 Physical aspects of thin-film materials in PV

Unlike crystalline silicon, most of the common absorber materials for thin-film solar cells — CdTe, $CuIn_{1-x}Ga_xSe_2$ (CIGS), and amorphous silicon (a-Si) — have direct band gaps. The resulting high absorption coefficients in these materials require considerably thinner layers for the absorption of all incident photons, for example compared to the indirect-gap crystalline Si. This is a clear advantage for the material-consumption minimization during manufacturing (see *Section 1.1.2* for other advantages of small thickness).

Very high PV quality can be achieved in the film materials. Discussion, however, still continues as to the role of the grain boundaries (GB's) present in CIGS and CdTe thin films. Some scientists believe that the absorber GB's are benign, because potential barriers that repel holes are formed at the GB's and prevent recombination, making GB's 'channels' for uninterrupted current flow [5]. Experimental evidence in support of this theory was provided in Ref. [6], where increased electric currents were detected

along the GB's, compared to the bulk of the grains. Other scientists [7] propose that the fluctuations in the semiconductor properties, such as the semiconductor band gap, including at the GB's, would result in the reduced overall performance of thin-film solar cells compared to the crystalline ones.

Another important aspect of the thin-film materials used in PV is the potential existence of relatively high densities of defects. The existence of various types of defects in the same semiconductor creates a challenge in the identification and separation of the influences of each defect type on the performance.

1.4 Major sources of solar-cell efficiency losses

Early theoretical work on the limits of single-junction solar-cell efficiency was done by Shockley and Queisser in 1961 [8]. According to the theoretical calculations, most of the efficiency would be lost to temperature effects (40%) and due to non-monochromaticity of the solar spectrum (at least 30%). The remaining efficiency depends on the band gap of the semiconductor absorber. Maximum efficiency of $\sim$ 30% was predicted for solar cells with E_g(absorber) of $\sim$ 1.4 eV operating at room temperature under standard solar illumination. This is very consistent with single-crystal GaAs solar cells with near-optimum band gap ($E_g \sim$ 1.5 eV), which hold the absolute single-junction efficiency record of $\sim$ 28%.

In addition to non-optimal absorber band-gap values, real-world solar cell efficiency may be reduced by several other factors. One type of loss comes from incomplete conversion of photons incident on a cell into photocurrent. Fig. 1.2 shows an example of the Quantum Efficiency (QE) curve as a function of photon wavelength λ, which quanti-

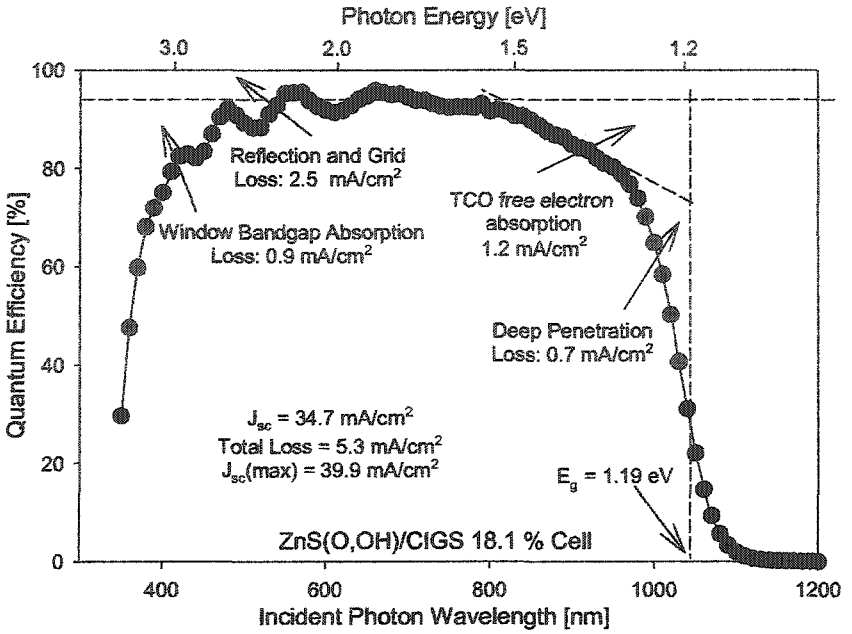

Figure 1.2: Quantum Efficiency losses due to various mechanisms [1].

fies the photons-into-current conversion efficiency, for a high-performance thin-film CIGS cell [1]. The graph shows that even for photon energies above the absorber band gap, there was a certain fraction of photons of each wavelength that was not converted into photocurrent for the various reasons shown. In terms of device parameters, such losses result in lower J_{sc}, which can be determined by the integral of the QE spectrum.

The effect of a shunt through a solar-cell diode is shown on Fig. 1.3(a). The maximum power P_{max} in this case may be significantly reduced. Whereas moderate shunts mainly reduce the FF factor of a device, large shunts will also reduce V_{oc}. Fig. 1.3(b) demonstrates the deleterious effect of high overall series resistance of the solar-cell layers on the J-V curves and P_{max}; FF is mainly affected in this case. This particular loss can be especially large in solar modules, where a large number of individual cells are connected in series.

V_{oc} can also be reduced by excess forward current resulting from electron-hole re-

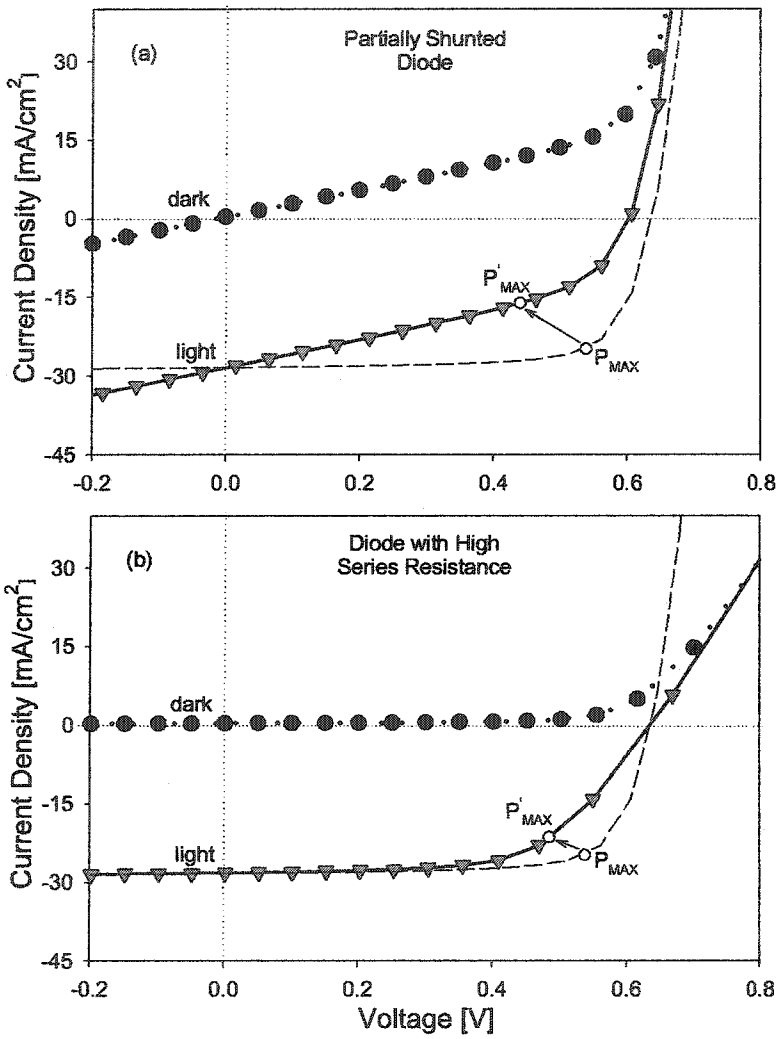

Figure 1.3: Effect of (a) diode partial shunting, and (b) high series resistance, on solar cell performance.

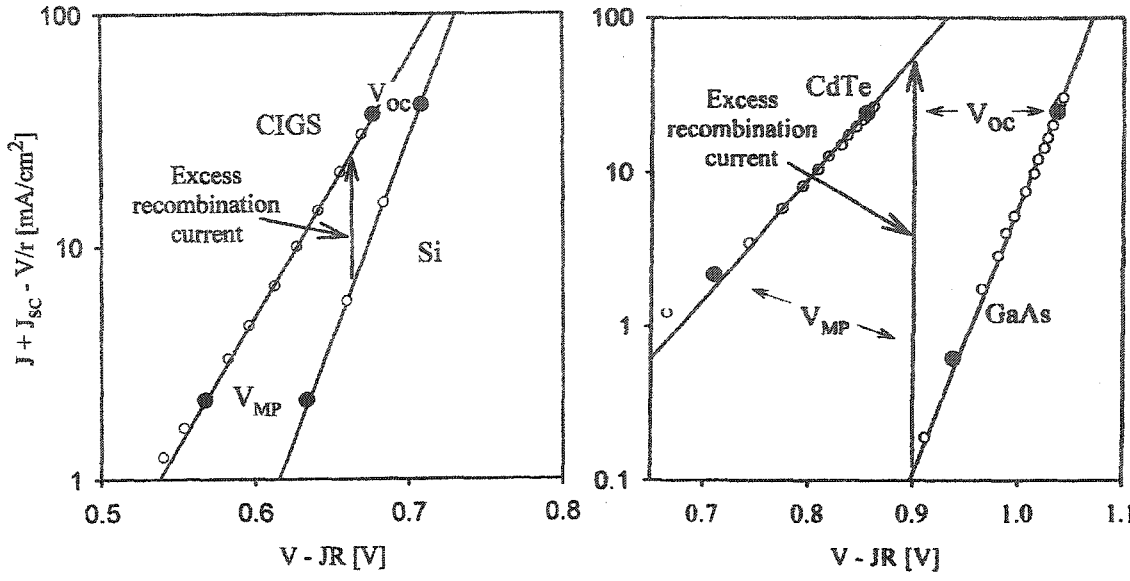

Figure 1.4: Excess forward currents in thin-film solar cells compared to their crystalline counterparts of similar band gaps [2].

combination. Fig. 1.4 from Ref. [2] shows J-V examples for high-efficiency thin-film CIGS and CdTe cells, and their single-crystal counterparts of similar band gaps, on a semi-logarithmic scale and corrected for shunt resistance r and series resistance R. The difference between the two curves on each graph indicated by vertical arrows is the excess current flowing in thin-film cells, and the corresponding horizontal difference is the voltage loss. The recombination mechanisms that cause the excess current mainly include recombination through diode depletion-region states, and states at various interfaces. For thin-film materials, the interfaces, in addition to the boundaries between adjacent layers of different materials, may also mean the grain boundaries within layers.

Existence of secondary parasitic barriers in the energy bands of solar-cell structures may also reduce cell efficiency. Whereas the problematic region where barriers form in CdTe thin-film solar cell is the back contact, in CIGS cells, the secondary barriers may form at the p-n junction.

The *following Section* highlights the content of this thesis.

1.5 Contributions of this work

The main goal of the research in the thin-film solar-cell R&D community is to further improve efficiency and long-term stability of such solar cells. Thus, a large portion of the collaborative effort is focused on the minimization of the above-mentioned and other efficiency losses.

In CIGS solar cells, utilization of certain buffer layers, the layers adjacent to the absorber, generally improves cell efficiency. However, even the best buffer-material choices for CIGS that have been implemented to-date, such as CdS, have certain drawbacks. This thesis further investigates the role of buffers layers in CIGS solar cells. In particular, the impact of buffer layers on cell performance (current-voltage curves) will be considered. The variation of the impact depending on Ga concentration in the absorber and features of different buffer types will be discussed. In both cases, the special emphasis will be given to J-V effects resulting from the conduction-band offset between the buffer and the absorber. The thesis also explores details such as the impact of buffer thickness, different temperatures, and spectral content of light. The potential improvements in CIGS efficiency with the replacement of the standard CdS buffer material by its alternatives will be evaluated.

Chapter 2 of the thesis will review CIGS solar cells and summarize previous work on CIGS cells with various buffer materials. *Chapter 3* will summarize fabrication, measurement, and simulation techniques used. *Chapter 4* will describe and discuss a large number of results of this work. Finally, *Chapter 5*, conclusions, will summarize the important information learned.

Chapter 2

Review of CIGS solar cells

2.1 CIGS-cell structure

A typical Cu(In,Ga)Se_2 (CIGS) thin-film solar cell consists of the following layers (Fig. 2.1): a metallic (Mo) back contact; a p-CIGS absorber layer, the surface of which is usually intentionally made Cu-poor; an n-type (or intrinsic) buffer layer, usually CdS; an intrinsic ZnO layer, and an n^+-ZnO transparent front contact. Metallic Ni/Al contact grids complete the cell (only one grid finger is shown). Soda-lime glass substrate is an important component since it provides sodium found to be critical for high CIGS-cell performance (see Ref. [9] on impact of Na).

Fig. 2.2 shows a typical calculated band diagram for the CIGS cell structure. The wider band gaps of the ZnO and buffer layers allow the majority of photons to be absorbed in the narrow-gap p-type absorber (CIGS). Electron-hole pairs generated by the photons in the CIGS absorber are separated by the built-in electric field in the p-n junction and contribute to cell's photocurrent. The solar cell's open-circuit voltage should be

determined by the built-in potential V_{bi} (see the graph). Thus, in a simple case, higher absorber band gaps should yield higher V_{oc} and lower J_{sc}. Electron-affinity difference at the buffer/absorber heterointerface results in a conduction band discontinuity ΔE_c. The thesis results dealing with the effects of the discontinuities on cell performance will be discussed in detail in *Sections 4.2 and 4.3.*

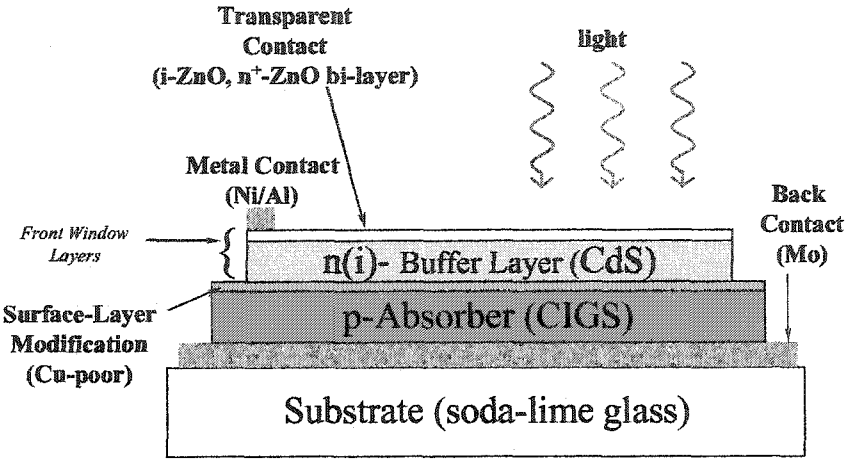

Figure 2.1: Layer structure of a Cu(In,Ga)Se_2 thin-film solar cell.

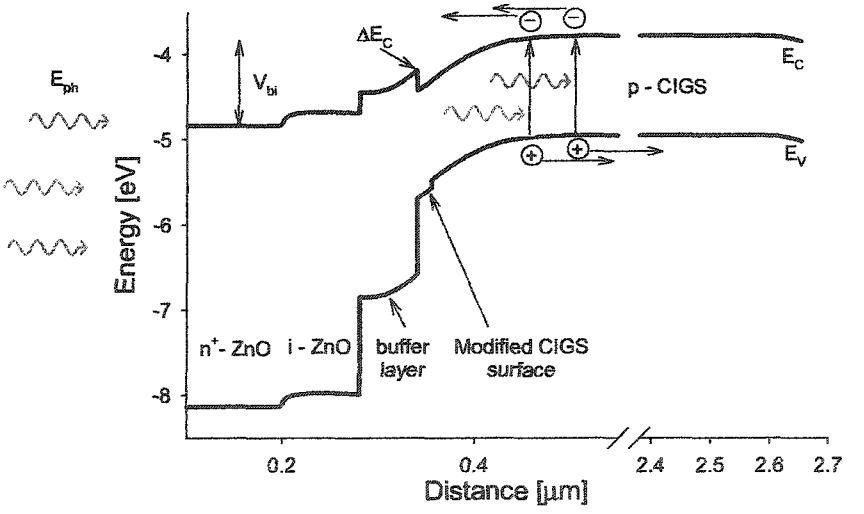

Figure 2.2: Simulated band diagram for a Cu(In,Ga)Se_2 thin-film solar cell.

2.2 CIGS absorbers

The well-known ternary $CuInSe_2$ (CIS) and its alloys are some of the most promising semiconductor absorber materials for photovoltaic applications. CIS has a direct band gap of $E_g \sim 1$ eV (0.98 eV – 1.04 eV can be found in literature), where the actual value of E_g depends on its stoichiometry. Decreased Cu concentration results in moderately increased CIS band-gap values. Compositional stoichiometry also plays a role in how well the absorber material performs in a solar cell. A few percent Cu deficiency has historically resulted in cells with the highest efficiencies, and is therefore commonly used.

As discussed in *Section 1.4*, the theoretical optimal absorber band gap for solar cells is about 1.4 eV [8]. In order to increase the CIS band gap towards the optimum, it is a common practice to add Ga or Al to CIS, keeping the overall number of group-III atoms, In + Ga or In + Al, constant. The band gaps of the resulting alloys range from 1.0 eV to 1.67 eV for $CuIn_{1-x}Ga_xSe_2$ (CIGS), and from 1.0 eV to 2.8 eV for $CuIn_{1-x}Al_xSe_2$ (CIAS). One can also achieve higher band gaps with sulfur addition to produce $CuIn(Se_{1-y}S_y)_2$ alloys. Other chalcopyrite compounds are also occasionally used in solar cells. It has been experimentally observed that neither CIGS- nor CIAS-based cells follow the theoretically-predicted efficiency increase with band gap all the way to 1.4 eV. The highest efficiencies of thin-film solar cells made to-date have $CuIn_{1-x}Ga_xSe_2$ absorbers with band gap near 1.15 eV. The *Results Chapter* investigates the reasons behind this issue.

CIGS thin films used in PV to-date have been p-type. The investigations of the majority carrier concentration in solar-cell-incorporated CIGS by various groups have shown values on the order of 10^{16} cm^{-3}. The natural doping is commonly attributed to Cu vacancies in the CIGS matrix that are shallow acceptors [10, 11].

2.3 Utility of buffer layers

2.3.1 Functions of buffer layers in CIGS solar cells

Any layer between the highly-doped n^+-ZnO transparent conducting oxide (TCO) and the absorber in Fig. 2.1 can be referred to as a "buffer" or "window"; the term "window", however, is logically extended to TCO's as well. Even though p-n junctions will form between n^+-TCO's and p-absorbers, the quality of the junctions is improved considerably with the introduction of an intermediate buffer layer(s).

The following functions are ascribed to buffer layers in thin-film solar-cell junctions. From the electronic point of view, since buffer layers are usually highly-resistive, they serve as intermediate layers that can prevent shunting between the TCO and the absorber [12]. From the technological point of view, buffer-layers can protect the absorber surface from damage by high-energy ions during the n^+-ZnO deposition by RF-sputtering (multiple papers, e.g., Ref. [13]). From the chemistry point of view, chemical constituents of buffer material passivate CIGS surface defects and/or dope the CIGS near-surface layer (see *Section 2.4.1*). And finally, from the physics point of view, buffer layers affect the band structure. Specifically, they affect the band offsets and the electric field in the junction, and thus the current transport.

2.3.2 Criteria for buffer-layer selection

Some of buffer-selection criteria follow directly from the *previous Section*. To make a good junction partner with a p-CIGS absorber, a buffer material should be n-type, or possibly intrinsic (i-type). Buffers with high resistivity are preferred to reduce the possibility of shunting of a junction. Matching the absorber and the buffer lattice constants

should also be considered when choosing a buffer. Poor matches may result in interfacial defects, which cause undesirable recombination of carriers. Technological feasibility of the incorporation of a buffer layer into the cell manufacturing process must also be considered.

One other major criterion in selection of a buffer material is its band gap (E_g). E_g needs to be sufficiently wide that as few photons as possible are absorbed in the buffer. This point is illustrated with Fig. 2.3 that shows the standardized solar spectrum, termed Air Mass 1.5 (AM1.5), in the units of photon current. The figure also shows the maximum photocurrent density (max-J_{sc}) that the light can generate in a solar cell as a function of the absorber E_g. For 1.0-eV CIS, the maximum J_{sc} is near 46 mA/cm^2, whereas it is nearly 6 mA/cm^2 lower for 1.15-eV CIGS. Note that despite the loss of current, one will still gain in efficiency by widening the absorber band gap; the efficiency increase should theoretically occur up to E_g(absorber) $\sim$ 1.4 eV [8] due to increased V_{oc}.

The max-J_{sc} calculations assume that all photons with $h\nu \geqslant E_g$(absorber) are absorbed in the absorber and all minority carriers generated are collected at the junction. Before reaching the absorber, however, the incident light first passes through the front window layers (Fig. 2.1). Photons with energies above the band gaps of those layers will be absorbed there and the generated minority carriers will predominantly *not* be collected due to their low mobilities. As seen from Fig. 2.3, the band gap of the ZnO TCO is E_g = 3.2 eV, which is nearly optimal in the sense that only a very small fraction of solar spectrum may be absorbed in ZnO resulting in photocurrent loss less than 1 mA/cm^2. CdS (E_g = 2.4 eV), however, can lower the photocurrent through absorption by up to $\sim$ 7 mA/cm^2. By making the CdS buffer layer thinner, part of the short-wavelength current loss can be recovered. Buffer-thickness variation will be discussed in *Section 4.1.2.*

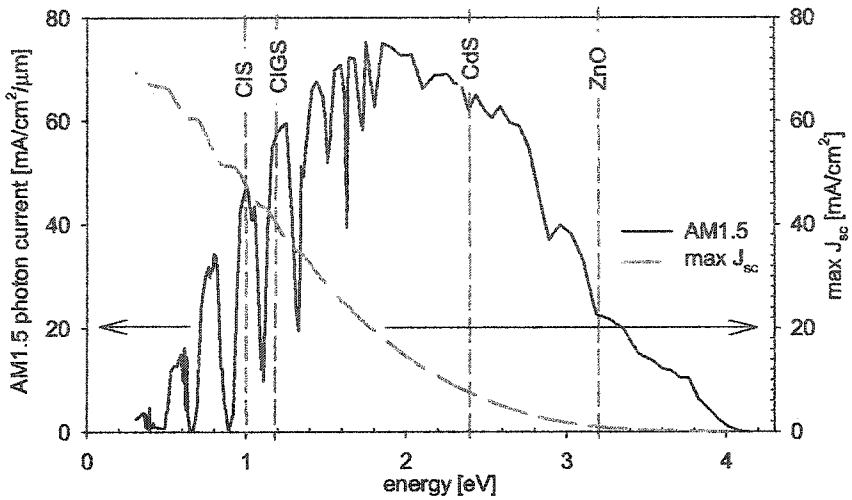

Figure 2.3: Standard AM1.5 solar spectrum; maximum attainable solar-cell short-circuit current density as a function of the absorber band gap.

Another important buffer-material selection criterion is its electron affinity χ, which will determine discontinuities in the energy bands at the buffer/absorber interfaces. A central result of this thesis deals with the positive discontinuities (spikes) in the conduction band, which cause deviations from the standard-diode behavior in solar cells.

There have been a number of various buffer materials and/or surface treatments incorporated in CIGS solar cells by various groups. Table 2.1 lists the majority of buffer materials that can be found in the literature. The *following Sections* will discuss the reported studies.

	Cd		Zn		In		Sn
	Chalcogenides						
S	CdS		ZnS		In_2S_3		
Se			ZnSe	$ZnIn_2Se_4$	In_2Se_3		
	Oxides						
O			ZnO				SnO_2

Table 2.1: Buffer materials attempted in lab-size CIGS thin-film solar cells to-date

2.4 Buffer materials used in CIGS cells

This section of the Review discusses multiple papers on utilization of different buffer layers in CIGS thin-film solar cells. In addition to the numbered references, a complete list of references for this section is located on page 104. The graphs in this section contain abbreviations for the names of the institutions where the reviewed research was conducted and the abbreviations for the names of the buffer-deposition methods. The list of the abbreviations is located at the end of the chapter on page 25.

2.4.1 CdS

Cadmium sulfide is a well-known material for photovoltaic applications. Record efficiencies of up to 19.3% [14] have been achieved in laboratory-scale CIGS cells with CdS buffer layers prepared by the chemical-bath deposition (CBD). Most CIGS solar modules made recently include the CdS layer.

However, there are some disadvantages to CdS. As discussed in *Section 2.3.2*, using wider-band-gap alternatives would be more favorable from the point of view of recovering short-wavelength photocurrent. From the environmental point of view, use of cadmium in mass-produced devices has a certain opposition from the public due to the toxicity of Cd. As for manufacturing, depositing CdS by the CBD method, most successful for making high-efficiency devices to-date compared to other techniques, typically involves significant amounts of waste.

The superior performance of CIGS cells with CdS buffer layers prepared by the CBD method was explored by K. Ramanathan et al. [15]. This group concluded that both sulfur and cadmium atoms favorably influence the surface or near-surface chemistry of

CIGS. Sulfur was suggested to passivate surface defects, and cadmium atoms were seen to diffuse into the near-surface region of the CIGS film resulting, as suggested, in additional defect passivation and/or n-type doping. Experiments were carried out, in which cells were made with CIGS surfaces treated in a partial electrolyte (PE) bath, containing only cation (Cd) species. Such treatment is sometimes referred to as Cd-PE treatment. A similar experiment was done with a partial electrolyte bath containing Zn atoms instead, which belongs to same chemical group as Cd. For both Cd-PE and Zn-PE treatments, Cd or Zn atoms were detected in the bulk (near-surface) region of CIGS close to the surface. One should note that devices without a buffer layer or a CIGS-surface treatment usually perform poorly. In cases of both Cd and Zn, the performance of PE-treated devices closely approached that of the comparison CdS device.

2.4.2 ZnO, Cd-PE, Zn-PE

Figure 2.4 (page 22) shows the progress in increasing of the efficiency of CIGS solar cells without buffer layers, but with the intrinsic-ZnO layer however, for the past decade or so. In the earlier years, the best CIGS cells without buffer layers had efficiencies that were typically considerably lower than those of comparison CdS cells. As discussed in the *previous Section*, the work of Ramanathan et al. (Ref. [15] and other publications) showed that the CIGS-surface treatment with Cd- or Zn- Partial Electrolytes increases the overall cell performance even though a separate buffer layer is not formed. The two bars on the right-hand side of the histogram where PE-treatments or similar principles were used show not only the overall increased performance of such cells, but also smaller difference with the CdS-cells performance. Despite the increased short-wavelength currents in these

cells due to the absence of a CdS layer, their V_{oc}-values are typically somewhat reduced compared to CdS devices.

2.4.3 ZnS(O,OH) and CdZnS

The wide band gap of ZnS (E_g = 3.8 eV) makes this material an attractive buffer from the perspective of short-wavelength current. However, the very high positive conduction-band offset (ΔE_c) that it forms with CIGS (near +1.4 eV, measured [16] and calculated [17]) poses a serious problem. Cd-PE and Zn-PE experiments mentioned above, along with studies on influence of sulfur on CIGS, rekindled interest in this option recently. Solar cells made with nominal ZnS via the CBD method by several groups showed (Fig. 2.5, page 22) quite a respectable performance, including the 18.6% alternative-buffer CIGS record [18]. Secondary zinc oxide and hydroxide phases in CBD-ZnS, however, were detected [19] in very large quantities in such cells. These compounds, which clearly alter properties of the thin film, have much lower E_c-offsets with CIGS giving a possible explanation for the discrepancy between the high performance of ZnS(O,OH)/CIGS and a large ΔE_c for pure-ZnS/CIGS. Additionally, ZnS can be unstable in an oxygen atmosphere and ZnO is formed when sufficient energy is provided [20].

Mixed CdZnS buffer materials have also been used for solar cell preparation. All reported buffers were prepared by chemical-vapor deposition techniques (Fig. 2.5), which are known to yield inferior junction quality due to non-uniform coverage of the absorber surface with the buffer material and also other reason. Thus, reported efficiencies of CdZnS/CIGS cells have barely exceeded 10% [21–23].

2.4.4 ZnSe and $ZnIn_2Se_4$

Figure 2.6 (page 23) shows the efficiency summary for CIGS cells with ZnSe and $ZnIn_2Se_4$ buffers made by various groups. Several ZnSe studies reported cell efficiencies as high as 14%, and the study done at Hahn-Meitner showed the efficiency for ZnSe cells approaching that for the CdS reference cells made with the same absorber. The studies showed that ZnSe band gap of $E_g = 2.67$ eV leads to photocurrents higher than those for comparison CdS cells; however, obtained ZnSe-cell voltages were inferior. $ZnIn_2Se_4$ has relatively low band gap of ~ 2.0 eV [12] for an ideal buffer-material candidate. Results from one of the two studies on $ZnIn_2Se_4$ shown in Fig. 2.6, however, were especially interesting. In that study, the buffer was deposited in the same vacuum cycle as (in-line with) the CIGS absorber, and the 15% efficiencies were achieved. The reason for the good result is the close lattice-matching between the absorber and the buffer in this case, and the non-exposure of the absorber surface to air prior to the buffer deposition. Despite the low band gap of $ZnIn_2Se_4$, its use in the in-line deposition process was thus demonstrated to be promising.

2.4.5 In_2S_3, In_2Se_3, $In(OH)_xS_y$

Figure 2.7 (page 23) shows the efficiency overview based on several recent studies for CIGS cells with In-containing buffers. The band gap of crystalline β-In_2S_3 found in the literature is near 2.0 eV (see discussion in [24]). Ref. [24] also reported cells with efficiencies as high as 13.5% where the band gap of the buffer "In_2S_3"-compound was near 3.2 eV, which was attributed to quantum-size effects since the material was amorphous. It can be seen from the histogram that preparation of In_2S_3 via physical vapor deposition

(PVD), which is a "harder" deposition method, yielded cells with lower efficiencies than those for the CIGS solar cells with indium-sulfide buffers by atomic layer epitaxy (ALE), a "softer" method. The right side of Fig. 2.7 shows results with the In-S buffers, which also incorporated hydroxy phases. The best efficiencies were as high as 14.8% [25], and the band gap of such multi-phase buffer material was near 2.7 eV. According to the reports on cells with 1.8-eV In_2Se_3 buffers, their efficiencies reached as high as 13.3% [12]. Such cells have low photocurrents due to the low buffer band gap.

2.4.6 Alternative TCO's and superstrate structures

Figure 2.8 (page 24) shows the cell-efficiency results with miscellaneous cell structures. In Ref. [26], it was suggested that the electron affinity of ZnO transparent conductive contacts (TCO) is not ideal for the best performance of CIGS cells, and (Mg,Zn)O alloys were proposed instead. Early results using the combination of (Mg,Zn)O TCO's and ZnS(O,OH) buffers yielded efficiencies as high as 16% [26]. The ideas of alternative TCO's continue to be developed. SnO_2 with the wide band gap of $\sim$ 4.0 eV, typically considered as a TCO, is another potential candidate for a buffer material. Solar cells with such buffers, modified with sulfur inclusion, showed moderate efficiencies (Fig. 2.8). More research, however, is needed with this buffer. Finally, CIGS cells in the superstrate configuration were attempted, in which the layer-deposition sequence is the reverse of that shown in Fig. 2.1. Fig. 2.8 shows two such attempts using CdS buffer, in which the cell efficiencies were fairly low resulting from low junction quality due to the subsumption of CdS, deposited first, by the absorber, deposited next at considerably higher temperatures.

According to this summary, utilization of junction buffer layers can be beneficial in CIGS solar cells, though several issues are a key to a successful buffer-material choice. Among the main selection criteria are the band gap, resistivity, lattice matching with the absorber, buffer/absorber conduction-band offsets, chemical constituents of the buffer, and manufacturability. In addition, it is important what buffer-deposition technique is used. While deposition of buffer materials by hard methods, such as thermal evaporation, RF-sputtering etc., generally results in poorer solar cells, wet deposition techniques, such as chemical bath deposition, consistently result in high efficiencies.

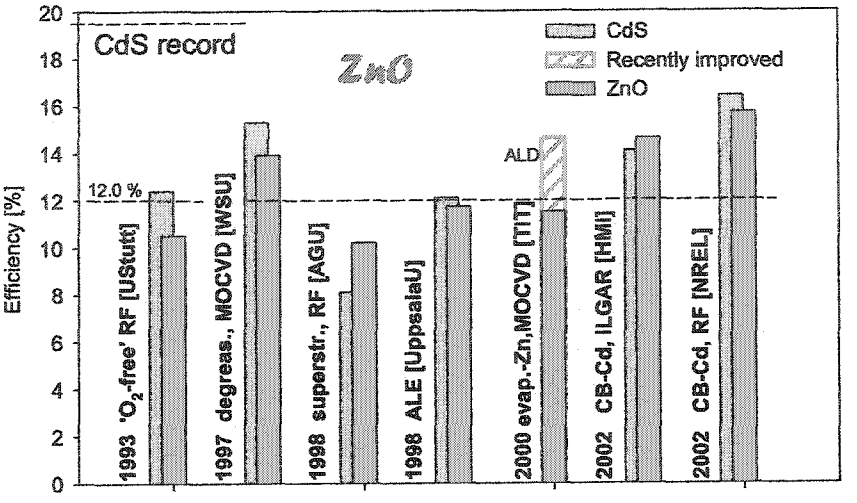

Figure 2.4: CIGS-cell efficiencies achieved with ZnO contact and no additional buffer.

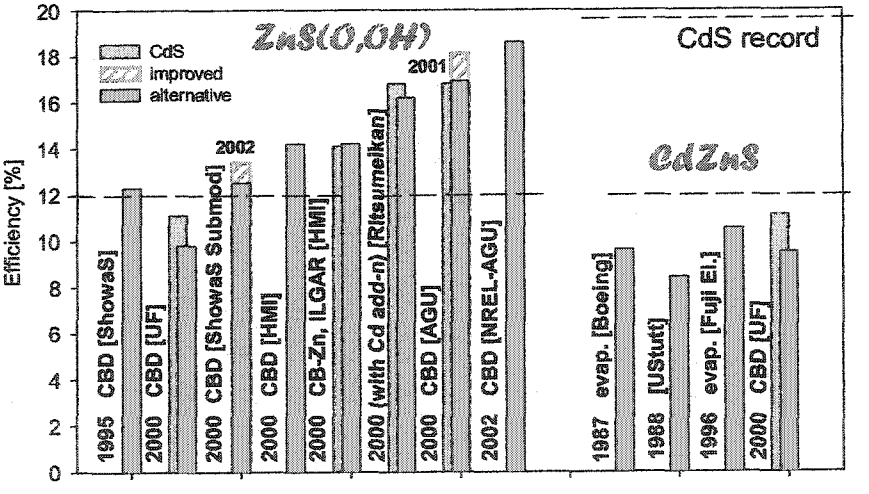

Figure 2.5: Efficiency of CIGS cells with ZnS(O,OH) and CdZnS buffers.

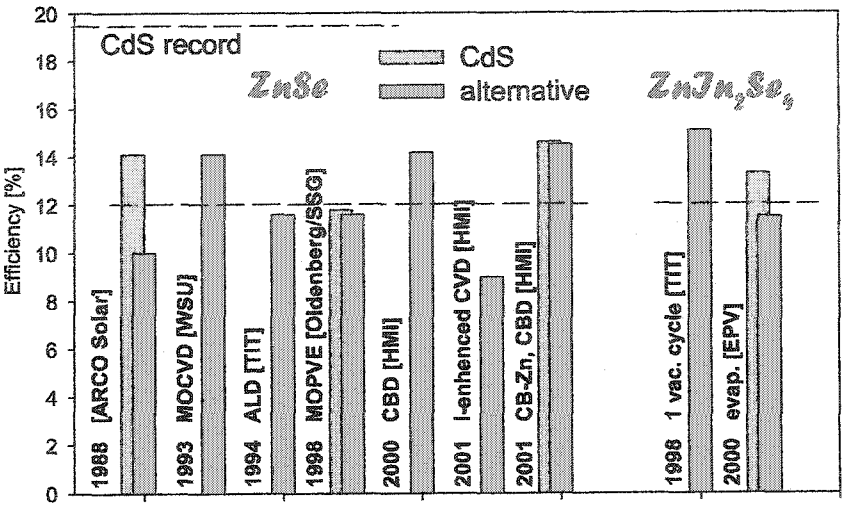

Figure 2.6: Efficiency of CIGS cells with ZnSe and $ZnInSe_2$ buffers.

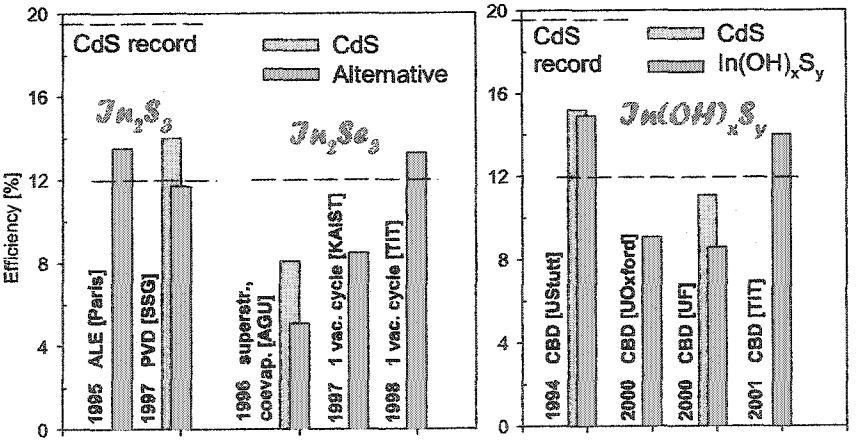

Figure 2.7: Efficiency of CIGS cells with InS, InSe, and $In(OH)_xS_y$ buffers.

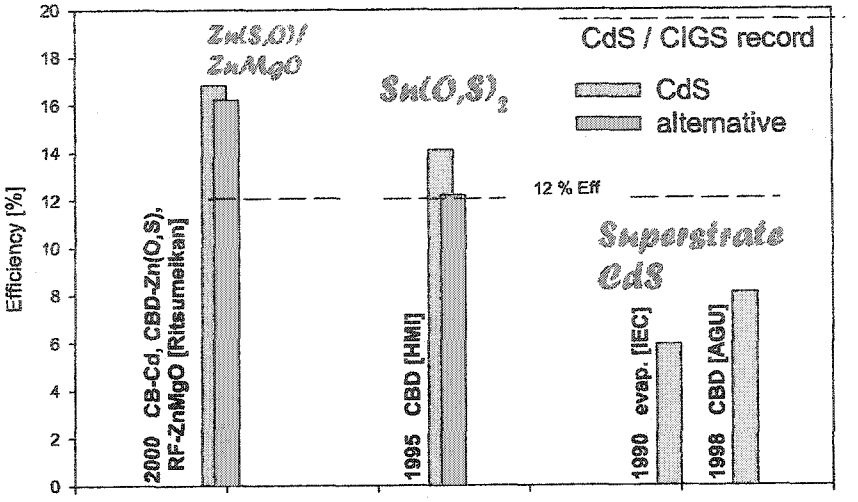

Figure 2.8: Efficiency of CIGS cells with Zn(S,O)/ZnMgO, $Sn(O,S)_2$ buffers and cells with CdS in the superstrate configuration.

Abbreviations for histograms in *Section 2.4*:

Institutions

AGU – Aoyama Gakuin University, Japan

EPV – Energy Photovoltaics, Inc., USA

Fuji El. – Fuji Electric, Japan

HMI – Hahn-Meitner Institute, Germany

IEC – Institute of Energy Conversion, USA

KAIST – Korea Advanced Institute of Science and Technology

NREL – National Renewable Energy Lab, USA

Ritsumeikan – Ritsumeikan University, Japan

ShowaS – Showa Shell Sekiyu K.K., Japan

SSG – Siemens Solar Gmbh., Germany

TIT – Tokyo Institute of Technology, Japan

UF – University of Florida, USA

UOxford – University of Oxford, GB

UppsalaU – University of Uppsala, Sweden

UStutt – Stuttgart University, Germany

WSU – Washington State University, USA

Deposition techniques

1 vac. cycle – single vacuum cycle with CIGS

ALD – Atomic Layer Deposition

ALE – Atomic Layer Epitaxy

CB(D) – Chemical Bath (Deposition)

CVD – Chemical Vapor Deposition

ILGAR – Ion Layer Gas Reaction

MOCVD – Metal Organic Chemical Vapor Deposition

MOPVE – Metal Organic Pressure Vapor Epitaxy

RF – Radio-frequency magnetron sputtering

Chapter 3

Description of experiments

3.1 Preparation of cells

This section of the experiment description summarizes the manufacturing of the cells studied. Most CIGS cells with the CdS buffer layers were fabricated at the U.S. National Renewable Energy Laboratory (NREL). For the ZnS(O,OH)/CIGS cells, the ZnS(O,OH) buffer layers were deposited at Aoyama Gakuin University (AGU), Japan, and all other layers were deposited at NREL. For the InS(O,OH)/CIGS cells, the buffer layers were deposited at the Institute of Physical Electronics (IPE), Germany, absorbers were deposited at NREL and IPE, and all other layers were deposited at NREL. For all cells described in this thesis, the 3"× 3" soda-lime glass substrates were used for the absorber deposition. They were then cut into approximately 1"× 1.5" pieces for the deposition of all subsequent thin layers. Individual cells on each substrate were delineated by mechanical or laser scribing, and the cells had the area of approximately 0.41 cm^2.

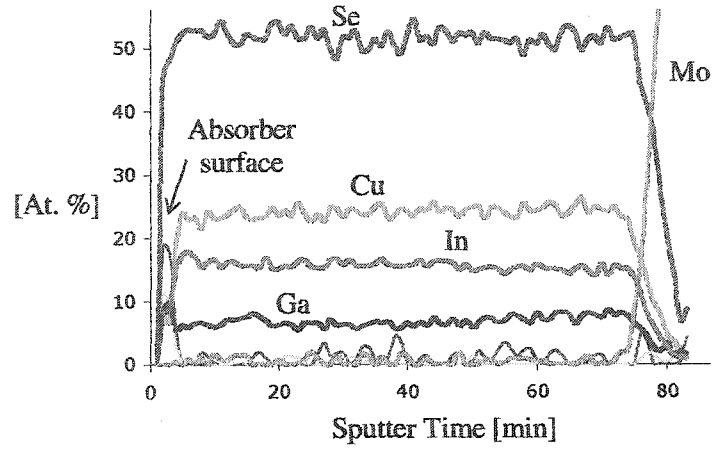

Figure 3.1: The profiling of chemical constituents through the thickness of a CIGS absorber (~ 30% Ga) by Auger Electron Spectroscopy [3].

3.1.1 $CdS/CuIn_{1-x}Ga_xSe_2$ (x = 0 to 1)

For these cells, $CuIn_{1-x}Ga_xSe_2$ (CIGS) absorbers with variable Ga concentration were deposited on Mo-coated soda-lime glass by the simultaneous thermal co-evaporation of the four elements (single-stage method); the substrate temperature was kept constant at ~ 580°C throughout the deposition cycle. The Cu/(In + Ga) (or Cu/III) ratio in the absorbers was near 0.9. The Ga component of the group-III elements was varied from 0 to 100% on a series of substrates. The chemical composition of the absorbers was determined using the Inductively-Coupled Plasma (ICP) technique. Auger Electron Spectroscopy (AES) indicated relatively uniform composition throughout the thicknesses of all CIGS absorbers [3], as illustrated for a ~ 1.15-eV CIGS absorber in Fig. 3.1. Approximately 50-nm CdS buffer layers were deposited unto all absorbers at 65°C by the chemical-bath deposition (CBD) process described in [27]. The cells were completed with the standard NREL ZnO bi-layer (~ 100 nm undoped, and ~ 120 nm Al-doped TCO) and Ni/Al grids. After the first round of measurements, the cells were given an air-anneal at 200°C for two minutes and a MgF_2 antireflection (AR) coating.

3.1.2 $CdS/CuInSe_2$ (variable CdS thickness)

For these cells, $CuInSe_2$ absorbers with $E_g = 1.0$ eV were deposited on Mo-coated soda-lime glass by the single-stage process described above and by the NREL three-stage process [28]. In the three-stage process, the metal atoms are evaporated in Se overpressure during all three stages. In the first stage, In (or In + Ga for CIGS) is evaporated onto the substrate at $T_s = 350°C$. In the second stage, Cu is evaporated at $T_s = 550°C$. When the overall slightly Cu-rich film composition, compared to the CIS (or CIGS) stoichiometry, is reached, the Cu source is turned off and an additional amount of group-III element(s) is deposited to make the final composition slightly Cu-poor (typically Cu/III $\sim$ 0.9). CdS layers of $\sim$ 20 nm, $\sim$ 50 nm, and $\sim$ 80 nm thickness were deposited onto the CIS absorbers by CBD. The cells were completed with ZnO bi-layers and Ni/Al contact grids as described in *Section 3.1.1.* These cells as well were subjected to a 2-min 200°C air-anneal after initial measurements.

3.1.3 $ZnS(O,OH)/CuIn_{1-x}Ga_xSe_2$ ($x \sim 0.3$)

Absorbers for these cells were prepared by the three-stage deposition method [28] summarized in *previous Section.* These absorbers, unlike the ones previously described, had a gradient of Ga/III ratio through the absorber thickness. Ga concentration (and E_g) was smallest ~ 0.3 μm from the diode junction. The concentration increased towards the junction, but it increased a larger amount towards the back of the absorber [29]. ICP showed the average Ga concentration of the absorber (Ga/III) was about 0.3. Nominal zinc sulfide buffer layers $\sim$ 100 nm thick were deposited onto the absorbers by CBD described in detail in Ref. [19]. XPS-analysis of similar films also described in Ref. [19]

showed inclusion of ZnO and $Zn(OH)_2$ phases, and thus the notation for the multi-phase material "ZnS(O,OH)". A 10-min 200°C air-anneal followed the CBD step. The cells were then completed with a ZnO bi-layer and Ni/Al grids as above. In addition, a layer of MgF_2 was applied as an anti-reflective coating. After an initial round of measurements, the complete devices were annealed for two minutes at 200°C in air.

3.1.4 InS(O,OH)/$CuIn_{1-x}Ga_xSe_2$ ($x \sim 0.3$)

The absorbers for the cells described in this section were also deposited by the three-stage process at NREL [28] and in some cases at IPE [30]. The Ga/(In + Ga) ratio in all absorbers was again $\sim$ 0.3, and the Cu/(In + Ga) ratio was $\sim$ 0.9. The first type of buffer layers, $\sim$ 50-nm CdS, was deposited onto the absorber by CBD [27] at NREL. The second buffer type, $\sim$ 20-nm InS(O,OH) [31], was deposited at IPE. Additionally, a thin CdS [32] layer was deposited on top of the InS(O,OH) at IPE in a few cases to create the third combined buffer type. To complete the cells, a 100-nm i-ZnO layer and 120-nm n^+-ZnO:Al layer were deposited by magnetron RF-sputtering, and Ni/Al grids were added for these cell types, as in *previous Sections*. Additional InS(O,OH)/CdS cells were finished with a double or no i-ZnO layer.

3.2 Measurement methods

3.2.1 Current – Voltage

A schematic of a current-voltage measurement circuit is shown in Fig. 3.2. A Keithley voltage source was used to apply voltages to a solar cell, typically from –0.5 to +1.0 V

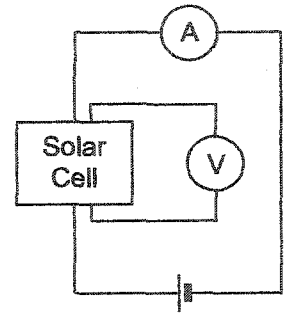

Figure 3.2: Current – voltage measurement circuit.

in 0.03-V increments. The actual voltage across the cell was measured with a Hewlett Packard multimeter, model 34401A. Another multimeter of the same type was used to measure current flowing through the cell.

Computer software controlling the measurements was designed by Jason Hiltner in 1998. The current J-V measurement set-up, or "the light box", was designed and built by Pamela Johnson in collaboration with CSU technical staff in 2002. A two-inch solar simulator was subsequently added to the set-up by Samuel Demtsu.

Standard J-V measurements were conducted at the room temperature (+25°C). In the current setup, the temperature is controlled by blowing cold nitrogen gas across the sample substrates. Maximum detected temperature gradients across 1.5" sample substrates were $\sim$ 2 K; the thermocouple, however, was usually placed in the immediate proximity of the measured cell. Two standard illumination conditions were used for J-V: no illumination (dark measurement), and 100 mA/cm^2 white-light illumination. The standard illumination was achieved with a solar simulator, Solar Light Co., model XPS 400. Both the standard global solar spectrum (AM1.5) [33], and the simulated light spectrum are shown for comparison in Fig. 3.3.

J-V was also measured under "red-light" illumination conditions. Fig. 3.4(a) shows the full white-light and partial red-light spectra in more conventional units of photon

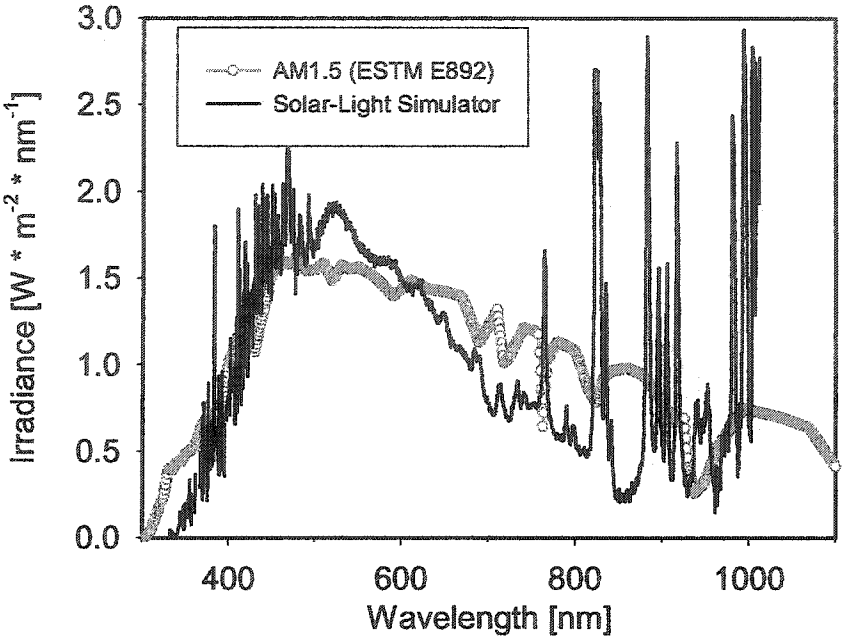

Figure 3.3: The AM1.5 outdoors solar spectrum, and the simulated spectrum.

current. The latter spectrum is attained with a filter that transmitted only light with wavelength greater than 600 nm; its transmittance is also shown. Besides the 600-nm filter, a series of filters with variable cut-off wavelengths (examples shown in Fig. 3.4 [b]) was used in some cases.

3.2.2 Current – Voltage – Temperature

J-V measurements at a series of temperatures, typically between –35 and +45°C (J-V-T), were conducted for more detailed analysis. A portion of the J-V-T measurements were taken according to the traditional procedure, in which both illuminated and dark J-V were measured at each temperature in one temperature cycle. Section 4.3 will show that such measurement procedure will likely mix temperature effects and photo-induced effects. Therefore, an alternative procedure was employed to separate these two factors. Two temperature cycles were used, in which the J-V measurements were taken (1) prior

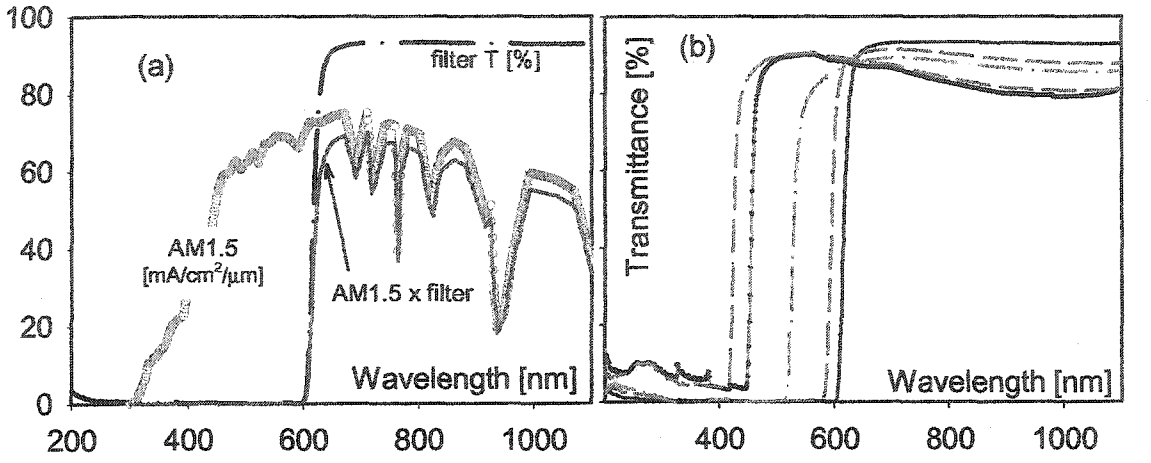

Figure 3.4: (a) AM1.5 outdoors sun-light spectrum, a 600-nm filter, and the reduced spectrum; (b) filters with various cut-off wavelengths.

to, and (2) after exposures of the test cells to photons with energies above the buffer band gap.

3.2.3 White-light exposure and relaxation

The performance of the cells described in this work was often affected by the photoconductivity of their buffer layers. Therefore, different diode characteristics were sometimes observed depending on whether or not the photons with energies above the buffer band gap were available in the illumination spectrum (thus the need for red-light J-V). To estimate the rates at which the high-energy photons effect cell diode characteristics, series of J-V curves were measured during cell exposures to short-wavelength photons of various duration and intensity. The standard approach was to measure red-light J-V curves subsequent to white-light exposures of increasing duration. Post-exposure J-V curves as a function of time without blue photons were also measured.

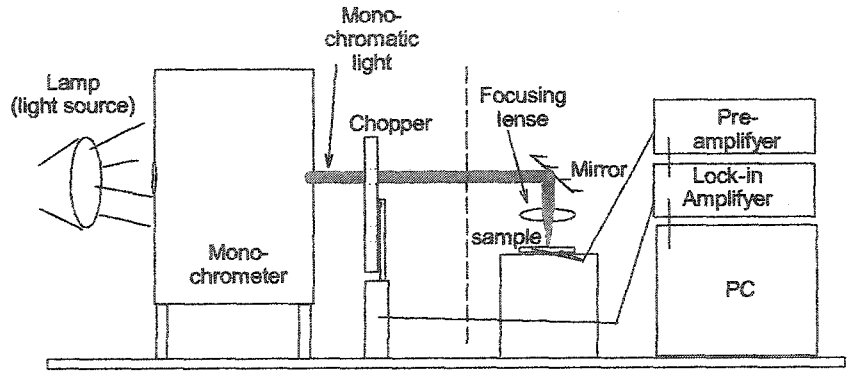

Figure 3.5: Schematic drawing of the quantum efficiency measurement.

3.2.4 Quantum efficiency

Quantum efficiency (QE) of a solar cell at a certain wavelength is defined as:

$$QE(\lambda) = \frac{N_{photons}(\lambda)}{N_{coll.\ carriers}} \tag{3.1}$$

where $N_{photons}$ is the number of incident photons of certain wavelength λ, and $N_{coll.\ carriers}$ is the number of carriers produced by the photons that are collected at the p-n junction.

Quantum efficiency was measured by the standard technique (Figure 3.5), in which chopped monochromatic light of variable wavelength was incident on the cell. The current signal generated by the light was detected with a lock-in amplifier and compared to that of a calibration cell with known QE. Monochromatic light was produced by passing integral light from a halogen bulb through an Acton Research Corp. monochrometer. White unchopped "bias" light (not shown) was added during some measurements to hold the cell near its standard operation conditions.

3.3 Parameters in numerical simulations

Numerical simulations of CIGS solar cells were carried out by using the one-dimensional simulation software "AMPS-1D" developed at Pennsylvania State University and Electric Power Research Institute by S. Fonash et al. The software is designed to simulate various photonic semiconductor structures, such as solar cells and photodiodes, and has the ability to introduce illumination with a defined photon spectrum and the electric biasing. The output data is generated through the numerical solution of the Poisson's equation for the charge distributions in semiconductor structures, and two continuity equations for the electron and hole currents flowing through the structures.

The layer structure of the simulated devices was very similar to one shown in Figs. 2.1 and 2.2, although the modified Cu-poor CIGS-surface thin layer was omitted due to insufficient information about its properties. The basic parameters for the four cell layers of the CdS/CIGS structures used in simulations are shown in Table 3.1. They are: layer thickness, dielectric constant ϵ, mobility for electrons and holes μ_e and μ_h, carrier concentration n or p, band-gap energy E_g, conduction- and valence-band density of states N_c and N_v, and electron affinity χ. Some of the listed values are reasonably well known from theoretical and experimental publications. Among the less-known are the carrier mobilities and densities of states. Although the less-known μ_e, μ_h, N_c, and N_v are important and will have an impact on the individual curves in the simulated results, they do not influence qualitatively the overall trends that will be presented. Several key parameters were systematically varied: carrier concentrations for the two middle layers n(i)-ZnO and CdS; CIGS and buffer band-gaps; conduction-band offsets ΔE_c between CdS and CIGS; and the properties of mid-gap acceptor states in CdS buffers. Simulation

results that complement the experimental results will be discussed in the *Results Chapter, Sections 4.2 and 4.3.*

Layer	1- n+ZnO	2- n(i)ZnO	3- CdS	4- CIGS
Parameters				
Thickness [nm]	200	80	60	2300
ε	9	9	10	13.6
μ(n) [cm^2/Vs]	50	50	6	300
μ(p) [cm^2/Vs]	5	5	3	30
n or p [1/cm^3]	n: 1.7E+19	n: 5E+16	n: 6E+16	p: 1.8E+16
Eg [eV]	3.3	3.3	2.4	1.04
Nc [1/cm^3]	1.00E+19	1.00E+19	1.00E+19	3.00E+18
Nv [1/cm^3]	1.00E+19	1.00E+19	1.60E+19	1.50E+19
CHI [eV]	3.9	3.9	3.75	4.05

Table 3.1: General layer parameters used for numerical simulations

Chapter 4

Results and Discussion

This chapter discusses results from the measurements of four sets of CIGS solar cells, including structures with various Ga concentrations in the absorber and with several different choices of the buffer material. The first section of the chapter describes the basic characterization of the devices: the standard dark and white-light current-voltage (J-V) measurements, white-light J-V at various temperatures (J-V-T), and standard quantum efficiency (QE) measurements. The second section will explore the effects of the conduction-band offsets at the buffer/absorber interface that form secondary barriers. The experimental data from the standard white-light J-V measurements will be compared in that section to the red-light J-V data, which reveals the impact of barriers more effectively. QE and J-V-T measurements under various illumination conditions, and numerical simulations will complement the discussion. The third section will emphasize the importance of the "blue" photons in the illumination spectrum. Transitions in the J-V curves of CI(G)S cells from highly-distorted to well-behaved as a result of blue-photon exposure, as well as the reverse transitions, will be explored.

4.1 Solar-cell performance

This section has several goals. One goal is to provide information on basic performance parameters (J_{sc}, V_{oc}, FF, η) of the studied solar cells. The second goal is to explore the benefits of the utilization of the wide-gap InS(O,OH) and ZnS(O,OH) buffers in place of traditional 2.4-eV CdS. The third goal is to begin a more in-depth analysis of the current transport in certain CIGS-cell structures. In particular, the effect of Ga concentration on the diode properties of CdS/$CuIn_{1-x}Ga_xSe_2$ cells will be studied; performance and diode properties of the hight-efficiency CdS/CIGS and ZnS(O,OH)/CIGS solar cells will be compared. The forth goal is to determine the basic parameters of the layers in the solar cells under study, such as the absorber band gaps, thicknesses of the buffer layers, etc. In particular, CIGS band gaps and the CdS thickness will be determined for CdS/$CuIn_{1-x}Ga_xSe_2$ cells with variable Ga concentrations in the absorber. The thickness of CdS layers will be determined for the CdS/CIS cells with variable CdS thickness. Absorber band gaps will be determined for the CIGS cells with alternative ZnS(O,OH) and InS(O,OH) buffer layers.

4.1.1 CdS/CIGS cells with variable Ga in CIGS

Figure 4.1(a) shows measured white-light J-V curves for the CdS/$CuIn_{1-x}Ga_xSe_2$ cells, described in *Section 3.1.1*, that had Ga concentrations covering the full range from 0 to 1 in CIGS absorbers. Band gaps of variable-Ga CIGS were determined from the quantum efficiency (QE) curves of the cells shown in Fig. 4.1(b). They were calculated from each curve's long-wavelength falloff, specifically the wavelength, at which QE was near 30%. The shift of the "infra-red" QE falloff towards higher energies (lower wavelengths) with

increasing Ga concentration was expected from the increase in E_g(CIGS). For the set of absorbers shown in Fig. 4.1, the increase of E_g with Ga concentration was fairly linear (Fig. 4.2). The primary effects of the absorber band gap increase on the J-V curves in Fig. 4.1(a), consistent with the discussion in *Section 2.3.2*, were the decrease of the short-circuit current density J_{sc} and the increase of the open-circuit voltage V_{oc}.

The solar-cell performance parameters J_{sc}, V_{oc}, FF, and η were determined from the J-V curves of Fig. 4.1; they are shown as a function of Ga concentration in Fig. 4.3. The appearance of the trends in the parameters would be very similar if the data were plotted as a function of CIGS E_g according to the linear dependence of E_g on Ga/(Ga + In) from Fig. 4.2. J_{sc} decreased relatively linearly with Ga concentration. V_{oc} tracked the Ga-concentration increase only up to x $\sim$ 0.3. Above x $\sim$ 0.3 ($E_g \sim 1.2$ eV), V_{oc} began to level out and eventually approached a saturation value of $\sim$ 780 mV. The anomalous saturation behavior of V_{oc} has been previously observed both in $CuIn_{1-x}Ga_xSe_2$ cells [34–37], and in $CuIn_{1-x}Al_xSe_2$ cells [38, 39]. FF was $\sim$ 73 – 74% for most Ga concentrations, but was slightly lower for the CIS and the $CuGaSe_2$ (CGS). After the cells received both the 2-min 200°C air-anneal and the AR-coating application, J_{sc} improved by 2–3 mA/cm^2 and V_{oc} increased a small amount for all Ga concentrations. For the cells with Ga concentrations between x = 0 and 0.5, a small FF increase was also observed. Thus, the absolute-efficiency increase from annealing and AR coating was $\sim$ 2% for most CIGS absorber compositions. The CGS cell acquired some shunting and, as a result, its efficiency did not improve with the post-deposition treatments. The highest efficiency of 16.3% was achieved for the cell with approximately 35% Ga. The optimal Ga concentration is similar to that reported by others.

Returning to the quantum efficiency curves in Fig. 4.1(b), each as-measured QE was

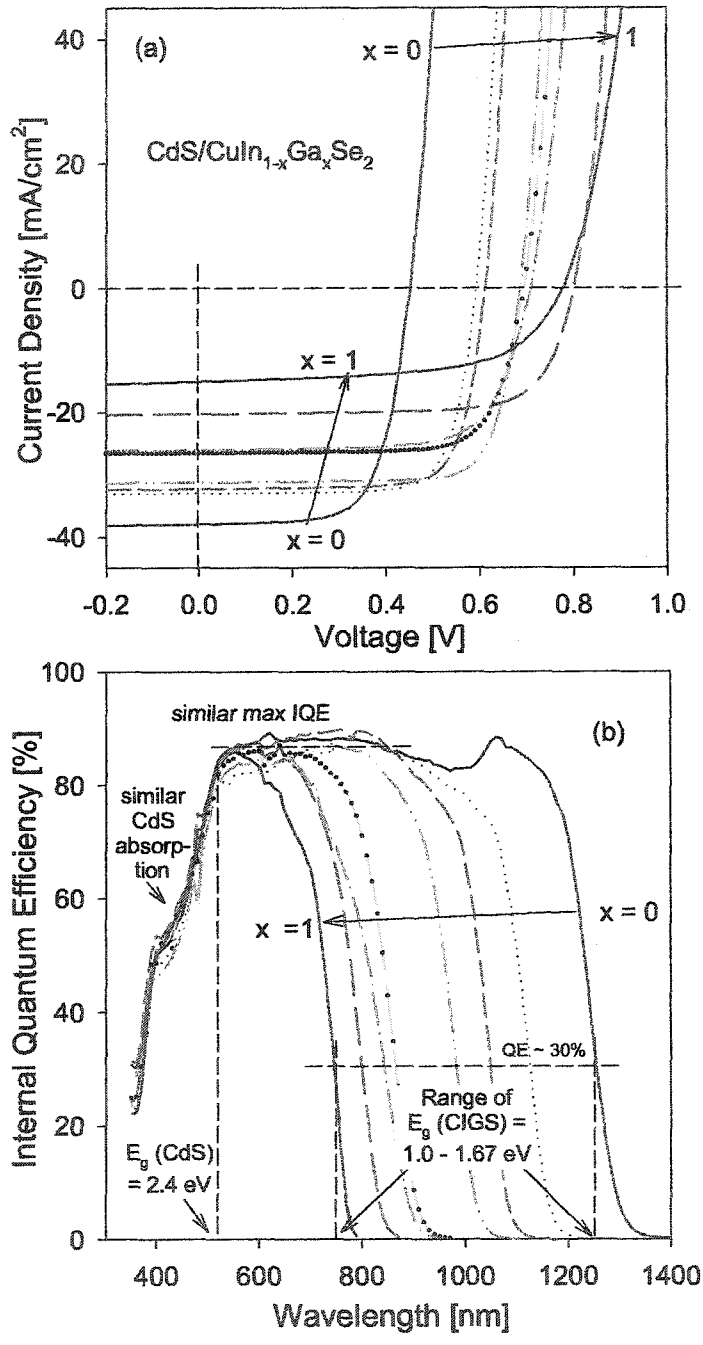

Figure 4.1: CdS/CIGS solar cells with full range $(0-1)$ Ga concentrations in CIGS: (a) Current-voltage curves (100 mA/cm^2 white-light illumination, 25°C); (b) internal quantum efficiency curves (corrected for reflection).

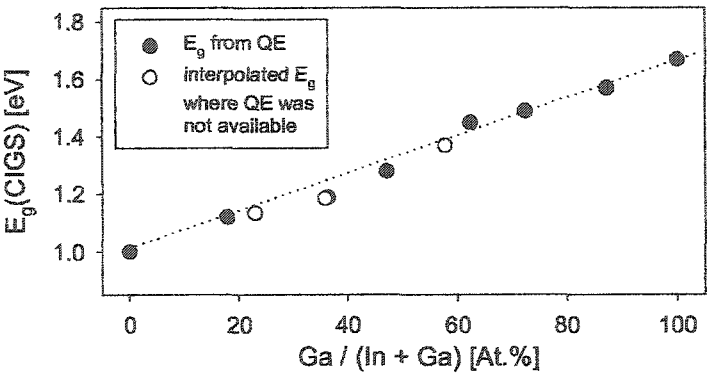

Figure 4.2: Band gap of CdS/CIGS cells as a function of Ga concentration.

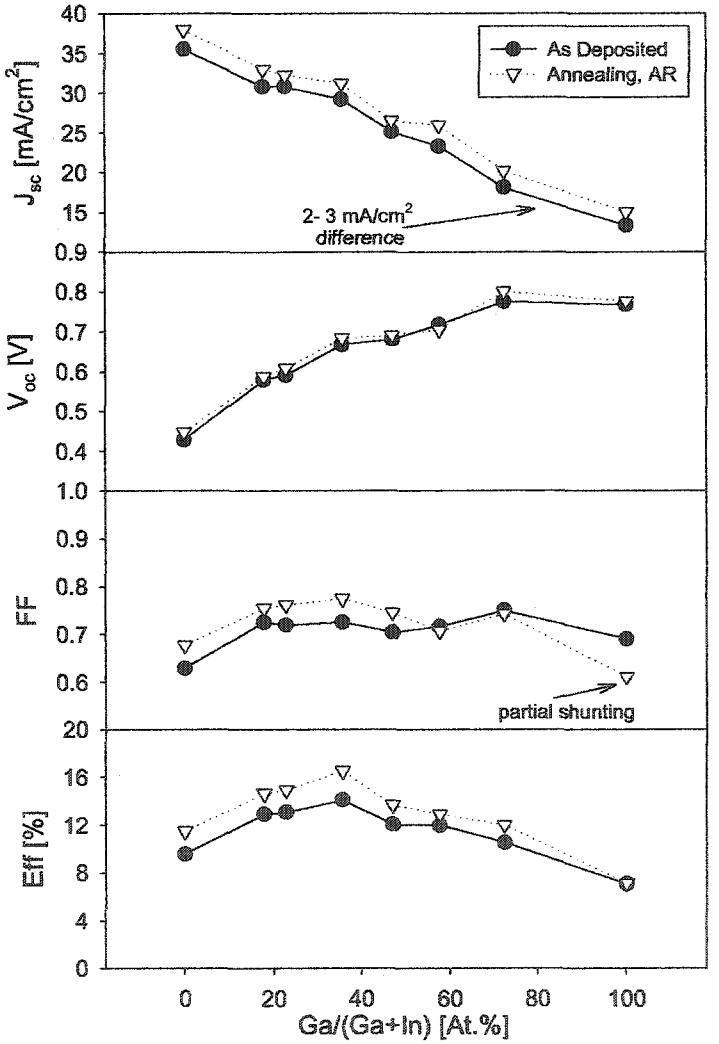

Figure 4.3: Variable-Ga cell performance parameters as a function of Ga concentration before and after the cells were subjected to a 2-min 200°C air-anneal and to the antireflection coating.

normalized to match the measured J_{sc} for the same cell, after which the curves were corrected for reflection ($\sim$ 12% on average) to give internal QE (IQE). Aside from the obvious shift in the band-gap falloff, the shapes of all curves and the maximum IQE values were very similar. This similarity indicates comparable electronic quality of all absorbers. All curves also had very similar amounts of short-wavelength ($\lambda \leqslant 520$ nm) QE reduction caused by CdS absorption. Assuming otherwise identical CdS properties, this indicated very nearly identical CdS-layer thicknesses $\sim$ 50 nm in all cells.

For further analysis, J-V curves at various temperatures (J-V-T) for the variable-Ga cells were measured in the dark and under white light. White-light J-V curves for cells with four representative Ga concentrations in the temperature range between –35 and +45°C at 10°C increments are shown in Fig. 4.4. For all cells, the changes in the J-V curves with decreasing temperature followed standard diode-curve behavior: V_{oc} increased steadily whereas J_{sc} showed little or no change. The figure indicates, however, that there were different voltage-change rates (dV_{oc}/dT) for different Ga concentrations. For all cells with Ga concentration $\gtrsim 0.18$, dV_{oc}/dT was near –2 mV/K, a typical value for CIGS cells, but the rate was much lower (~ -1.1 mV/K) for the CIS cell. The reduced rate is likely from a large conduction-band spike in the junction, which is the topic of *Section 4.2*. An additional feature was observed in the highest-Ga curves: the "knee" part of J-V changed to a more washed-out shape at the lower temperatures, corresponding to a loss in FF.

Standard diode formalism was applied to the analysis of the J-V curves. The photo-diode equation of the following form was assumed:

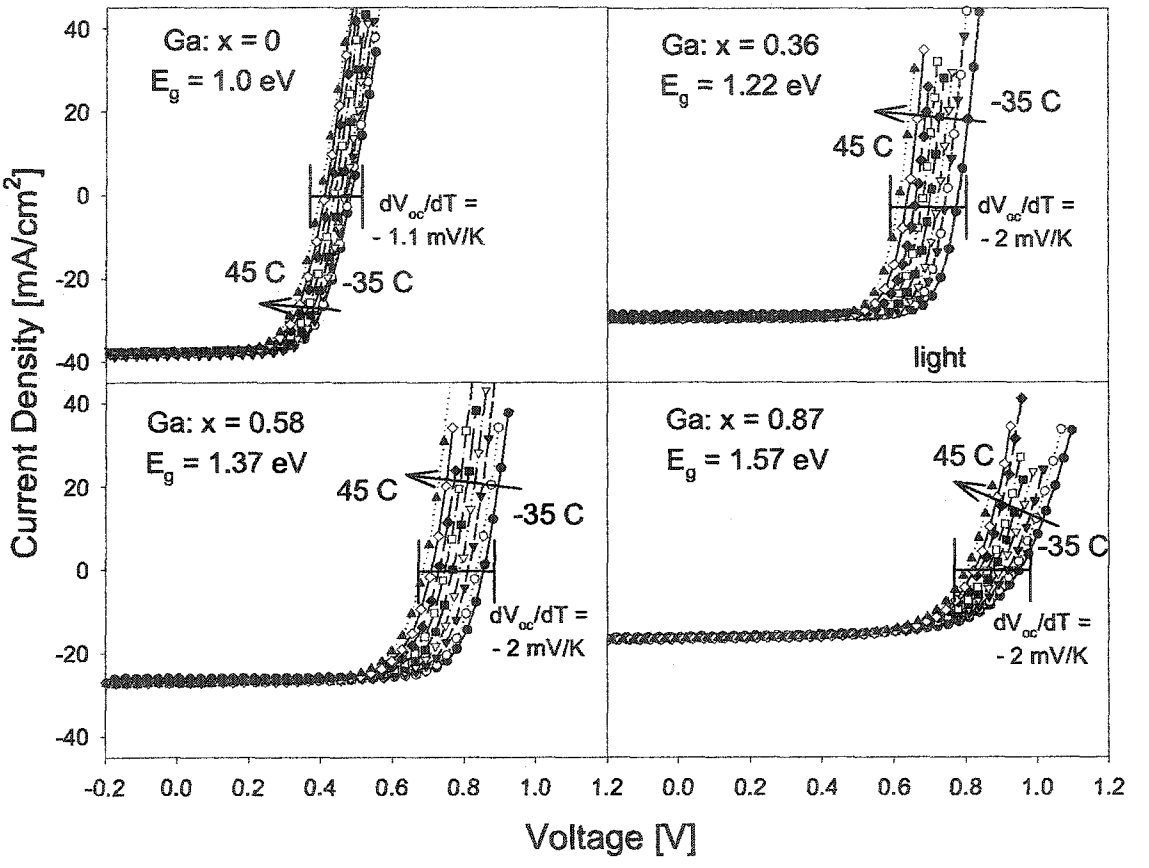

Figure 4.4: White-light J-V-T for $CdS/CuIn_{1-x}Ga_xSe_2$ cells with x = 0.00, 0.36, 0.58, and 0.87.

$$J = J_0(\exp\frac{q(V - R_s J)}{AkT} - 1) + J_L + \frac{V - R_s J}{r_{sh}} \tag{4.1}$$

where V is the applied voltage, J is the resulting current density, J_L is the photocurrent density, J_0 is the reverse diode saturation current density, R_s is the series resistance, r_{sh} is the shunt resistance, A is the diode quality factor, k is Boltzman's constant, and T is the temperature. Series resistances, shunt resistances, and the diode-quality factors of the J-V curves taken at various temperatures for the variable-Ga cells were determined with the technique developed by Sites et al. [40]. In all cases, series resistance increased with decreasing temperature, which is expected for semiconductors. Fig. 4.5 shows the dependence of the diode-quality factor on temperature for variable-Ga cells. The A-values separated into three groups: A $\sim$ 1.5 and independent of temperature for CIGS band gaps E_g = 1.0–1.2 eV, A $\sim$ 2.2 and independent of temperature for E_g = 1.28–1.49 eV, and A $\sim$ 3 and increasing with decreasing temperature for E_g = 1.57 eV (and above). According to the literature, it is likely that the A-values for the 1.57-eV CIGS cells would level out at higher temperatures, at which the measurements were not done. In general terms, the diode-quality factor is a measure of the amount of undesirable recombination occurring in a diode. Thus, according to Fig. 4.5, there was a difference observed in the recombination mechanisms (or at least recombination amounts) between the cells with low and medium Ga concentrations (absorber band gap below and above $\sim 1.2 - 1.3$ eV). A suggested source of the increased recombination for E_g(CIGS) above 1.2 eV — the buffer/absorber interfaces — will be discussed in *Section 4.2.6*. The high temperature-dependent recombination for E_g(CIGS) > 1.57 eV is likely due to poorer absorber quality that is usually observed in CGS and high-Ga CIGS alloys.

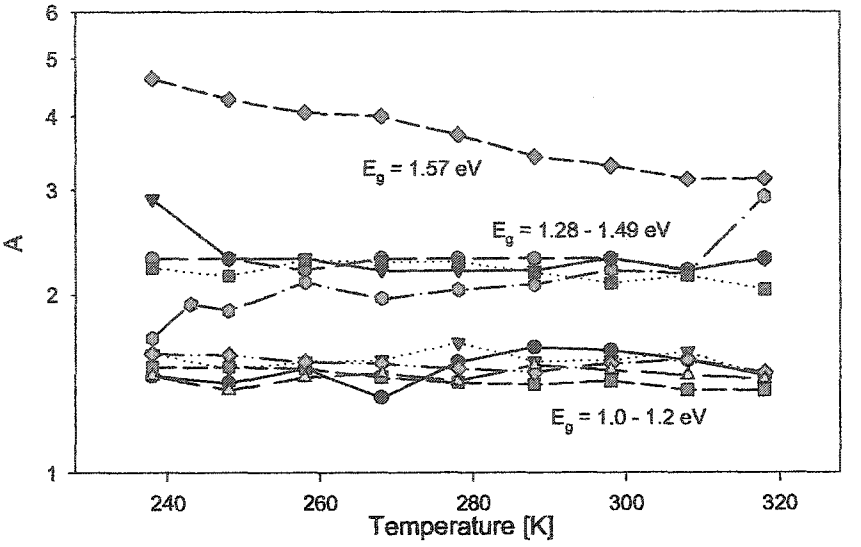

Figure 4.5: Diode-quality factor A for cells with different E_g(CIGS) as a function of temperature.

4.1.2 CdS/CIS cells with variable CdS thickness

Figure 4.6 shows internal quantum efficiency curves for CdS/CIS cells with CdS of variable thickness deposited on both single-stage and three-stage CIS. As was discussed in *Section 2.3.2*, buffer absorption decreases the number of incident photons with $h\nu \geqslant E_g$(buffer) that contributes to overall photocurrent; thicker buffers result in higher photon loss. Thus, the curves with higher response between $\lambda = 380 - 520$ nm correspond to thinner CdS layers. The specific CdS thicknesses were determined by comparison of the integrated short-wavelength currents to those of thin-film CdTe cells with known CdS thicknesses [41]. IQE values were very similar for $\lambda > 520$ nm for all cells of both types of CIS absorbers. The IQE curves did not change significantly after a 2-min 200°C air-anneal of the cells.

Figure 4.7 shows J-V curves for CdS/CIS cells from Fig. 4.6 measured under standard 100 mW/cm^2 white-light illumination at 25°C, both before and after the anneal. Curves for as-deposited (Fig. 4.7[a]) single-stage cells were similar for all CdS thicknesses, though

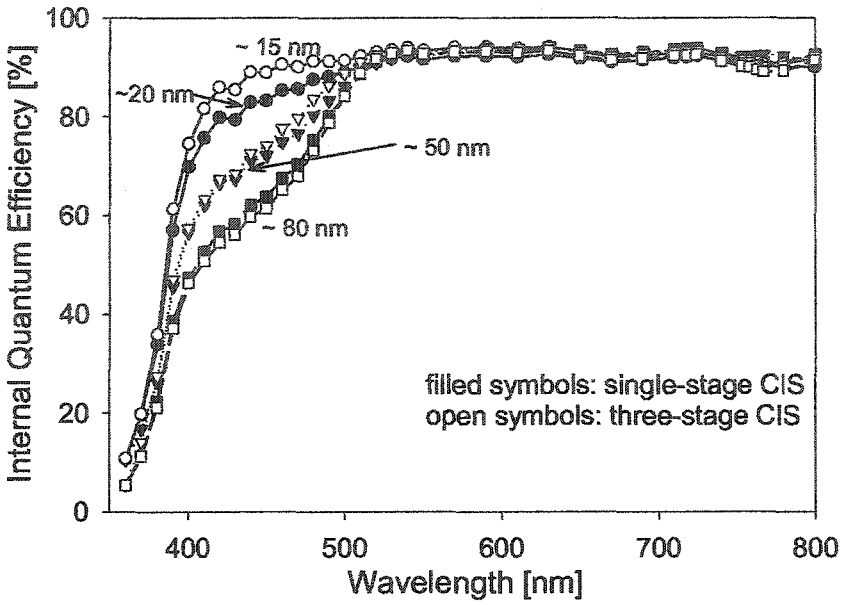

Figure 4.6: Internal quantum efficiency for CdS/CIS cells with variable CdS thicknesses.

the thickest-CdS (80-nm) cell had a slightly smaller FF. In as-deposited three-stage cells, FF decrease with increasing CdS thickness was more pronounced. This progression is consistent with the effects of secondary barriers in the CdS/CIS junction and will be explained in detail in *Section 4.2.3.* The as-deposited single-stage cells all showed slightly higher V_{oc} values compared to the three-stage cells. The differences in J_{sc} between cells with thinner and thicker CdS, expected from short-wavelength QE differences in Fig. 4.6, were not pronounced. The effects of the air-anneal on J-V (Fig. 4.7[b]) were a slight V_{oc} increase for three-stage cells, and a very significant V_{oc} decrease for single-stage cells. Slight improvements of V_{oc} caused by air-anneals have often been observed in CIGS solar cells. One possibility for the strong V_{oc} reduction in single-stage cells is the noticed mechanical non-ideality of the back contacts probably aggravated by the anneal. The slight dependence of FF on the CdS thickness in both single-stage and three-stage cells remained after the anneal. Results from the temperature-dependent J-V (J-V-T)

measurements taken for these cells under the red light, as well as the standard white light, will be discussed in *Section 4.2.5.*

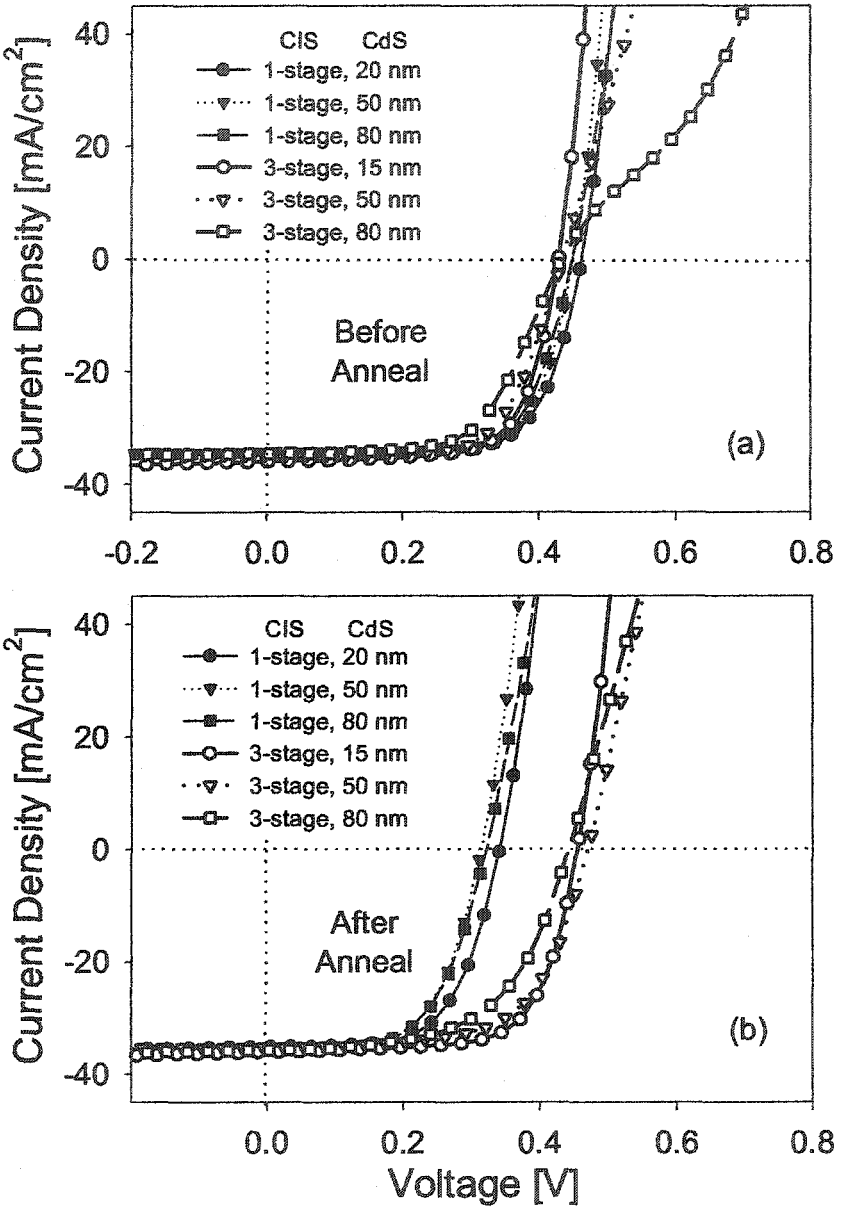

Figure 4.7: White-light J-V for variable-CdS cells from Fig. 4.6, both before and after a 200°C 2-min air-anneal.

4.1.3 CIGS with alternative buffers: ZnS(O,OH)

This section and the next one discuss CIGS solar cells with the buffer materials alternative to CdS. The band gaps of the alternative buffers are higher than that of CdS, and improved short-wavelength quantum efficiency, and thus J_{sc} and hopefully efficiency, are expected.

Figure 4.8(a) shows NREL-certified J-V measurement for a previous record CdS/CIGS cell with 19.2% efficiency [42]. It also shows the curve for one of the ZnS(O,OH)/CIGS cells described in *Section 3.1.3* with 18.6% efficiency [18], which is currently the record for CIGS with any alternative buffer. The curves had a very similar appearance except for a 25-mV voltage difference, and an insignificant current difference. Although the record cells are shown for discussion purposes, other cells made under nominally identical conditions yielded very similar J-V curves.

The J-V data from Fig. 4.8(a) was corrected for the shunt and series resistances and re-plotted on a semi-logarithmic scale (Fig. 4.8[b]). Apart from the 25-mV V_{oc} difference, the logarithmic plot did not reveal additional differences in current transport between the two cells. The shunt and series resistances and the diode-quality factors deduced for both cells indicated on the figure were also similar. It is clear that the superior performance of the CdS cell was almost entirely due to its higher voltage. The ZnS(O,OH)-cell substrate was subsequently annealed in air for 2 minutes at 200°C, after which the performance of these cells deteriorated (see *Section 4.1.4*).

Figure 4.9 shows the NREL-certified QE measurements for the two cells from Fig. 4.8. The curves shown were normalized to the cells' measured J_{sc} values. The infrared QE falloff for both cells indicated CIGS absorber band gaps of 1.15 – 1.16 eV. The slightly-

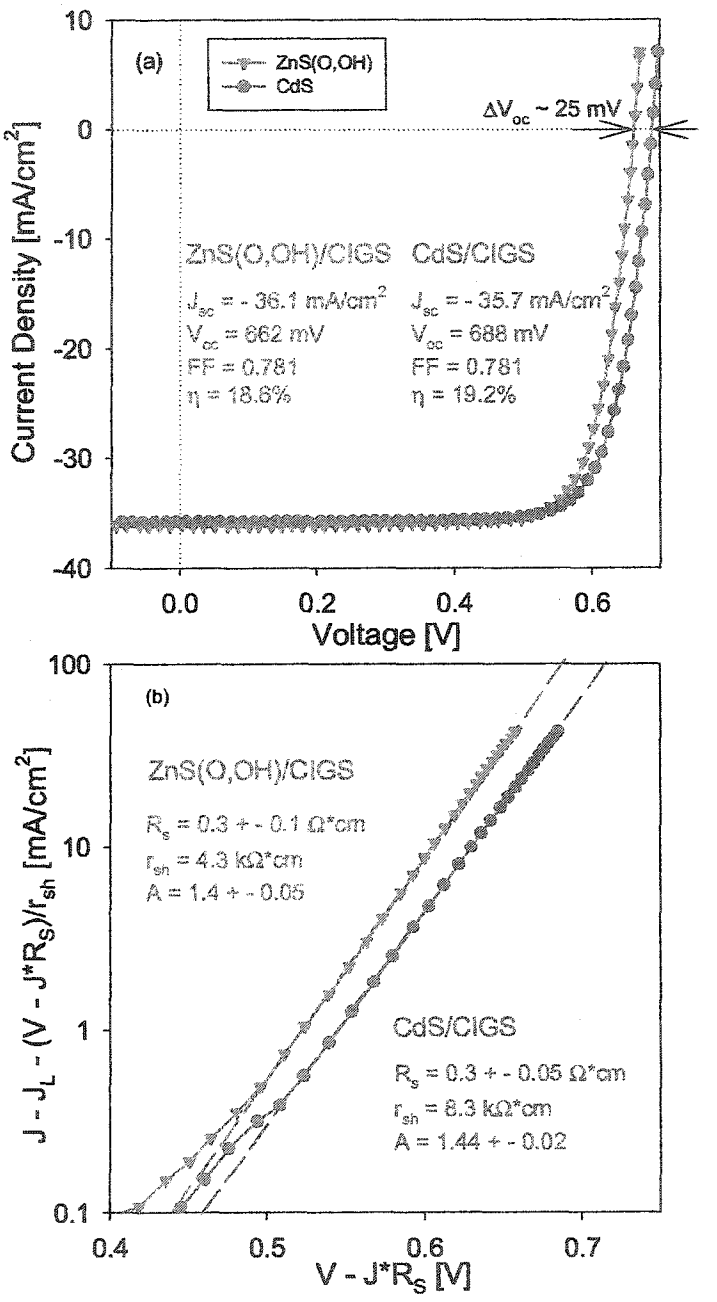

Figure 4.8: (a) Certified NREL J-V measurements for two CIGS cells: previous record CIGS cell with standard CdS buffer (circles) and record CIGS with alternative (ZnS(O,OH)) buffer (triangles); (b) same data, corrected for shunt and series resistances, on a semi-logarithmic scale.

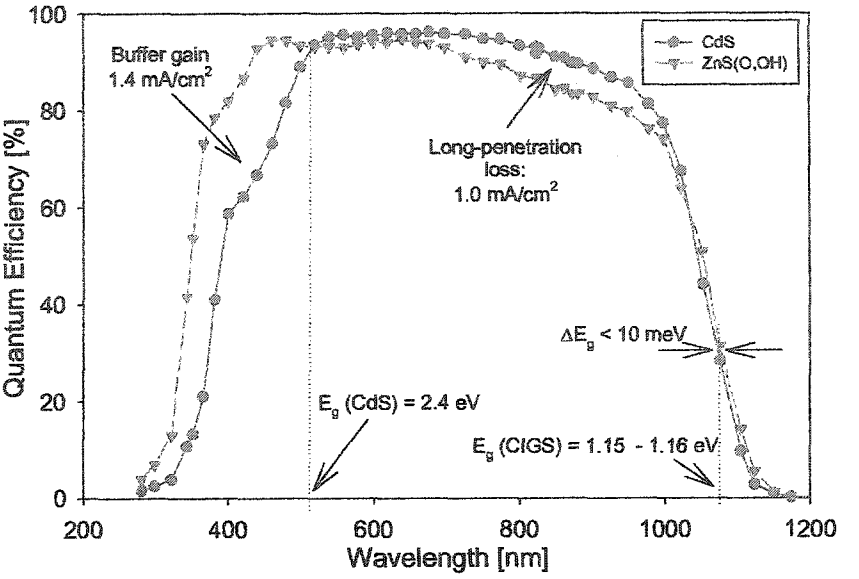

Figure 4.9: Certified NREL quantum efficiency measurements for two record cells from Fig. 4.8.

higher absorber band gap (< 10 meV higher) of the CdS cell only partially accounts for the cell's higher V_{oc}. The remaining ~ 15-mV difference most likely came from the superior quality of the junction formed in the CdS/CIGS cell. The short-wavelength QE response of the ZnS(O,OH) cell was higher than that of the CdS cell, as expected from higher E_g(ZnS(O,OH)). The CdS cell, however, had superior collection in the long-wavelength region. Therefore, the net current advantage of the ZnS(O,OH) cell was only 0.4 mA/cm^2, which agrees with the J-V curves. Note that even without correction for reflection, the QE of these state-of-the-art cells reached high values of 93–95%, compared to somewhat-lower QE values for cells in *Sections 4.1.1 and 4.1.2.*

Figure 4.10 shows dark and white-light J-V curves at temperatures between –45 and 35°C for the two types of high-efficiency cells. One was a cell from the record ZnS(O,OH)-buffer substrate described above. The other was a cell with ~ 1.15-eV CIGS absorber and a standard CdS buffer. Both cells had efficiency slightly above 18%. The temperature dependence of the J-V for both cells appeared very similar: a steady voltage increase of

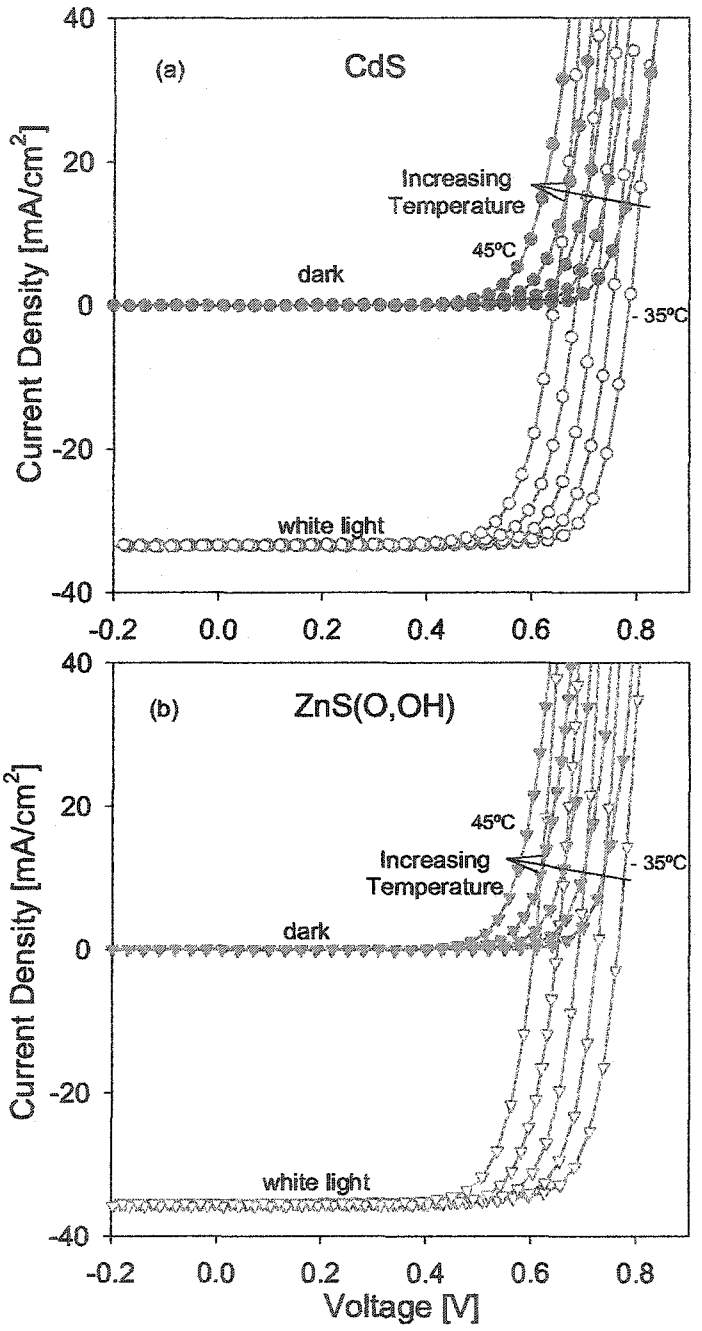

Figure 4.10: J-V-T for high-efficiency (a) CdS/CIGS and (b) ZnS(O,OH)/CIGS cells with E_g(CIGS) $\sim$ 1.15 eV.

approximately 2 mV/K with decreasing temperature (light and dark J-V) with little or no change in J_{sc} and FF.

Figure 4.11 plots J_{sc}, V_{oc}, FF, and efficiency as a function of temperature for the two cells from Fig. 4.10. In the case of these two particular cells, the J_{sc} of the ZnS(O,OH) cell was significantly higher due to its wider-gap buffer. The nearly-equal impact of the ZnS(O,OH)-cell's higher J_{sc} and of the CdS-cell's higher V_{oc} on the efficiency were consistent with very similar efficiencies at all temperatures ($\eta(T_R) \sim 18.1\%$). The J-V-T trends are more clearly seen in this figure: J_{sc} of the cells did not change with temperature, and the V_{oc} and FF increased linearly with decreasing temperature. Thus, the efficiencies of both cells linearly increased with decreased temperature. Even moderately-decreased temperatures resulted in the efficiencies of both cells surpassing the 20% mark. The zero-Kelvin V_{oc}-extrapolations, which in well-behaved cells give rough estimates for the absorber band gap, had similar values of 1.18–1.2 V for both cells, which is slightly higher than the values determined from QE.

4.1.4 CIGS with alternative buffers: InS(O,OH)

Figure 4.12 shows J-V curves for CIGS cells with three buffers (the primary variable parameter): the standard CdS buffer, and alternative buffers InS(O,OH) and InS(O,OH)/CdS, described in *Section 3.1.4*. The CIGS layers all had $E_g \sim 1.13$ eV and were made by similar 'three-stage' methods at two different laboratories, NREL and IPE. Some cells were finished with i-ZnO layers that were twice as thick (2i) as the standard i-ZnO (i), and also without i-ZnO layers (no i). J-V curves from the best cells with CdS are shown in Fig. 4.12(a). The curves for cells with the standard i-ZnO were similar for absorbers

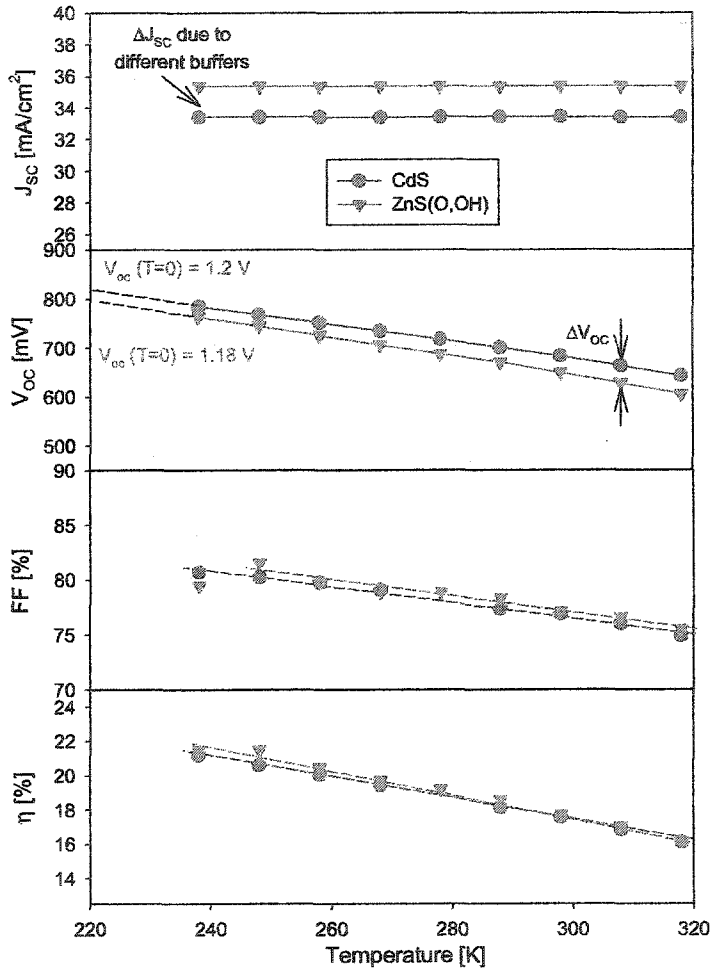

Figure 4.11: J_{sc}, V_{oc}, FF, and η for high-efficiency 1.15-eV CIGS cells with CdS and ZnS(O,OH) buffers.

made at both laboratories. CdS cells with double-i-ZnO, however, showed a reduced V_{oc}. Curves for InS(O,OH)-buffer cells (Fig. 4.12[b]) with no i-ZnO or with standard i-ZnO were also similar for the absorbers from NREL and IPE. The fill factors for these cells were somewhat lower than those of CdS-buffer cells. The curves for cells with the InS(O,OH)/CdS buffer (Fig. 4.12[c]) all showed various amounts of distortion in J-V, and cells with thicker i-ZnO had stronger distortions.

Figure 4.13 shows comparison of light and dark J-V curves from best cells with each type of buffer layer from Fig. 4.12. It also shows the J-V after a 2-min 200°C air-anneal for the ZnS(O,OH) cell, whose record J-V performance prior to the anneal was described in *Section 4.1.3.* All curves on the graph had similar V_{oc}. Wide band gaps of the alternative buffers resulted in slightly higher J_{sc} values for the corresponding cells compared to CdS cells. The alternative-buffer curves, however, had reduced fill-factor values. In addition to reduced fill factors, the alternative-buffer cells all had various amounts of dark/white-light crossover compared to well-behaved dark and white-light J-V for CdS. Both the J-V distortions in Fig. 4.12(c) and the reduced fill factors in Figs. 4.12(b) and 4.13, as well as the reduced fill factors for CdS/CIS cells in Fig. 4.7, can be explained by secondary barriers at the hetero-interfaces (see *Section 4.2*).

Figure 4.14 shows QE curves for an InS(O,OH)-buffer cell and a high-efficiency CdS-buffer cell. The infra-red QE falloffs indicated similar CIGS band gaps for both cells. As with the ZnS(O,OH) cells discussed earlier, the InS(O,OH) cell had a superior short-wavelength response due to wider buffer band gap. The response in the remaining wavelength range, however, was somewhat lower than that of the CdS cells. This is in agreement with only slightly improved J_{sc} of the alternative-buffer cell compared to that of the CdS-buffer cell in Fig. 4.13.

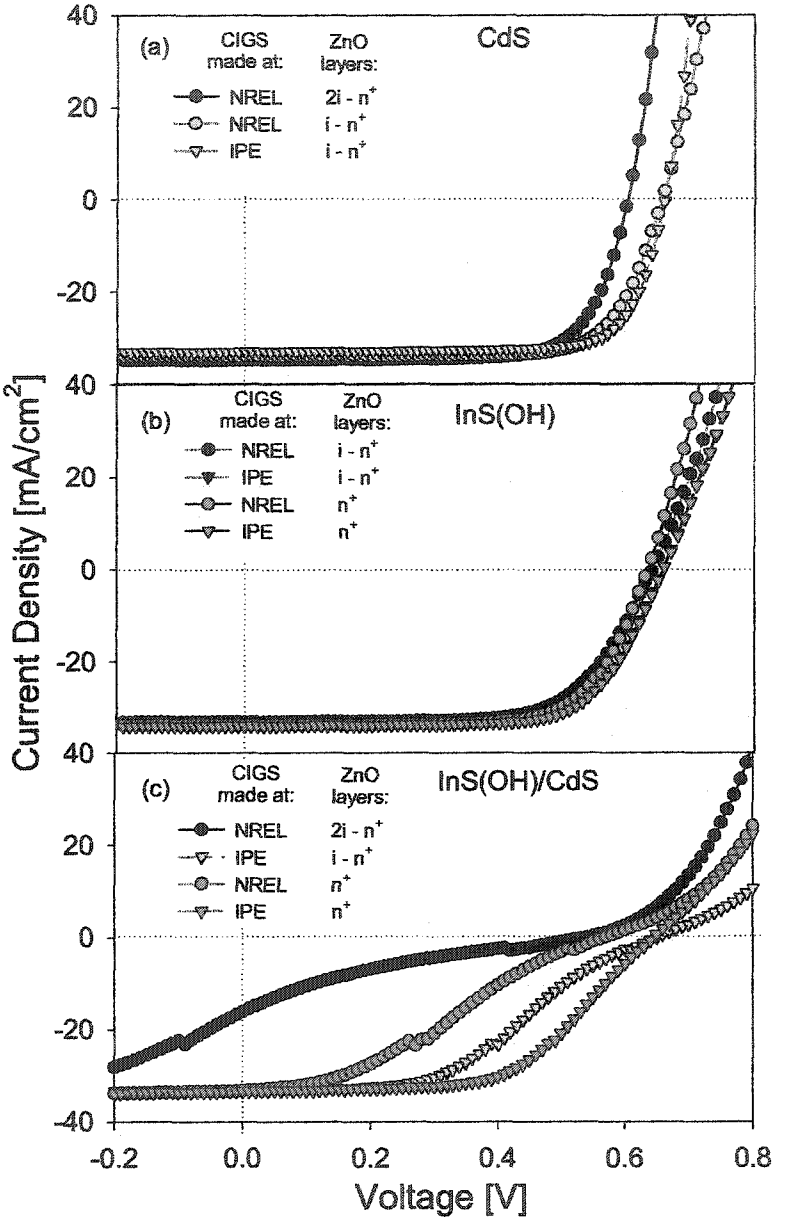

Figure 4.12: J-V for cells with three-stage 1.15-eV CIGS absorbers, made at NREL and IPE, and with (a) CdS, or (b) InS(O,OH), or (c) InS(O,OH)/CdS buffers; i-ZnO thickness is also varied.

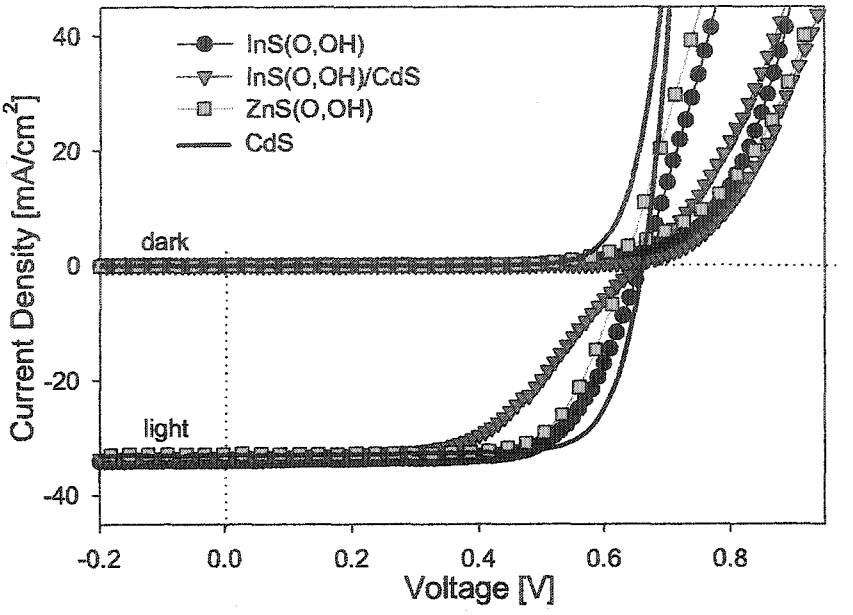

Figure 4.13: J-V for 1.15-eV CIGS cells with CdS, InS(O,OH), InS(O,OH)/CdS, and ZnS(O,OH) buffers.

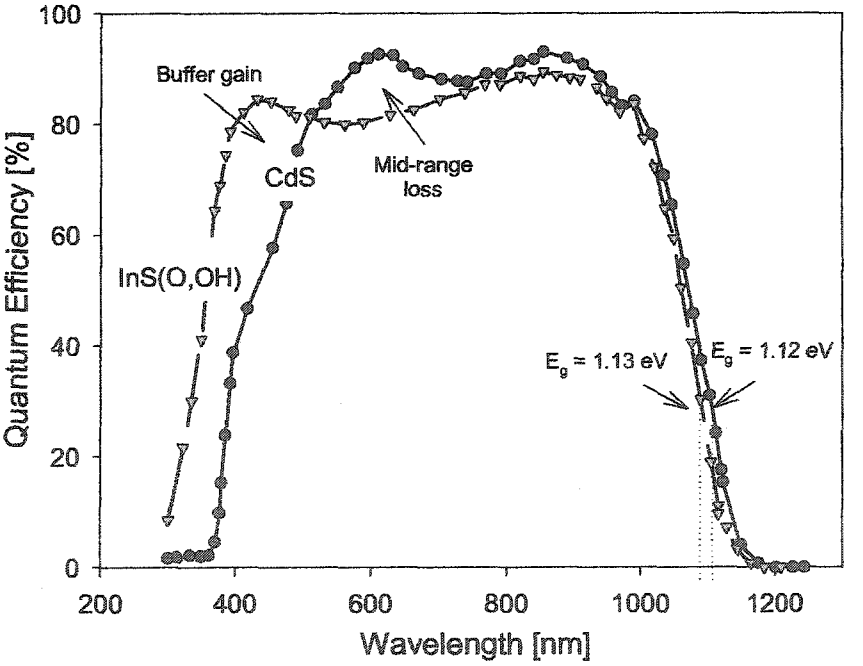

Figure 4.14: QE curves for an InS(O,OH)/CIGS and a CdS/CIGS cell with similar absorbers.

4.1.5 Performance summary

J-V and QE for CdS/$CuIn_{1-x}Ga_xSe_2$ cells with variable Ga concentration, CdS/CIS cells with variable CdS thickness, and for 1.15-eV CIGS cells with ZnS(O,OH) and InS(O,OH) alternative buffers were measured. In variable-Ga cells, CIGS band gaps were determined from QE. The dependence of E_g(CIGS) on Ga concentration was nearly linear within the full range of the alloy ($E_g = 1.0 - 1.67$ eV). QE also indicated nearly-identical CdS-layer thicknesses for all the cells, as was intended. The character of dependence of J_{sc}, V_{oc}, FF, and η from standard white-light J-V curves on E_g(CIGS) were in agreement with previous work on similar cells with Ga- and Al-alloys of CIS. Specifically, J_{sc} decreased linearly with E_g(CIGS) increase, whereas V_{oc} increased but saturated for $E_g \gtrsim 1.2$. The subsequent deposition of the AR-coating and the air anneal of the cells in this work resulted in improved performance for all Ga concentrations.

White-light J-V-T measurements on the CdS/CIGS cells with variable Ga revealed a difference in recombination magnitude, and perhaps the recombination mechanisms, between cells with low and high Ga concentrations. *Section 4.2.2* will discuss additional changes that were observed in the behavior of the cells near the transition Ga concentration ($x \sim 0.35$).

A range of CdS thicknesses was deliberately introduced into CdS/CIS cells, and the specific thicknesses were determined from QE measurements. The thin- and medium-CdS cells showed well-behaved white-light diode curves; the thicker CdS caused fill-factor reductions. There were some distinctions observed between the cells with single-stage and three-stage CIS, in particular, a significant voltage loss was observed for the single-stage solar cells subsequent to a standard annealing step. This, however, was most-likely

caused by a purely mechanical issue of the partial loss of back contact for the given cells, and will not be investigated further in this thesis.

Despite the fact that a fraction of solar photons is lost in CdS buffers, CdS/CIGS ($E_g \sim 1.15$ eV) cells have the highest efficiency for thin-film solar cells to-date [42]. The primary reason for choosing wider-gap ZnS(O,OH) or InS(O,OH) buffers described in this work was to reduce this short-wavelength photon loss. As expected, cells with the alternative buffers showed higher short-wavelength QE response than that of CdS cells. This advantage, however, was offset by somewhat lower long-wavelength QE response and/or V_{oc} and/or fill factors. These losses do not appear unreasonable to overcome. In fact, the best CIGS solar cells with alternative ZnS(O,OH) buffers have already demonstrated the performance [18] approaching that of cells with standard CdS buffers. J-V-T of such high-efficiency ZnS(O,OH)/CIGS cells suggested their photodiode behavior to be basically similar to that of the best CdS/CIGS cells.

The J-V curves for cells with combined InS(O,OH)/CdS buffers were pathologically distorted. The distortion was stronger with greater thickness of the intrinsic ZnO layer in the cells. Such behavior is consistent with the secondary-barrier model that will be discussed next.

4.2 Distortions in diode curves by secondary barriers

This section investigates the effects of the secondary barriers in the junctions of the CIGS solar cells of various configurations on cell performance. The section will be opened with an introduction to the model, which connects distortions of the J-V curves of CIGS cells, also reported occasionally by others, to the discontinuity of the conduction-band minimum at the buffer/absorber interface. Several experiments supported with numerical simulations testing this model will be described. The set of cells for the first experiment — CdS/$CuIn_{1-x}Ga_xSe_2$ cells with variable Ga — provide a wide range of the values for the conduction-band offsets (ΔE_c) according to previous studies. Different E_c-offset values in the structures are expected to produce different amounts of J-V distortion. The second set of solar cells — CdS/CIS cells with varied CdS thickness — will test the model predictions concerning the variation of the secondary-barrier height with the buffer-layer thickness. The effects of the buffer barriers on J-V will then be compared for the CIGS cells with several different buffer materials. Several side points, which provide additional evidence in support of the model, such as the determination of the band gap values for the buffer materials in cells with severe J-V distortions, and the increase of the distortions with decreased temperature will also be described. The discussion of the results, including correlations with the results of the *Section 4.1* and results from the work by others, will conclude this section.

4.2.1 E_c offsets and photoconductivity

For the CdS/CIS diode, and for modest Ga-concentration CdS/CIGS, the conduction-band offset (ΔE_c) between CdS and the CIS (or CIGS) absorber is positive, as determined

from XPS [43], and theory [44]. The dashed line in Fig. 4.15(a) shows the simulated conduction-band minimum E_c at thermal equilibrium (zero bias and no illumination) for an n^+-ZnO/i-ZnO/CdS/CIGS structure. The simulation shown in Fig. 4.15 used a 0.3-eV CdS/CIS ΔE_c, and a 50-nm CdS layer with carrier concentration of n = 6 x 10^{16} cm^{-3}, and the mid-gap acceptor concentration of $N_A = 10^{17}$ cm^{-3}. The particular ΔE_c, n and N_A values are reasonable (though not exactly known) and provided good agreement with experimental J-V curves. The positive offset between buffer and absorber, often referred to as a "spike", forms a secondary barrier that may inhibit electron transport, especially when the cell is in forward bias. In many cases, n-type window layers such as CdS have a significant concentration of acceptor traps and are therefore heavily compensated. Buffer compensation — or low net carrier concentration in general — results in greater distance to the Fermi level at the spike and thus a higher barrier (dashed line). The lack of carriers at the spike limits the maximum current that can flow across the junction [45] according to the thermionic emission theory. Thus, the carrier concentration at the spike is the key quantity, although the spike height relative to the conduction-band minimum in the bulk of the CI(G)S absorber is also a good parameter to use. In general, acceptor traps will have a much smaller electron-capture cross-section when neutral than hole-capture cross-section when negatively ionized. This asymmetry leads to the phenomenon of persistent photoconductivity, in which electron-hole pairs that are photogenerated in the buffer push the acceptor traps towards neutrality, and hence the window layer towards a more positive charge [46, 47]. The effect on the band diagram (solid line in Fig. 4.15[a]) is a downward shift in the conduction band and a reduced barrier to electron transport. Even with the photoconductivity, however, room-temperature current will still be inhibited by large spikes of $\geqslant$ 0.5 eV [48, 49].

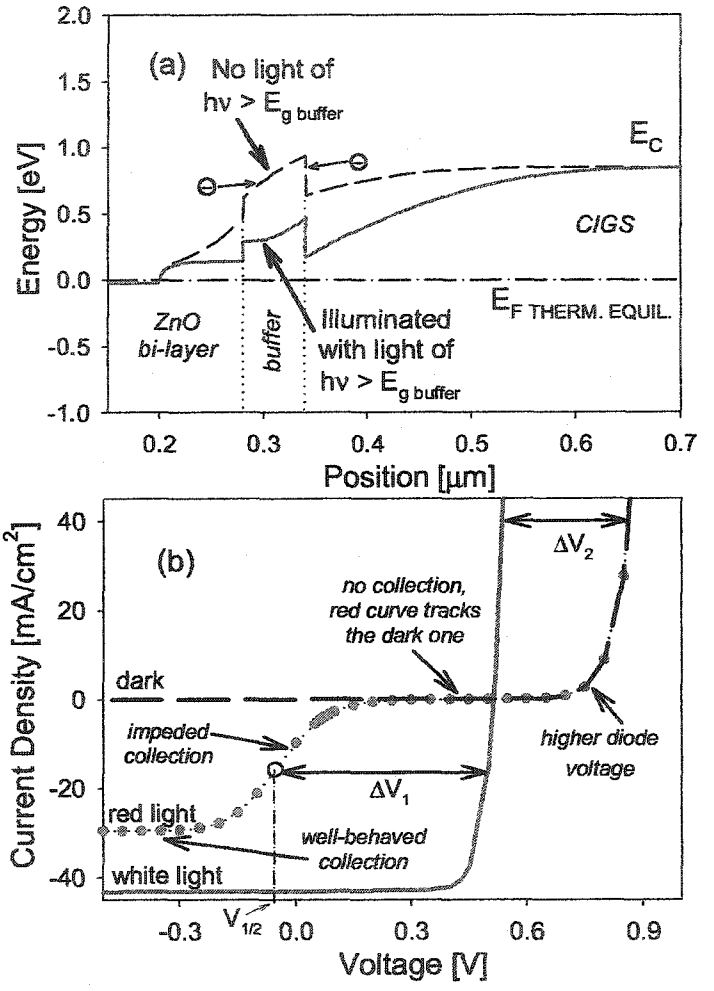

Figure 4.15: Numerical simulations for a buffer(CdS)/CIS structure: (a) E_c with (solid line) and without (dashed line) blue light ($h\nu > E_g$(buffer)); (b) Dark, red-, and white-light J-V curves.

Figure 4.15[b] shows the simulated effect of the low and high barriers on J-V. The curve is well-behaved with the reduced barrier under the standard AM1.5 white light illumination that includes photoconductivity-related blue photons with $h\nu \geqslant E_g$(buffer). The dark curve, however, has a higher diode turn-up voltage. This behavior of white and dark curves that is frequently observed experimentally is often referred to as a "crossover" or "non-superposition". The red-light curve ($h\nu < E_g$(buffer), note reduced J_L) has a reverse-bias region with well-behaved collection, a mid-bias transition region with decreasing collection, and a higher-bias region where the curve merges with the dark J-V curve. The distortion seen in red-light J-V curves has been termed as the "red kink" [46], and both the red kink and dark/light crossover are the effects of a higher secondary barrier without blue-light illumination. The red/white collection voltage difference ΔV_1 and the dark/white non-superposition voltage ΔV_2, shown on the graph, will be used to quantify J-V distortions. The voltage at half the maximum photogenerated current, $V_{1/2}$, will also be used for comparisons.

4.2.2 CdS/CIGS with variable Ga

Figure 4.16(a) shows simulated band diagrams for CdS/CIGS cells with four CIGS band-gap values, which correspond to four different Ga concentrations in actual absorbers. The assumption here is that Ga concentration primarily affects the conduction band. The smallest-gap CdS/CIS is therefore assumed to have the largest positive conduction-band offset ΔE_c (spike). As the band gap increases, the offset becomes smaller and eventually becomes negative (a cliff-type offset) at E_g(CIGS) $\sim$ 1.35±0.1 eV, which would correspond to x $\sim$ 0.5±0.15 in actual absorbers.

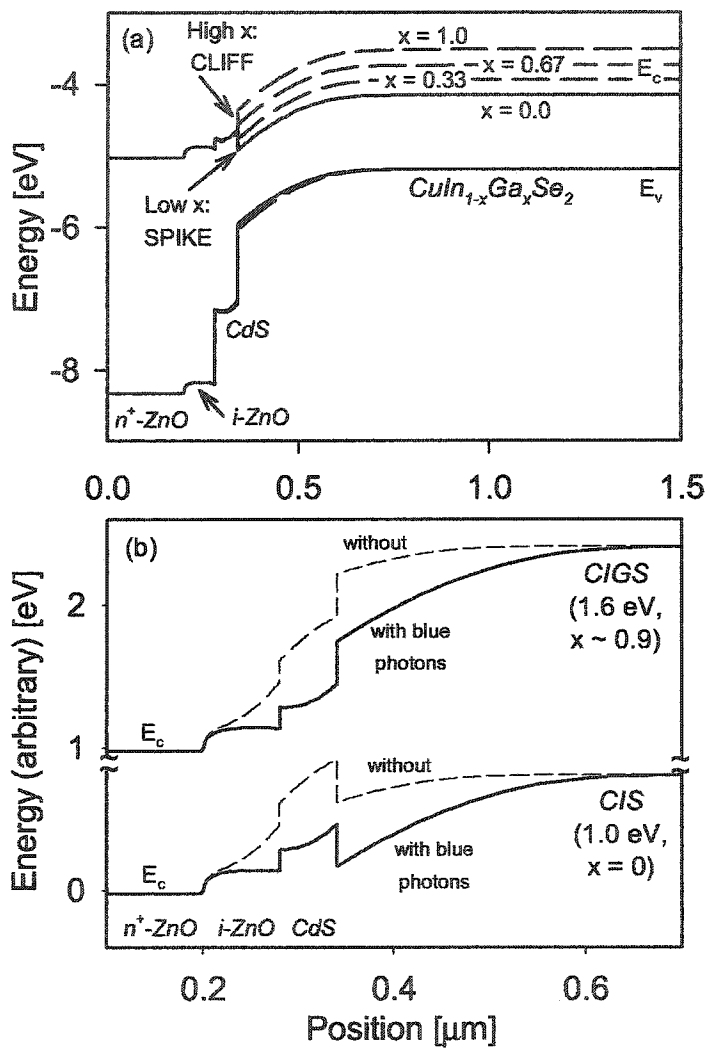

Figure 4.16: Band-diagram simulations for $CdS/CuIn_{1-x}Ga_xSe_2$ (a) four representative Ga concentrations, blue-light illumination; (b) no-Ga and high-Ga structures with and without blue light (only conduction band shown).

Figure 4.16(b) shows the simulated E_c for a 1-eV CIS cell and a 1.6-eV CIGS cell, both with and without short-wavelength (blue) illumination. Much of the blue light is absorbed in the buffer, which may well induce photoconductivity. For the 1.6-eV absorber with a negative (cliff-type) offset at the interface, there are no additional barriers for the photocarriers under either illumination, compared to the situation with the spike in E_c for the 1.0-eV cell discussed in *previous Section*.

J-V curves from the simulations of $CdS/CuIn_{1-x}Ga_xSe_2$ structures with E_g(abs.) = 1.0 – 1.7 eV and with the above assumptions of the variation in ΔE_c were analyzed. In the simulations, besides the J_{sc} decrease and V_{oc} increase resulting from the increasing absorber E_g, white-light curves were well-behaved for all absorber band gaps, but the amount of the distortion in the red-light curves varied. Fig. 4.17 shows kink parameters ΔV_1 and ΔV_2 deduced from the curves. According to the simulated data, the distortion amount in red J-V is largest for CdS/CIS and decreases with increasing CIGS band gap as its E_c-offset to CdS approaches zero. Red kinks are absent for large-band-gap CIGS forming negative (cliff-type) offsets with CdS.

Figure 4.18 shows experimental dark, red-light, and white-light J-V curves for CdS/CIGS cells with eight CIGS band-gap values. As in the simulations and also consistent with previous data in *Section 4.1.1*, the white-light curves showed an increase in voltage and a decrease in current with the CIGS band-gap increase. Additionally, the band-gap increase reduced the conduction-band discontinuity so that the red kink in J-V, as well as the dark/white-light crossover, decreased and then disappeared at $E_g \sim 1.2$ eV. This agrees qualitatively with the simulation predictions of Fig. 4.17. Note that the dark curve for each absorber converged with the red-light curve in forward bias (also in simulations). In addition, reductions of fill factor in experimental J-V taken under red

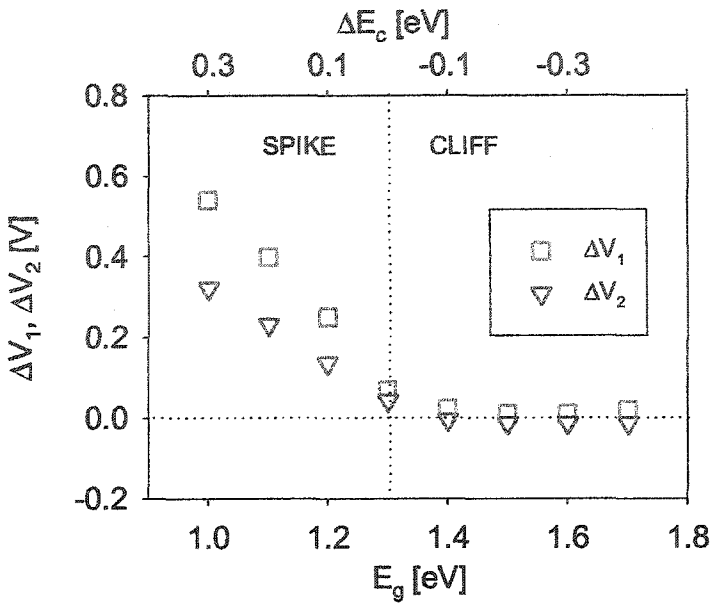

Figure 4.17: J-V kink parameters for simulated CdS/CuIn$_{1-x}$Ga$_x$Se$_2$ as a function of E$_g$(CIGS): ΔE$_c$ changes with E$_g$.

light were observed for CIGS with band gaps between 1.2 and 1.4 eV. These distortions appeared weaker compared to the large-spike effects, and were not accompanied with significant dark/light crossover.

4.2.3 CdS/CIS with variable CdS thickness

Figure 4.19(a) shows the simulated conduction-band minimum E$_c$ for two n$^+$-ZnO/i-ZnO/CdS/CIS structures, where only the thickness of the CdS layer was different (25 nm vs. 75 nm). All other simulation parameters were kept the same as in *Section 4.2.1.* With illumination containing blue photons, the secondary barriers for structures with both CdS thicknesses were low. Without the blue photons, however, the barriers reached energies comparable to that of the bulk absorber due to the compensation of the buffers, and the barrier for the thicker CdS buffer was higher than that for the thinner CdS.

Figure 4.19(b) shows simulated red- and white-light J-V curves for five CdS thick-

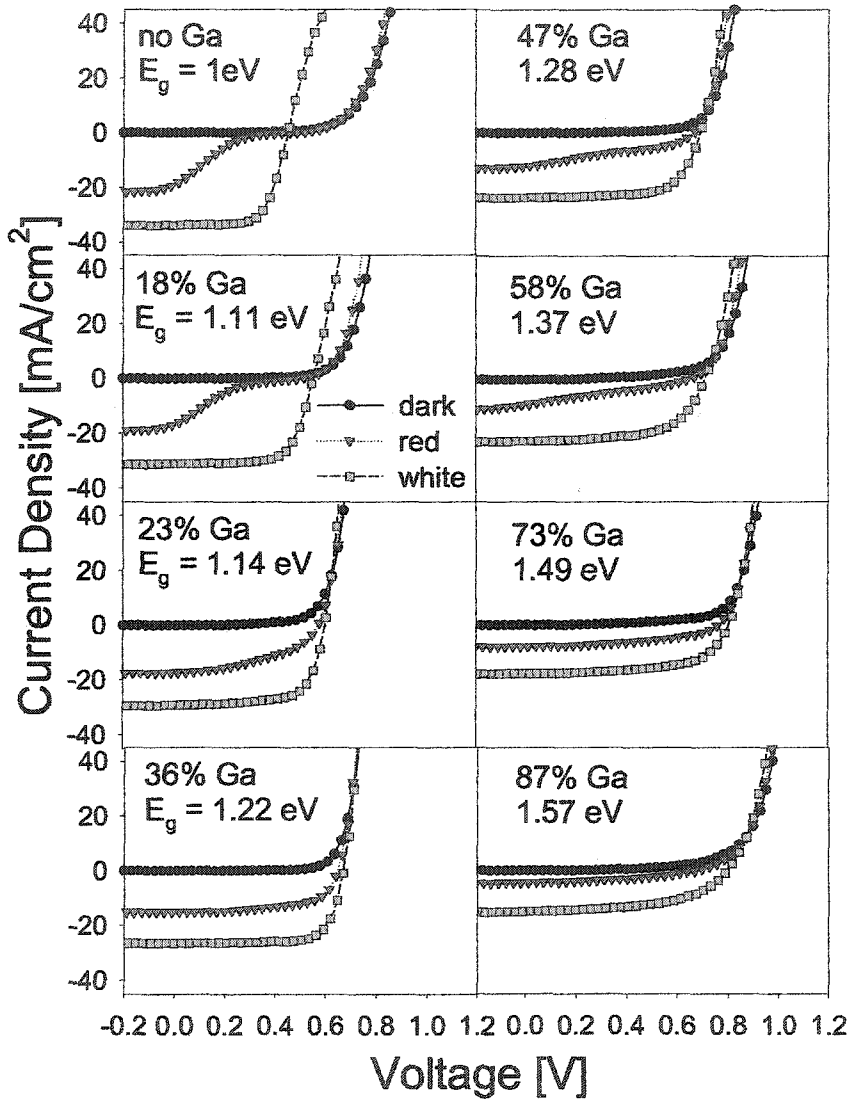

Figure 4.18: Experimental dark, red-light, and white-light J-V for CdS/CIGS with eight Ga concentrations.

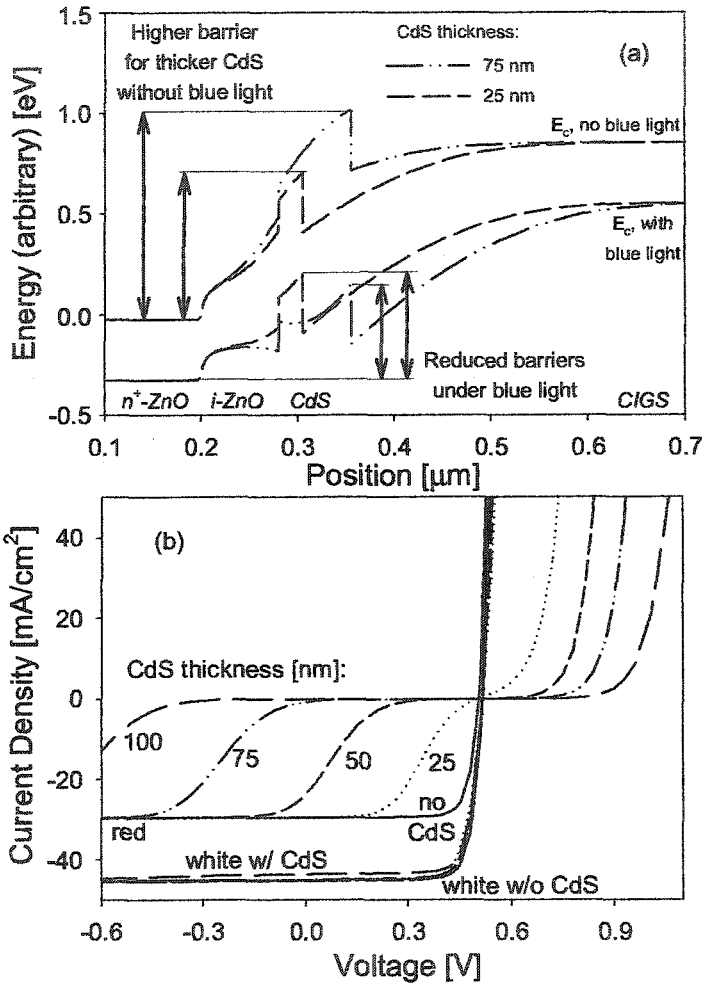

Figure 4.19: Simulated (a) E_c with and without blue-photon illumination for CdS/CIS cells with two CdS thickness; (b) red- and white-light J-V curves for five CdS thicknesses.

nesses between 0 and 100 nm. White-light curves for the five thicknesses were almost identical, in contrast with increasing kinks in the red curves (increasing ΔV_1 and ΔV_2) with thicker CdS. Dark curves (not shown) all converged with the corresponding red curves in forward bias as in Fig. 4.15. Variation in the electronic parameters of the ZnO layers also influenced the barrier height, but did not qualitatively change the progression shown in Fig. 4.19(b). The simulations did indicate that thinning of the intrinsic ZnO layer, as with CdS thinning, led to the reduced barriers and reduced J-V distortions. Note that the simulated CIS structure without a CdS layer resulted in a very good performance under red and white light, whereas actual bufferless cells usually perform poorly, as discussed in *Chapter 2.*

Figure 4.20 shows experimental J-V from cells with different CdS thicknesses and with CIS absorbers made by the single-stage and three-stage processes, both as-deposited and after the 200°C anneal. For each absorber type, three red-light curves corresponding to different CdS thicknesses are shown. A single typical white curve from Fig. 4.7 is shown on each plot for reference. The red-curve progressions, similar to the simulated progression in Fig. 4.19(b), all showed increasing distortions with increasing CdS thickness. Before annealing, the single-stage cells with 20-nm and 50-nm CdS were well-behaved and the thickest-CdS (80-nm) cell showed considerable distortion. The three-stage-absorber cells were similar: the 15-nm-CdS cell showed no distortion and the 50-nm- and 80-nm-CdS cells showed increasing amounts of distortion. As in the simulations, the dark curves converged with the red-light curves in forward bias. After annealing of the cells with the absorbers of both types, the thinnest-CdS cells acquired small red distortions, and the distortions in the thicker-CdS cells became larger. The general progression of the curves, however, did not change.

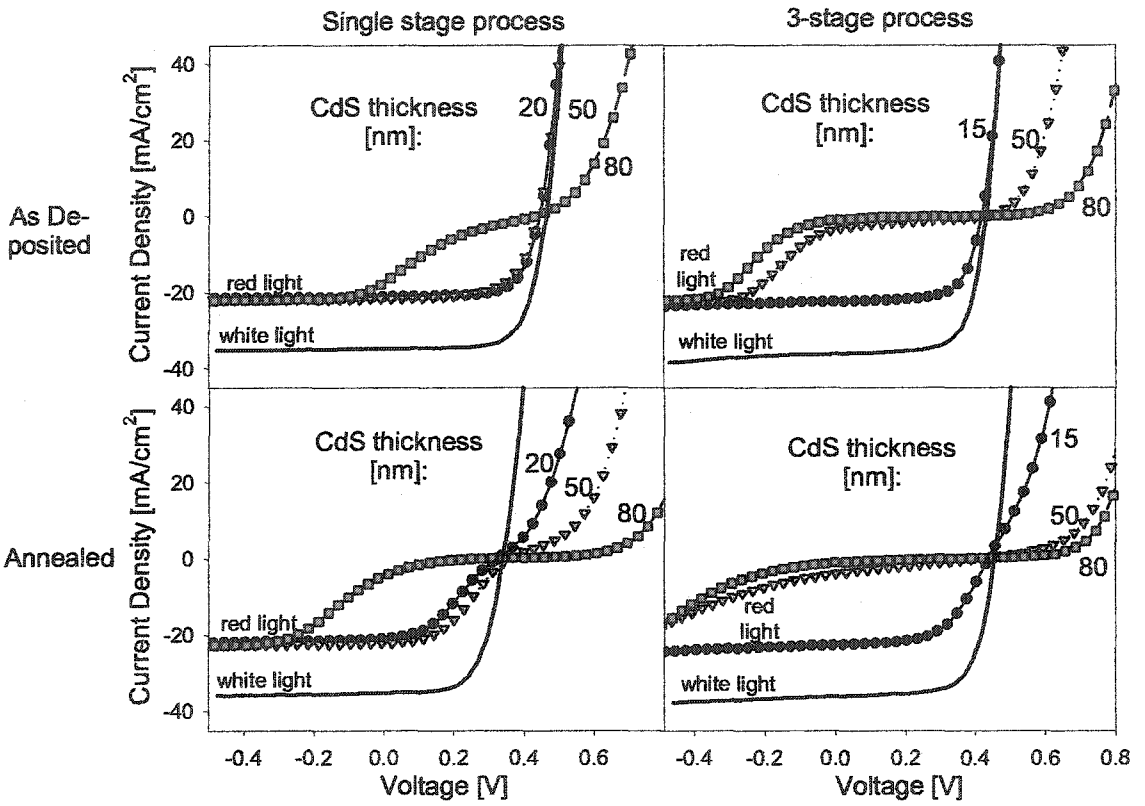

Figure 4.20: Experimental red- and white-light J-V curves from CdS/CIS cells with single-stage and three-stage absorbers and with variable CdS thicknesses, both before and after 2-minute 200°C air-anneal.

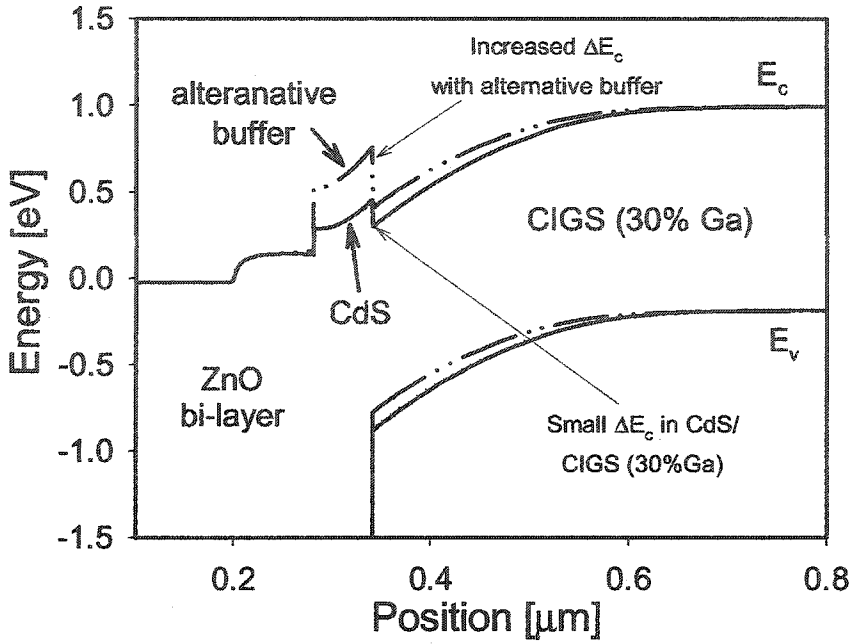

Figure 4.21: Simulated band diagrams for 1.15-eV CIGS cells with a standard CdS buffer and an alternative.

4.2.4 CIGS offsets with alternative buffers

From *Section 4.2.2*, the ΔE_c spike between CdS and the optimal 1.15-eV CIGS should be relatively small, as seen in Fig. 4.21. The graph also shows that use of a wider-gap alternative buffer with the same absorber will likely result in a higher ΔE_c barrier, which, if sufficiently large, should produce a J-V distortion with red light and possibly with white light. The assumption here was that the increased buffer band gap is at least partly due to the upward conduction-band shift.

This argument was partially supported with Fig. 4.13, where white-light J-V curves of the alternative-buffer cells exhibited distortion-related reduced fill factors. Figure 4.22 shows measured dark, red-light, and white-light J-V curves for 1.15-eV CIGS cells with CdS, ZnS(O,OH), InS(O,OH), and InS(O,OH)/CdS buffers from Fig. 4.13. The red curve from the CdS cell was as well-behaved as the dark and the white-light curves. For all three alternative-buffer cells, the small white-light J-V distortions were significantly

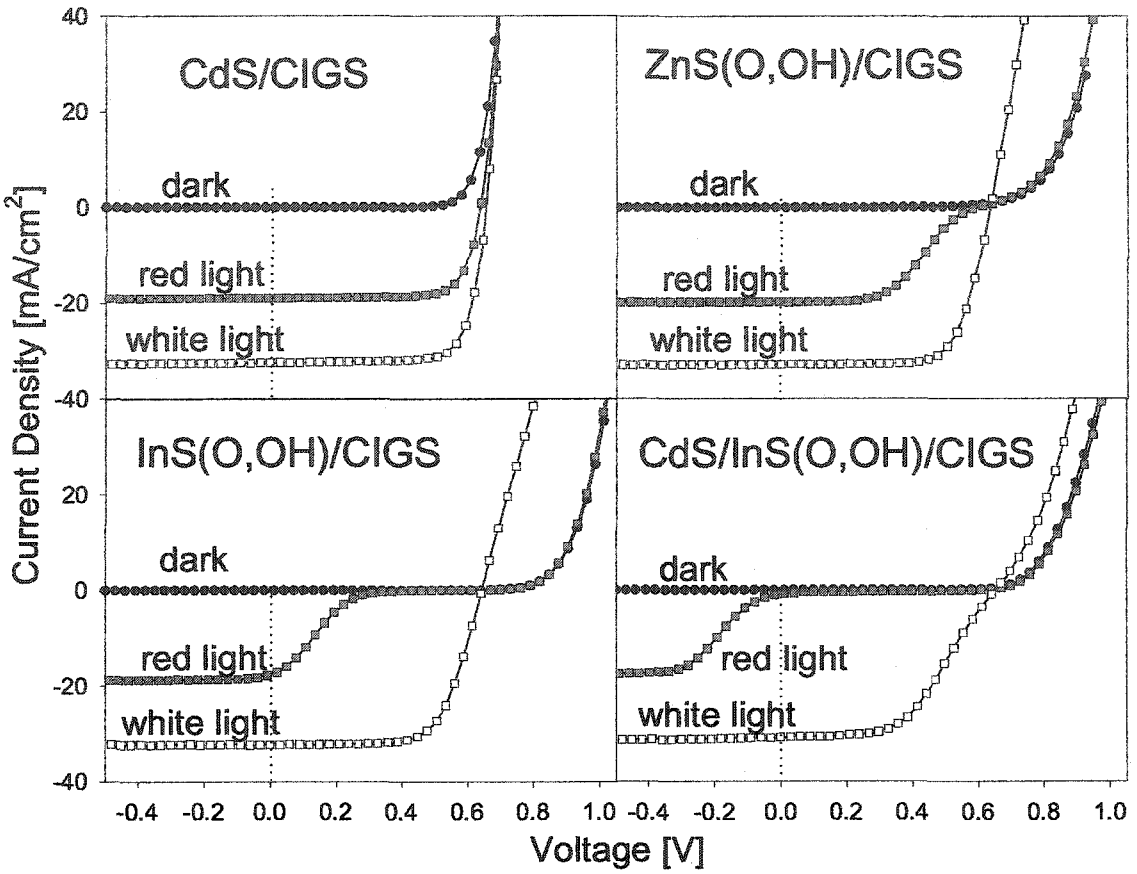

Figure 4.22: Various amounts of distortion in dark, red-light, and white-light J-V curves for 1.15-eV CIGS cells with four different buffers.

increased under red light, which confirmed the presence of significant secondary barriers. For these cells as well, the dark curves converged with the red-light curves in forward bias.

The three alternative-buffer cells had different amounts of the red kink. Note that though a barrier primarily reduces a cell's photocurrent J_L (starting at a certain applied bias), other performance parameters are reduced with different amounts of the kink. FF is primarily affected when a red kink is moderate; for severe kinks, V_{oc} is also affected, and eventually J_{sc} is reduced to zero.

Fig. 4.23 shows the quantum efficiency curves for the cells from Fig. 4.22 measured at zero volts in the absence of additional bias light. For the three cells with the red

kink contained within the power quadrant, or without red kink, the QE curves were well-behaved. QE for the CdS/InS(O,OH) cell, for which the red kink extended into reverse bias in Fig. 4.22 (red-light $J_{sc} \sim 0$), was strongly depressed in the region of photon energies $h\nu \lesssim 2.8$ eV. To better understand the phenomenon, CdS/CIS QE curves, with and without bias light containing blue photons, were simulated for the case, in which the red kink extended well into reverse voltage. The simulation results are shown in Fig. 4.24[a]. Whereas the QE curve with bias light has a standard appearance in agreement with well behaved white-light J-V, a depression in the no-bias-light QE curve is seen below E_g(CdS). Such QE behavior is consistent with large barriers when photons of the QE probing beam having energies below E_g(buffer) are incident on the structure and reduced barriers when the higher-energy photons are incident. Fig. 4.24(b) shows the variation of the buffer band gap with all other parameters (including ΔE_c) identical to those of Fig. 4.24(a). The photon energy values that delineated the "blue" and "red" regions in each QE curve corresponded to the values of E_g(buffer) in all cases. Thus, the buffer band gap can be experimentally determined for large-kink cells from the edge of the QE depression region. The value for the effective optical band gap of InS(O,OH) buffer determined this way from Fig. 4.23 was near 2.8 eV. In agreement with the simulations, exposure of cells with strong red kinks to bias white light of sufficient intensity during the experimental QE measurements was necessary in order to obtain well-behaved curves without reduced collection.

Earlier work [46] established that to remove red kinks from CdS/CIS J-V, incident-photon energies above the CdS band gap (2.4 eV) were needed. The comparable experiment to determine the gap of the InS(O,OH) used a set of optical filters (see Fig. 3.3[b]) to vary the short-wavelength cut-off of the illumination spectrum. Thus, Fig. 4.25

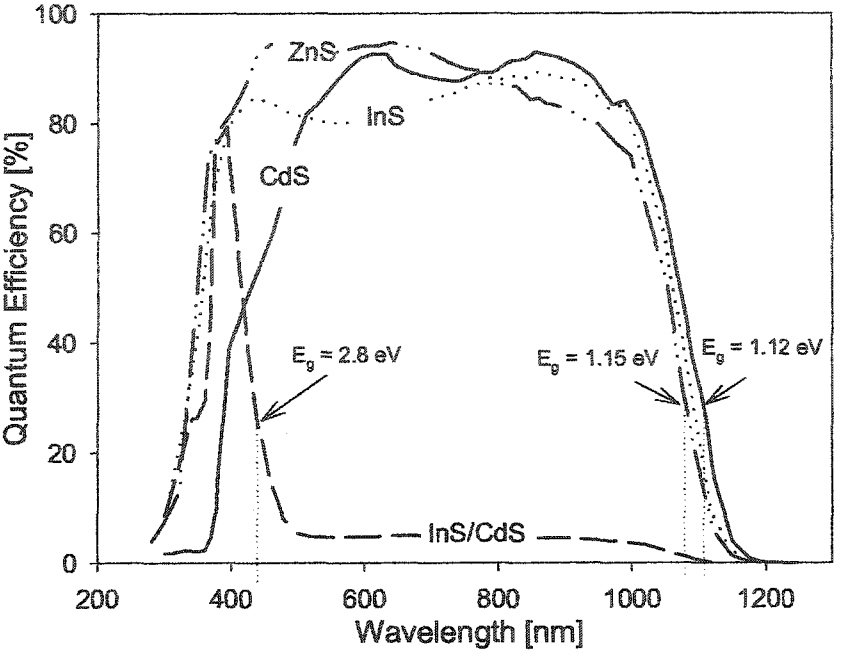

Figure 4.23: QE curves without bias light for the four cells with different buffers.

shows a set of J-V curves taken under illumination through filters with a series of cut-off wavelengths. Note that the J_{sc} increased as the filter cut-off wavelength decreased and more total photons were available. The initially-distorted J-V curve shifted towards the well-behaved shape as the incident photon energies approached and then exceeded 2.8 eV. Therefore, the band-gap value for the InS(O,OH) buffer ($\sim$ 2.8 eV) was deduced from this method, which was consistent with the value determined from the QE-depression edge for a large-kink CdS/InS(O,OH) cell. The large band gap of ZnS(O,OH) buffer material (E_g = 3.7 eV), which is above E_g(ZnO-TCO) = 3.2 eV, did not allow for a similar measurement in cells with this buffer type.

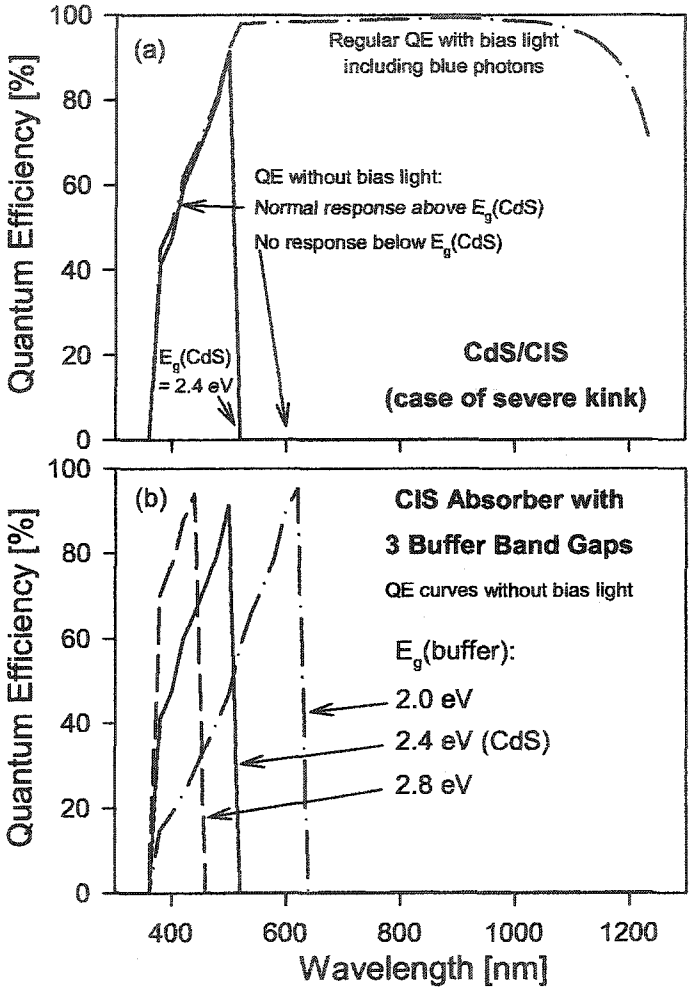

Figure 4.24: Simulated QE curves for cases when red kink in J-V extends well into reverse voltage: (a) CdS/CIS with and without blue bias light; (b) CIS with buffers of varied band gap (ΔE_c and other parameters the same) without bias light.

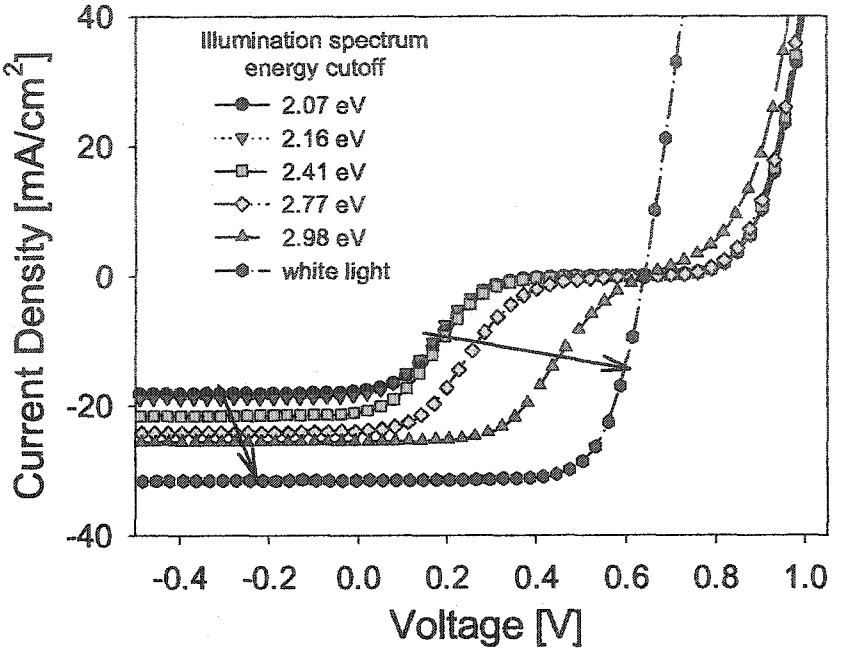

Figure 4.25: An InS(O,OH)/CIGS cell: a series of J-V curves from illumination with spectra that had various upper limits of photon energies.

4.2.5 J-V distortion as a function of temperature

The traditional strategy for measuring the J-V temperature dependence (J-V-T) is to measure both illuminated (with full spectrum of photons) and dark J-V at each temperature in one temperature cycle. The light-exposure results (see *Section 4.3*), however, show that such a measurement will likely mix temperature effects and photo-induced changes. Fig. 4.26 shows J-V-T data for a CdS/CIGS cell (same as in Fig. 4.22) from two temperature cycles. In the first cycle, the dark and red-light J-V were measured with no blue-light exposure (4.26[a]) at any time. In the second temperature cycle, the full-spectrum exposure was continuous for all white-light J-V measurements, and was only turned off for the brief times of the dark J-V measurements (4.26[b]). The J-V-T features in Fig. 4.26(b) (with blue photons) were well-behaved: the rate of V_{oc} change with temperature dV/dT was typical for this kind of cell, no J-V distortion was observed, and

there was no dark/light non-superposition at any temperature. Without blue photons (Fig. 4.26[a]), well-behaved curves were only observed at higher temperatures, which was consistent with well-behaved room-temperature dark and red curves for this cell in Fig. 4.22. The red kink distortion with the CdS buffer, however, appeared in a modest form at low temperature. It was accompanied with an artificially increased voltage-change rate dV_{oc}/dT. The highest- and lowest-temperature curves from Fig. 4.26 (a) and (b) are re-plotted on Fig. 4.26(c) for comparison. At higher temperatures, the J-V curves measured before (dotted) and after (short dash) blue-light exposure were very similar; but at lower temperatures, the red and dark curves measured prior to blue-photon exposure showed distortion and crossover compared to the curves measured after or during the exposure (solid lines vs. long-dashed lines).

Figure 4.27 shows the J-V-T measurements under dark, red-light, and white-light conditions for a three-stage CdS/CIS cell with a 15-nm CdS buffer layer. At room temperature, consistent with Fig. 4.20, this cell had a moderate red kink and a well-behaved white-light performance. The increasing kinks were observed in the red curves with decreasing temperature. The white-light curves were, however, all well-behaved at the temperature range shown. Thus, the amount of the white-red voltage difference in the power quadrant ΔV_1 increased with decreasing temperature. The dark/white-light crossover did not change noticeably with temperature.

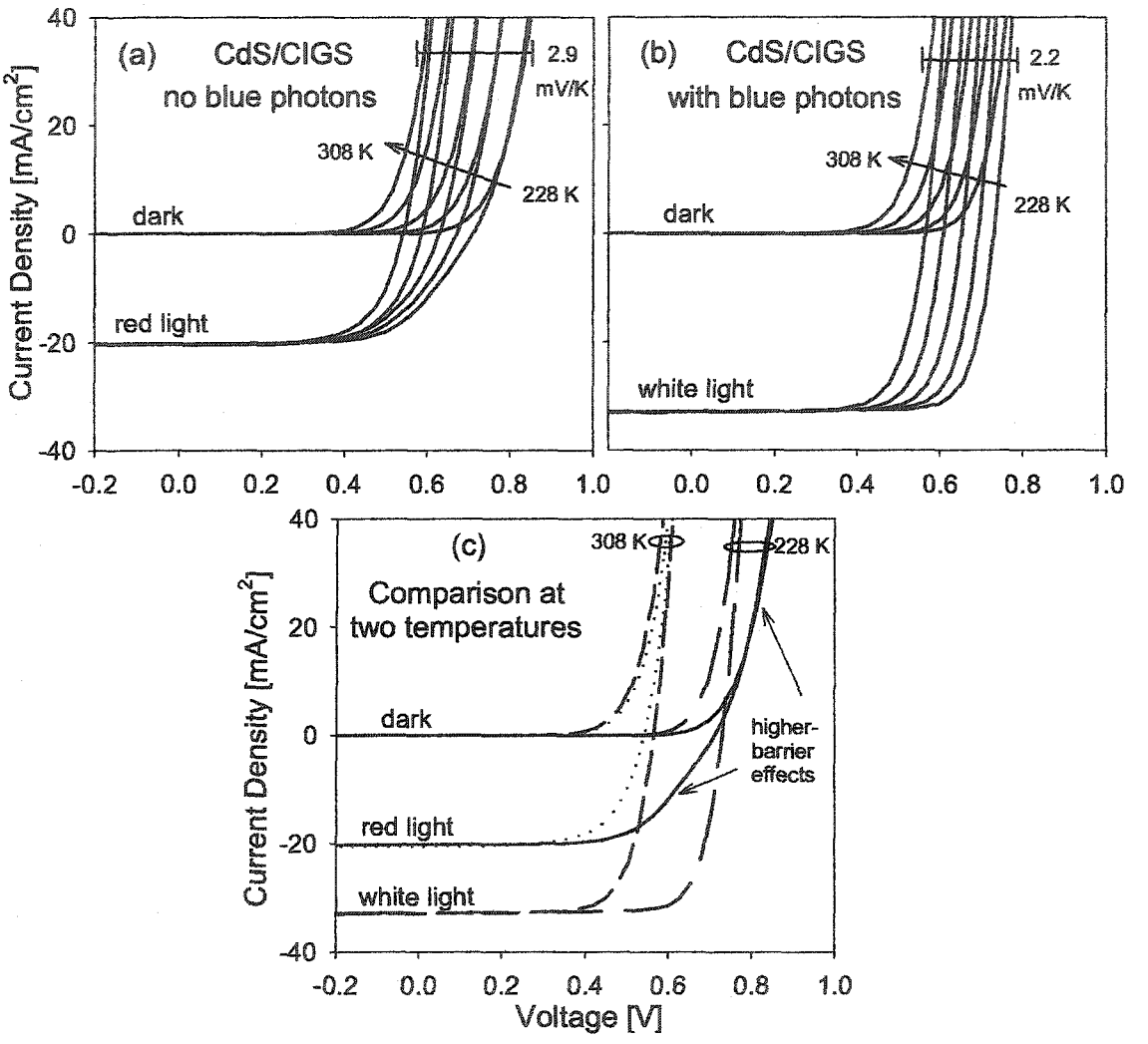

Figure 4.26: J-V-T for a high-efficiency 1.15-eV CIGS with CdS buffer: (a) prior to blue-photon exposure; (b) white-light-soaked; (c) comparison of high- and low-temperature J-V from the graph (a) (solid and dotted lines) and the graph (b) (dashed lines).

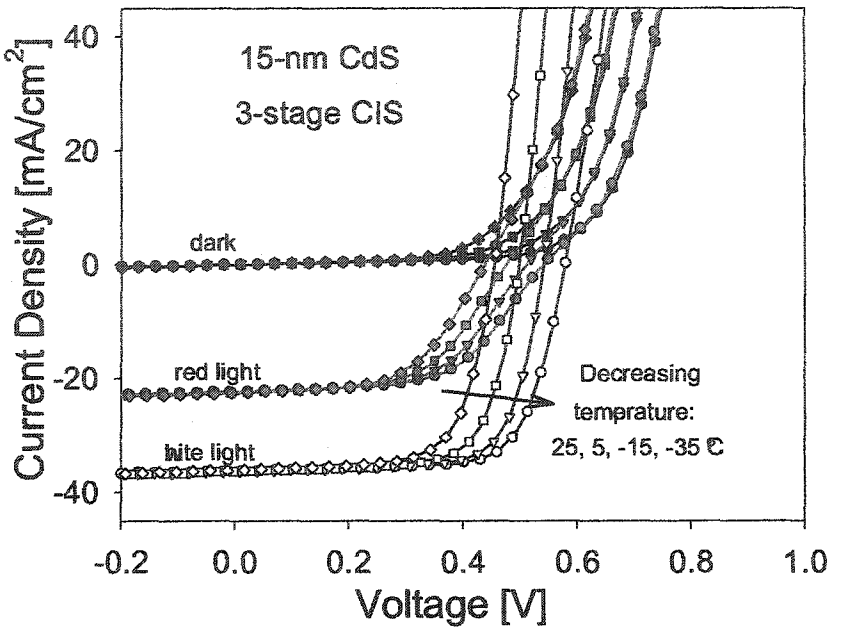

Figure 4.27: Dark, red-light, and white-light J-V-T for three-stage CIS cell with a 15-nm CdS layer.

4.2.6 Secondary-barrier discussion

To summarize, thin-film CIGS solar cells with different structure revealed various amounts of J-V distortion. The observed trends in the results were explained with a relatively straightforward model that includes buffer/absorber ΔE_c and buffer photoconductivity. All data trends observed in the results were confirmed with the corresponding numerical simulations. Fairly substantial lateral non-uniformity of the red-light J-V distortion amount, sometimes extending across the whole cell, is observed in cells that possess kinks (see also [46]). In practice, the device non-uniformity could result in the less-than-exact correspondence between the one-dimensional numerical predictions and cell results.

For the various absorber compositions in CdS/$CuIn_{1-x}Ga_xSe_2$ cells, the largest conduction-band positive ΔE_c (spike) will be formed in CdS/CIS producing a serious red-light J-V distortion. The offset is moderately positive in CdS/CIS, decreases with Ga and is moderately negative in CdS/CGS. Due to the change in CdS/CIGS ΔE_c, the red kink decreases

with the increasing CIGS Ga concentration. According to the numerical simulations, the red kink should disappear when ΔE_c is near zero. In experiments, the disappearance of the red kink occurred for $CdS/CuIn_{1-x}Ga_xSe_2$ at x $\sim$ 0.35 ($E_g \sim 1.22$ eV). Similar CIGS band gap value, at which the ΔE_c transition occurs, is expected from theory and direct measurements by others [43, 44].

In *Section 4.1.1*, the increased diode-quality factor values (greater recombination) and limited V_{oc}-values were observed for the cells with x above 0.35. Both V_{oc}-limitation and the recombination increase for the high-Ga devices correlate with their lack of red kinks, and are most likely due to the ΔE_c-values that are small-positive (for x just above $\sim$ 0.35) or negative (for higher Ga concentrations). Recent numerical simulations [49] also explained the V_{oc} limitation with interfacial recombination, which becomes effective when the conduction-band offset is negative or small positive.

With neither composition of the CIGS-alloy, a sufficiently large ΔE_c with CdS is formed to cause a significant barrier and a J-V distortion under the standard solar light when CdS is relatively thin. However, white-light J-V curves for the largest-spike CdS/CIS cells may show modest distortions when CdS is thick, in which case red-light distortion is quite severe. Simulations indicated that white-light distortions would occur in CdS/CIS if the buffer is relatively thick and and has a low doping concentration (lightly n-type). Decreasing CdS thickness in CdS/CIS leads to smaller secondary barriers, and thus, to less red-light distortion (and elimination of any existing small white-light J-V distortion). In fact, CdS/CIS devices with $\sim$ 20-nm CdS showed no or little red kink.

Wide-band-gap buffer layers are preferred from the point of view of photocurrent according to the *Section 4.1.* Such buffers, however, may form less favorable band-offsets. In particular, InS(O,OH)-buffer cells indicated the effects of sufficiently high secondary

barriers even with small buffer-layer thicknesses (20 nm). The indication came from reduced FF-values in the white J-V curves and from severe red kinks in such cells. Thus, it is suggested that electron affinity of the InS(O,OH) studied is relatively low, though the effective value may depend on the InS(O,OH) preparation details. The 2.8 eV effective optical band gap of InS(O,OH) was determined from the photon energy corresponding to the disappearance of the red kink in the cells, as it was discussed earlier for CdS/CIS in [46]. The InS(O,OH) band-gap value also agreed with quantum-efficiency results. This is especially relevant since the literature values for band gaps of InS-compounds vary considerably.

CIGS cells with the combined InS(O,OH)/CdS buffers showed very large J-V distortions even under white light, whereas their red-light distortions extended far into the reverse bias. The increased distortions in the white-light J-V curves of such cells with the increasing thickness of the i-ZnO layer were similar to the results on the CdS-thickness variation and are consistent with variation of the barrier height shown in the numerical simulations. The principle was also confirmed with earlier-published ZnSe/CIS results (see discussion below).

Devices with alternative ZnS(O,OH) buffers have demonstrated very high efficiencies [1, 18]. High offsets between CIGS and pure ZnS ($\Delta E_c \sim 1.4$ eV) are predicted theoretically [17] and have been measured by XPS [16]. Therefore, J-V curves for ZnS/CIGS are expected to seriously suffer from the secondary barriers. In fact, poor performance for pure-ZnS/CIGS cells was reported [16]. As discussed in *Subsection 3.1.3*, good performance of ZnS(O,OH)/CIGS cells are explained by the presence of the admixture of ZnO or $Zn(OH)_2$ with ZnS, which determines the overall properties of the CBD-ZnS(O,OH) material. The significant variation in the amount of J-V distortion ubiquitously observed

in ZnS(O,OH)/CIGS cells can be explained by slight differences in the buffer preparation details, deliberate or accidental, resulting in different amounts and/or different distributions of the secondary phases in the ZnS(O,OH) films.

Small ΔE_c-barriers may have little or no visible effect on current at room temperature. At reduced temperatures, however, charge carriers involved in current transport possess less thermal energy, and thus relatively-small ΔE_c-barriers can limit current more effectively. This was observed in red-kink distortions, which were small or absent at room temperature for thin-CdS/CIS, and CdS/1.15eV-CIGS cells, but were clearly observed at reduced temperatures.

A few words on the details of the model used: A J-V kink model alternative to the one presented here was suggested in the literature [52], in which a 'defected' p^+ CIGS-surface layer is responsible for the modifications of J-V under various illumination conditions. Though the alternative model is overall consistent with an E_c-spike, the existence of the proposed layer was not independently confirmed. It is highly unlikely that the surface CIGS layer is responsible for red/white J-V differences since CIGS band gaps are between 1.0 and 1.67 eV, whereas this work's experiments and Ref. [46] showed that it is the photon energies above the buffer band gap that are needed for red-kink removal. An additional argument against a "photoconductive" CIGS layer is the convergence of the red-light and dark J-V curves in forward bias in most cases; the only exception to this rule was seen for a few cells with serious pathologies. Our results also showed that various intensities of red light, which typically included photon energies up to 2.1 eV, yield equal amounts of red kink. In several papers, CIGS surface was suggested to be doped n-type, as discussed in *Section 2.4*. Moderate n-doping of the CIGS surface would mitigate the effects of the secondary barriers on red-light J-V somewhat, but most likely will not

seriously change the trends shown.

Previously-published results on ZnSe/$CuInSe_2$

The conduction-band model can successfully describe some of the earlier results. Fig. 4.28 shows white-light J-V curves from Ref. [4] for $CuInSe_2$ devices with two buffer combinations, ZnSe/CdS (top graph) and ZnSe/In_2O_3 (bottom graph), where in both cases the ZnSe layer of varied thickness was deposited onto CIS first. The curve for the CdS/CIS cell without ZnSe on the top graph is well-behaved. The introduction of a 20-nm ZnSe layer led to a curve with a lower FF. Curves for the cells with subsequently increasing ZnSe thickness showed an increasing amount of the distortion, and the thickest-ZnSe cell thus had J_{sc} near zero and seriously suppressed forward current in forward bias. The progression in J-V curves with varying ZnSe thickness was analogous for the In_2O_3/ZnSe/CIS cells. The In_2O_3/CIS cell without ZnSe, however, was quite poor, most likely due to the non-ideal junction interface, whereas the cell with a very thin ZnSe layer had an improved performance. These results agree qualitatively with other publications on ZnSe/CIGS cells, discussed in *Section 2.4.4*, that reported decreasing FF-values with ZnSe-thickness increase.

The authors of Ref. [4] did suspect that there might be a barrier that blocks the current, though the reason for the barrier was not proposed. The progressions in the ZnSe/CIS J-V curves in Fig. 4.28 follow the pattern discussed for CdS/InS(O,OH)/CIGS cells with the variable i-ZnO thickness under white light (*Section 4.1.4*) and CdS/CIS cells with variable CdS thickness under red light (*Section 4.2.3*). Thus, the likely reason for the barrier in the ZnSe/CIS cells is the large conduction-band spike. This explanation is qualitatively consistent with band-offset calculations by Zhang et al. [17], which predicted the ZnSe/CIS E_c-offsets near 0.9 eV (compared to 0.3–0.4 eV for CdS/CIS).

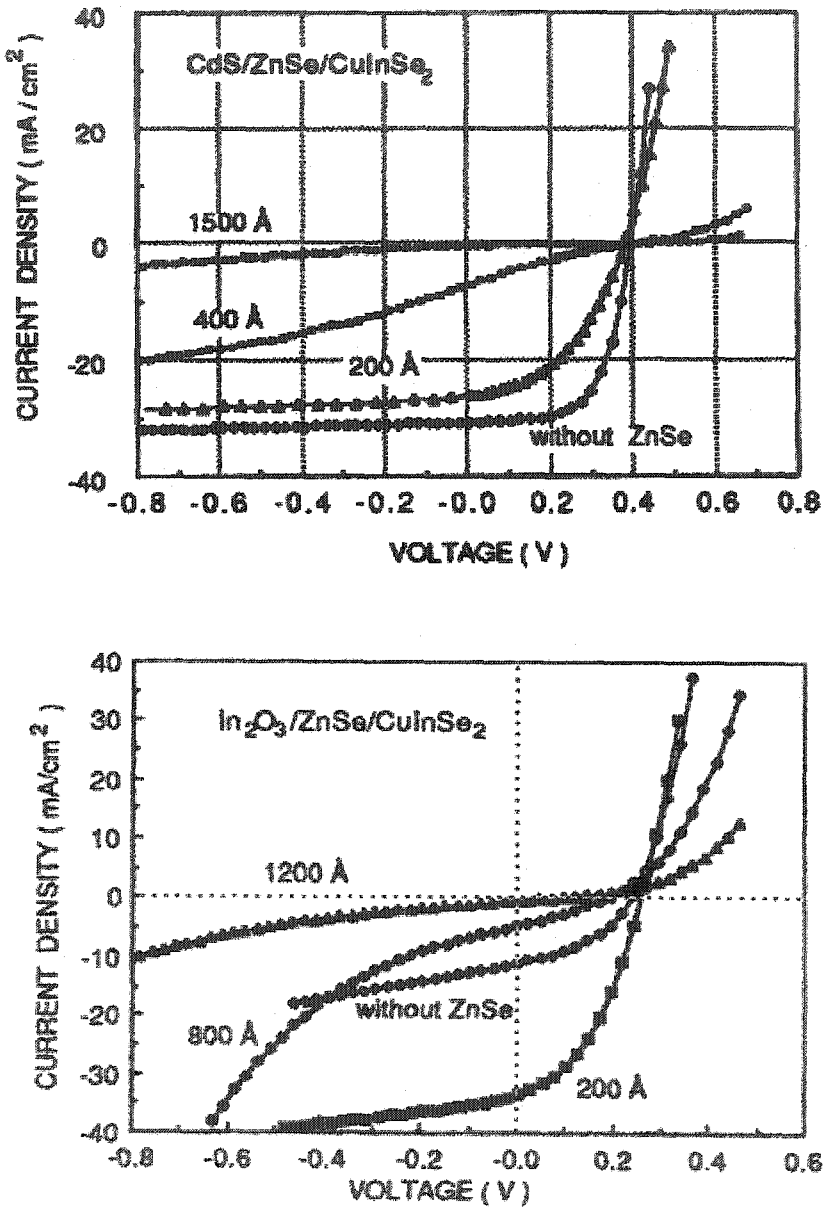

Figure 4.28: White-light J-V from Ref. [4] for (top graph) CdS/ZnSe/CIS and (bottom graph) In_2O_3/ZnSe/CIS cells with variable thicknesses of the ZnSe layer.

4.3 Effect of blue-light intensity and history on J-V

Results from the *Section 4.2* showed that J-V of most of the studied cells are well-behaved when measured with the blue photons present in the illumination spectrum, but the curves are sometimes distorted under red light. This section of the Results reports on the rates of change between red-kink and well-behaved white-light J-V. The data from the CI(G)S cells with CdS, InS(O,OH), and ZnS(O,OH) buffers will be described.

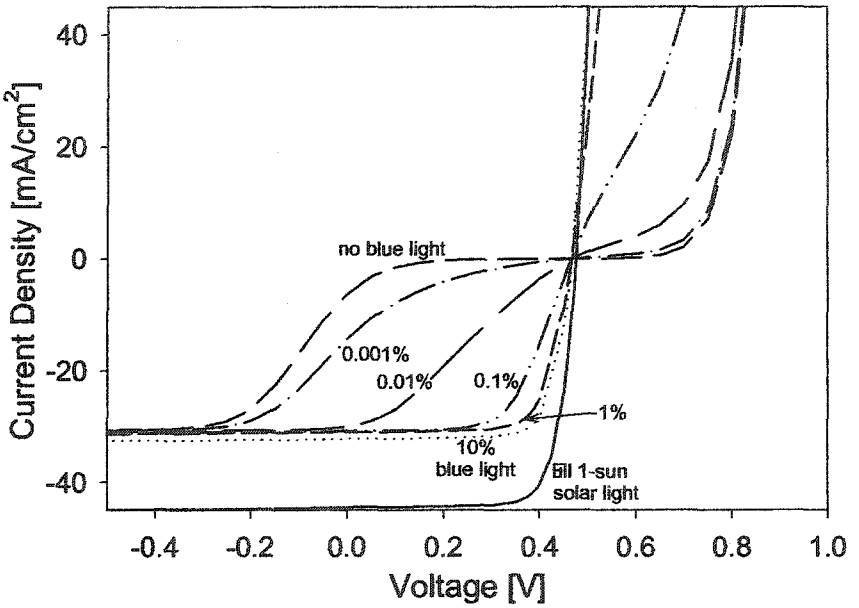

Figure 4.29: Simulated J-V curves for CdS/CIS, illuminated with full-spectrum light, red light, and intermediate "blue"-photon flux intensities.

4.3.1 Simulated reduced blue-photon flux

Figure 4.29 shows the simulated red-light and white-light J-V curves from the introduction on J-V kinks (Fig. 4.15). It also shows a series of curves with the "blue" part ($\lambda \leq$ 620 nm) of the original white-light illumination spectrum successively reduced by factors of 10. In this set of simulations, even as little as 1% of standard outdoor blue-photon flux removed most of the J-V distortion that was seen without blue light. Smaller blue-

photon intensities resulted in J-V curves intermediate to the standard diode J-V and J-V with a large kink. The J-V curves, which were produced with the AMPS-1D software, are steady-state solutions, i.e., the trapping of photogenerated electrons and holes is in equilibrium when the structure is "illuminated". Thus, each curve shown corresponds to a "long-time" exposure of a solar cell to a specified spectrum.

4.3.2 J-V transition rates in CdS/CIS cells

For the actual cells, the amount of removal of the red kink from J-V depends on both intensity and time of exposure to blue photons. Fig. 4.30(a) shows a series of experimental J-V curves from the three-stage CIS cell with 80-nm CdS buffer measured with red light subsequent to incremental exposures to the equivalent of 1-sun white light. The red-light curve prior to any white-light exposure was the most distorted. The curves gradually shifted towards the well-behaved shape with increasing time of white-light exposure. Very short exposures removed most of the distortion. The red-light curves measured after 4-min, 15-min, and 2-hr exposures did not quite match up with the well-behaved white-light curve taken only after $\sim$ 4 min of exposure, indicating that the red curves regressed in their shape slightly during the time without blue photons needed for the red-light measurement. Figure 4.30(b) shows a series of red-light curves measured as a function of the elapsed time in the dark following the white-light exposure. Without short-wavelength light available for absorption by CdS, the J-V shape returned to the large kink. The rate of the kink return was much slower, about a factor of a thousand, than the rate of kink removal under 1-sun white light.

Figure 4.31 plots the characteristic voltage $V_{1/2}$ (see Fig. 4.15[b] for definition) from

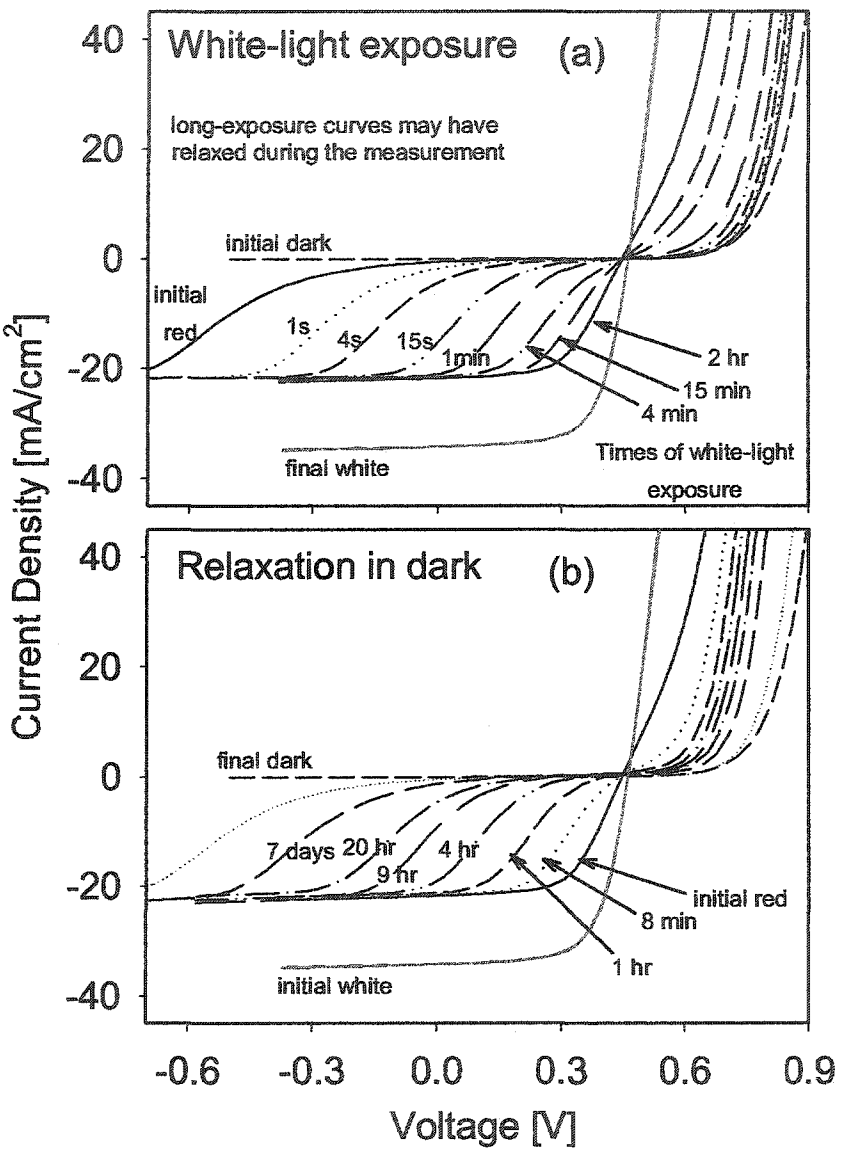

Figure 4.30: Experimental red-light J-V for a large-kink CdS/CIS cell: (a) as a function of white-light exposure time; (b) relaxation after 2-hr exposure. Well-behaved white-light curves are also shown.

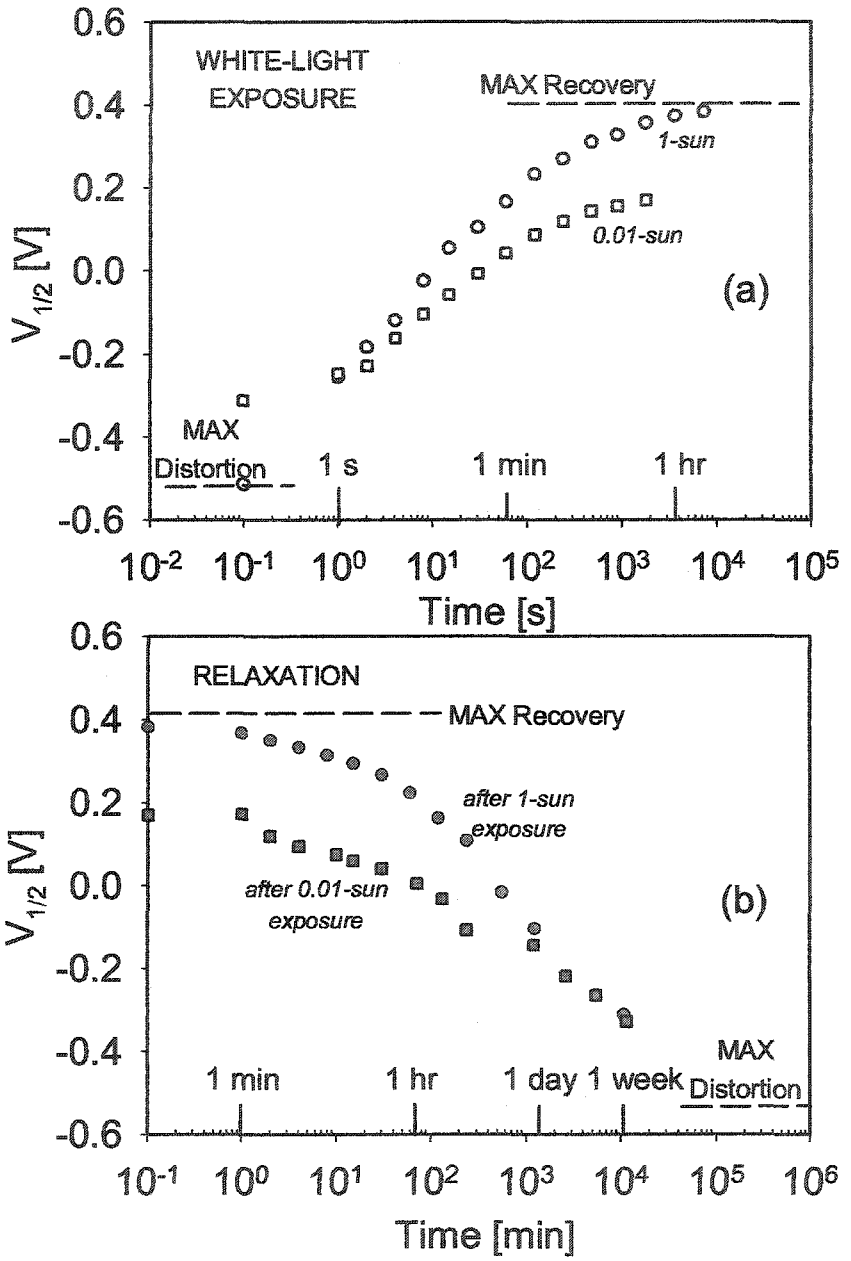

Figure 4.31: Kink voltage $V_{1/2}$ from red-light J-V curves for a large-kink CdS/CIS cell versus: (a) white-light (1-sun and 0.01 sun) exposure time; (b) relaxation time in the dark after exposures with white light of both intensities.

the J-V curves in Fig. 4.30 versus time. It also shows the $V_{1/2}$-values when the same cell was exposed to white light with intensity reduced by a factor of 100. Within approximately the first minute of white-light exposure of either intensity, the voltage increased nearly linearly with the logarithm of time until it approached its maximum. The voltage increase for the 0.01-sun intensity was slower than for the 1-sun exposure and saturated at a lower value. In fact, the kink did not entirely disappear even after a long exposure time. The smaller final value of $V_{1/2}$ subsequent to long-time exposure of the cell to white light of reduced intensity agrees qualitatively with the simulated steady-state J-V curves in Fig. 4.29. The dependence of kink re-appearance with time in the dark after the white-light exposures shown in Fig. 4.31(b) (note a different time scale) was also relatively linear with logarithm of time. The rate of kink return after the smaller-intensity exposure was slower.

4.3.3 J-V transition rates in InS(O,OH)/CIGS cells

Figure 4.32 shows the initial red-light J-V with maximum kink and a series of red-light J-V curves measured as a function of white-light exposure time for a cell with the InS(O,OH) buffer. In this case, four white-light intensities were used for the exposures: 1, 0.1, 0.01, and < 0.001 sun. The figure shows that, for the InS(O,OH)/CIGS, the reduction of the blue photon-flux to which the cell was being exposed resulted in a slower and less complete restoration of the standard diode behavior of the curve. For the reverse process with no white-light exposure, a series of red-light J-V curves (not shown) was measured as a function of time only after the 1-sun exposure. The curve took several days to return to the initial shape with the maximum kink.

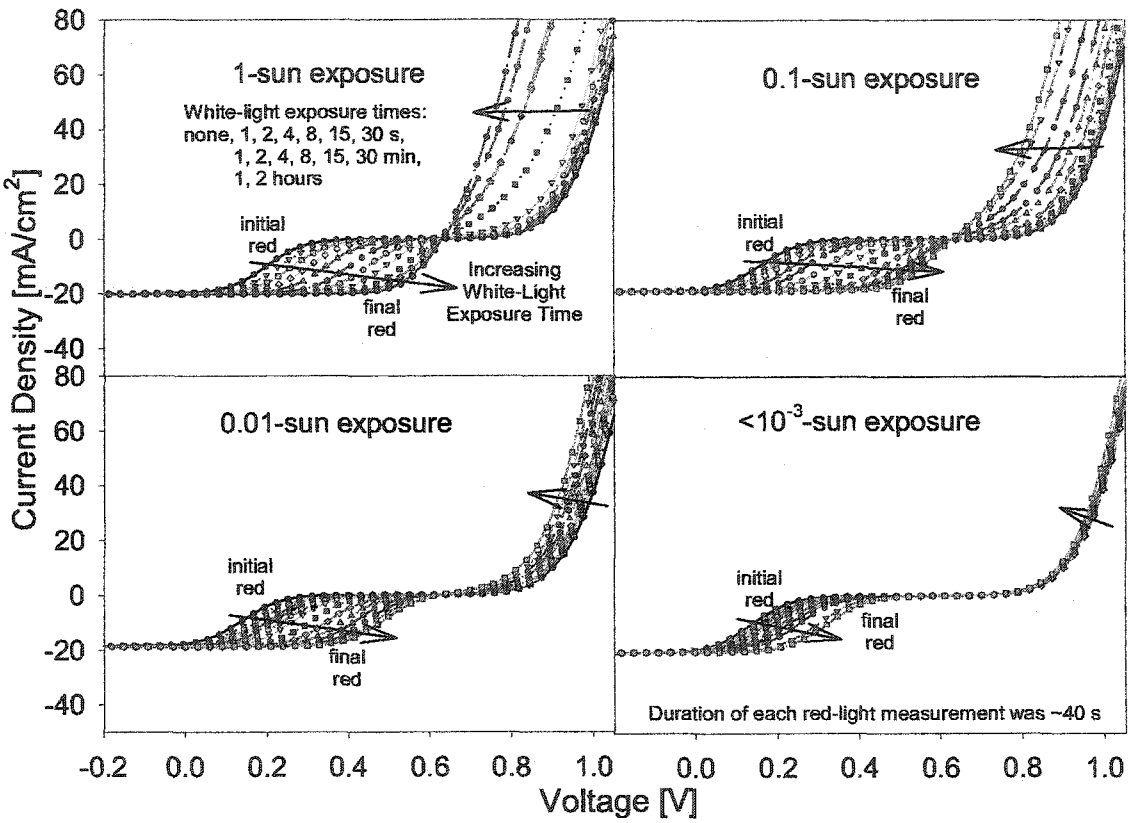

Figure 4.32: Red-light J-V for a large-kink InS(O,OH)/CIGS cell versus white-light exposure time; intensities of white light of 1, 0.1, 0.01, and $< 10^{-3}$ sun were used.

Figure 4.33(a) shows the characteristic voltage $V_{1/2}$ from J-V curves in Fig. 4.32 versus time. The graph demonstrates more explicitly that the rate of J-V recovery was greater and the recovery was more complete with greater blue-photon flux intensities contained in the white light. The character of the dependence of $V_{1/2}$ on the exposure time was qualitatively similar to that for the CdS/CIS cell from Fig. 4.31(a): the initially near-linear increase versus logarithm of time with a saturation at long times of exposure. The smaller final $V_{1/2}$-values resulting from reduced-intensity exposures, for this cell as well, were consistent with the simulations in Fig. 4.29. Fig. 4.33(b) shows the voltage relaxation after the 1-sun white-light exposure (note the different time scale). During the first hour or so, the curve retained a high $V_{1/2}$, after which time the voltage decrease with logarithm of time was steeper. This can be explained by the number of electrons in the buffer gradually decreasing and the buffer barrier increasing with time in the dark, though the J-V kink will start to show only after the barrier height reaches a certain critical value.

Finally, Fig. 4.34 shows the dependence of the time (obtained from Fig. 4.33) needed to remove the kink half-way from the InS(O,OH)/CIGS cell on the white-light illumination intensity on log-log scale. The correlation is roughly linear over several orders of magnitude, though it was more accurate for higher intensities.

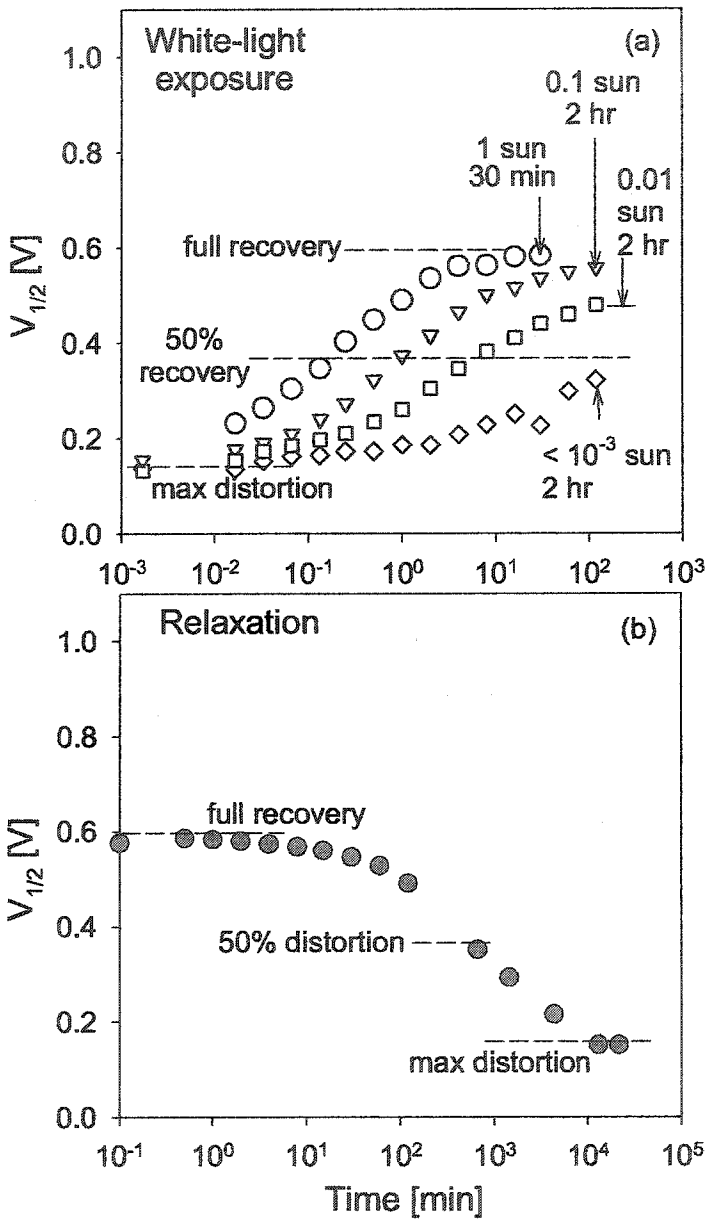

Figure 4.33: Kink parameter $V_{1/2}$ from red-light J-V curves for a large-kink InS(O,OH)/CIS cell versus: (a) time of white-light exposures with four intensities; (b) relaxation time in the dark after 1-sun white-light exposure.

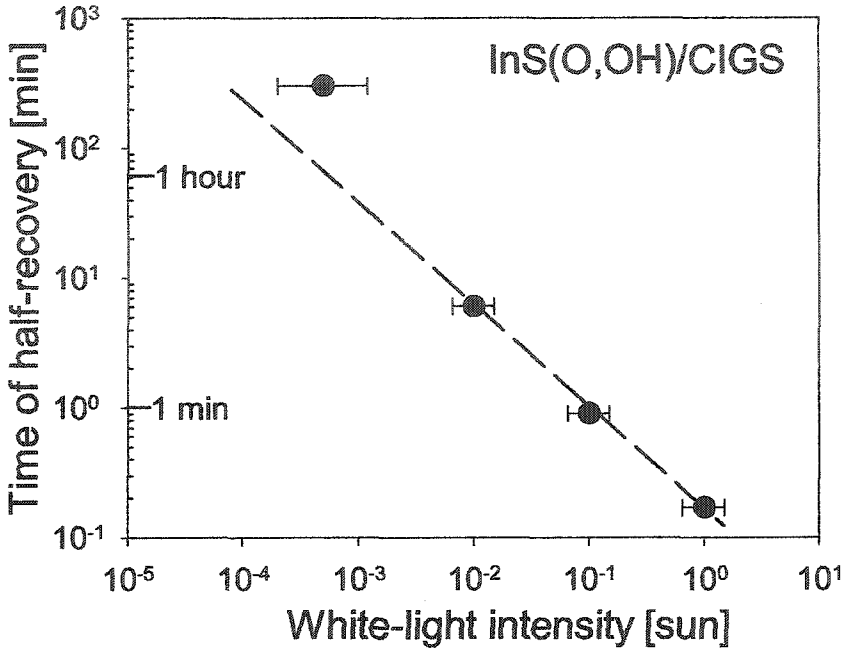

Figure 4.34: Time constant for half-removal of the kink in an InS(O,OH) cell versus intensity of white-light exposure.

4.3.4 J-V transition rates in ZnS(O,OH)/CIGS cells

Red-light J-V were measured as a function of white-light exposure times and relaxation times for the ZnS(O,OH)/CIGS cells from *Section 4.2.4* that had relatively smaller red kinks. Figure 4.35 shows the dependance of the $V_{1/2}$-values for those curves. The exposures of the cell with 1- and 0.01-sun white light were both effective in the J-V red kink removal, though the removal was faster with the greater white-light intensity. The return of the kink in the dark was quite slow; the good J-V shape maintained for up to ten hours without blue-light exposure before the kink noticeably appeared again. Both the kink removal with 1-sun exposure and the kink reappearance in the dark were considerably slower for these cells compared to cells with CdS and InS(O,OH) buffers.

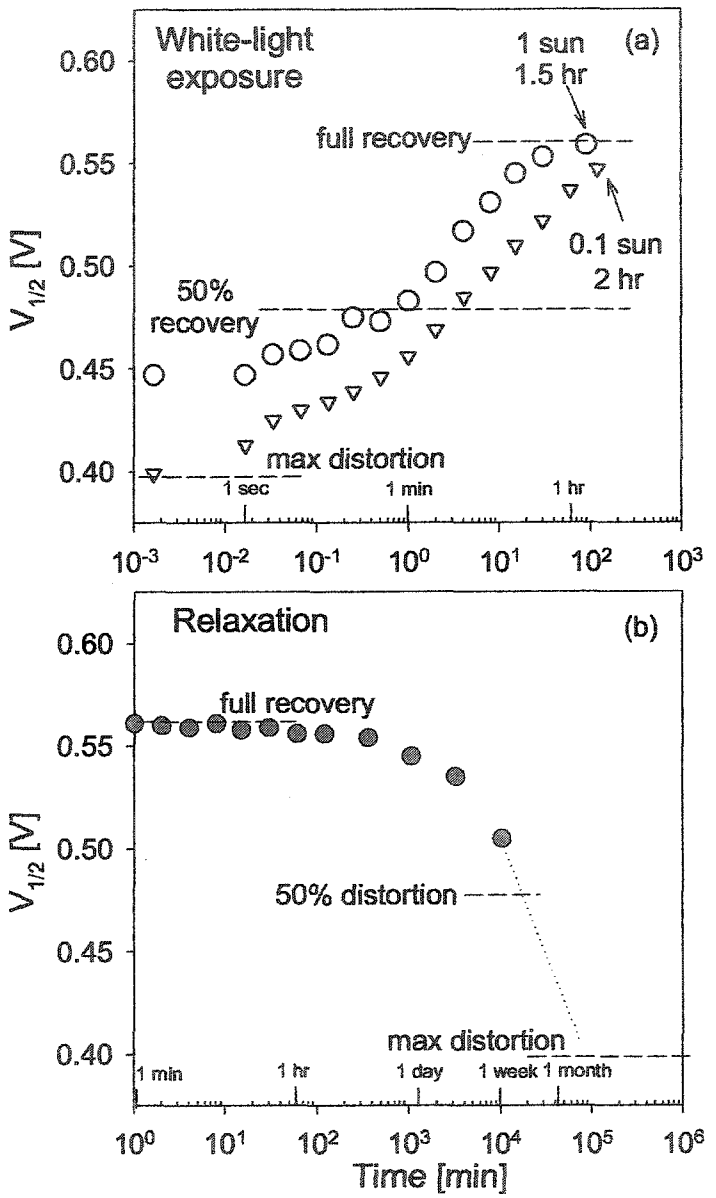

Figure 4.35: Kink parameter $V_{1/2}$ from red-light J-V curves for a ZnS(O,OH)/CIS cell versus: (a) time of white-light exposures with two intensities; (b) relaxation time in the dark after 1-sun white-light exposure.

4.3.5 Discussion on exposure to blue photons

Thin-film CIGS solar cells with various buffer materials have a similar in character response to 'blue'-light illumination, though the cutoff of the effective blue-photon region differs with the buffer band gap ($h\nu$(blue) > E_g(buffer)). For the cells with each buffer type, the shapes of J-V curves that were distorted due to increased secondary barriers when initially measured under red light, were gradually restored to a standard diode shape when exposed to white light containing blue photons. The disappearance of the kink, quantified with the characteristic voltage $V_{1/2}$, was nearly linear with logarithm of time of white-light exposures. The rate of the recovery of a good J-V shape was faster when the cells were exposed to greater blue-photon flux intensities. This was shown explicitly for InS(O,OH)/CIGS cells, in which case the time of the J-V recovery changed nearly linearly with the intensity of the exposure light on log–log scale. Similar behavior was observed in cells with CdS and ZnS(O,OH) buffers. For the reduced intensities of blue-photon exposure fluxes, the J-V recovery was slower, and it was also less complete. The times that took white light of various intensities to reduce the kink by a half ($\Delta V_1 = 1/2\ \Delta V_1$-max) in cells with the three buffer types are summarized in Table 4.1. It appears advantageous from the perspective of the solar-cell operation that the 1-sun spectrum, or one with as much as 90% reduction in blue photons, was able to remove the distortions relatively quickly (within minutes) for the reported cell structures. However, substantially-reduced photon-flux intensities were less effective. The table also shows that the kink-removal times, under identical illumination conditions, were shorter for cells with narrower buffer band gaps. This fact can be explained, at least partly, by higher total number of photons per unit of time absorbed in narrower buffers from the

Light intensity [sun]	50% change in distortion		
	CdS	InS(O,OH)	ZnS(O,OH)
1	10 s	10 s	1 min
0.1	not done	1 min	4 min
0.01	20 s	6 min	not done
$<10^{-3}$	not done	5 hr	not done
Zero (relaxation)	10 hr	10 hr	8 days

Table 4.1: Half-time constants for kink removal under white light of various intensities and for kink return in the dark.

same white-light spectrum, and thus faster kink removal by greater photon fluxes, which is consistent with Fig. 4.34. The assumption here is that the values for the densities of deep acceptors for all of these buffer materials and their properties are close.

In the absence of high-energy photons, J-V curves resume the distorted shapes over period of time the order of hours or days. The corresponding times for the three cell types, also shown in the table, were factors 10^3 – 10^4 longer than the times for kink removal by 1-sun light. This is also advantageous for the solar-cell operation, and is a logical result of the strong asymmetry between electron and hole capture rates in the buffer. The relaxation times were considerably longer for the ZnS(O,OH)-buffer cells, compared to the other two cell types. A slower rate of J-V relaxation, according to our model, should be due to a slower electron-capture rate in the buffer. The lower relaxation rate, however, may also be partially due relatively small maximum J-V distortion amount found in the particular ZnS(O,OH) cells.

The dependence of performance of thin-film solar cells on the spectral content of the illumination, reported here, is relevant to the operation of the cell modules outdoors, where they are exposed to variable light intensities, including reduced blue-photon fluxes. However, the results are especially central to tandem solar cells where the wider-gap top cells ($E_g \sim 1.7$ eV) absorb almost all photons above its band gap, and the narrow-

gap bottom cells receive only "red" light with $h\nu < E_g$(top cell). $CuInSe_2$ cells were recently proposed as bottom cells for thin-film tandems (outlined in [53]). Based on the results reported here, it is thus recommended to design at least a partial transmission of blue photons through the top cells unto the bottom CIS cells to insure CIS cell kink removal. The second demonstrated tactic of removing red kinks from large-spike CdS/CIS cells, according to *Section 4.2.3*, is thinning of CdS or i-ZnO, in which case the effective secondary barriers will also be reduced.

Chapter 5

Conclusions

The current-transport mechanisms governing thin-film $Cu(In,Ga)Se_2$ solar cells were described in this thesis with a relatively straightforward junction model that was extended onto various CIGS band gaps and several buffer-layer choices. It was shown that the conduction-band offset (ΔE_c) between CIGS absorber and the buffer is crucial for solar-cell performance. Large positive offsets (spikes) above 0.5 eV can limit both forward and reverse photogenerated currents [48, 49]. Smaller spikes can also form current barriers if the buffer material is only lightly doped n-type *or* heavily compensated. In the latter case, distortions, or more pronounced distortions, in J-V curves due to current blockage are seen under "red" illumination consisting of photons with energies below the buffer band gap.

This principle was verified through examination of the $CdS/CuIn_{1-x}Ga_xSe_2$ solar cells with variable x, which provide a large range of ΔE_c-values between the buffer and absorber naturally: from moderately positive (spike) in CdS/CIS to moderately negative (cliff) in CdS/CGS. Consequently, there was a varying amount of the red-kink distortion

in the J-V curves of these cells. The kink was strongest in CdS/CIS and it decreased with the increasing Ga concentration. The measurements showed that the CIGS band gap value, at which $\Delta E_c = 0$ (no red kink), is near 1.2 – 1.3 eV.

Regular white-light J-V and QE measurements on the same cells showed that the CIGS band gap increased linearly with x. The band-gap increase resulted in J_{sc} decrease and V_{oc} increase. V_{oc}, however, failed to increase proportionally with band gap above 1.2 eV, which was analogous to the known results reported by others on cells with Al- and Ga-alloys of CIS. According to numerical simulations of Ref. [49], the lack of V_{oc} increase with band gap can be caused by cliffs or small spikes in the conduction band at the junction, in which case the interfacial recombination plays a significant role. Our experimental results, in fact, showed that all cells with $E_g > 1.2$ eV, where V_{oc} was lower than expected, also had relatively-high diode-quality factors of $A \approx 2.1$ compared to $A \approx 1.5$ for the cells with $E_g \leqslant 1.2$. High A-values are thus likely due to interfacial recombination, and the CdS/CIGS ΔE_c transition from positive to negative is likely somewhat above E_g(CIGS) = 1.2 eV. This value is similar to the one from the red-light J-V measurements.

Severe J-V kinks under red light for CI(G)S solar cells with moderate spikes in the junction can be avoided through adjusting the thicknesses of the buffer layers, such as CdS and i-ZnO. In particular, the numerical simulations of the CdS/CIS junction showed that the height of the secondary barrier in the absence of blue photons is greater for thicker compensated-CdS or i-ZnO. The experimental results were consistent with the simulation predictions. In CdS/CIS cells, decreasing red kinks were observed with decreased CdS thickness. In fact, CIS cells with 15-20 nm CdS showed no or very little red-light distortion. Additional evidence for this principle was found in CdS/InS(O,OH)/CIGS

cells, which showed relatively large J-V kinks even under white light, and the kinks were larger with thicker i-ZnO. The principle was also applied to interpret the data from Ref. [4], in which the amount of white-light J-V distortion for ZnSe/CIS cells (ΔE_c from theory near 0.9 eV) was increasing with the ZnSe layer thickness.

Despite the partial photon loss in CdS buffers, CdS/CIGS ($E_g \sim 1.15$ eV) cells have the highest efficiency for thin-film solar cells to-date [14]. Use of alternative wider-gap buffers, such as ZnS(O,OH) or InS(O,OH) described in this work, leads to a reduction of the short-wavelength photon loss. The InS(O,OH)/CIGS solar cells studied, however, showed the formation of high secondary junction barriers, which distorted red-light, and in some cases, even white-light J-V. Thus, there was a strong suggestion that the electron affinity of the InS(O,OH) films was relatively low. Best ZnS(O,OH)/CIGS solar cells have demonstrated the efficiencies [18] that closely approached those for the best CdS devices. It appears however, that the best results require sufficient amounts of the oxide and/or hydroxide phases in the buffer material in order to avoid high buffer/absorber conduction-band spikes. Cells with both alternative ZnS(O,OH) and standard CdS demonstrate a clear potential of reaching, and hopefully surpassing the 20%-efficiency milestone for thin-film cells in the near future.

"Blue" light, absorbed in the buffers, is essential for the solar-cell operation since it lowers the secondary barriers through the buffer photoconductivity and removes or substantially reduces J-V distortions. It was shown that the blue photons contained in the standard solar light removed the kinks from the J-V curves of CIGS cells with CdS, InS(O,OH), and ZnS(O,OH) buffer layers within minutes. The reduction of the blue-flux intensity leads to slower and less complete barrier suppression and J-V recovery. This fact explains a slower J-V recovery of the cells with wider-gap buffers under identical

white light, since such buffers absorb a smaller fraction of the solar spectrum. The reverse processes of relaxation to initial kink behavior in the absence of blue light were some $10^3 - 10^4$ times slower, depending on the buffer, than the J-V recovery under one sun. This natural consequence of the large asymmetry of capture rates of photogenerated electrons and holes in the buffer is advantageous for the regular operation of solar cells. The effect of the buffer photoconductivity on solar-cell performance was also used in this work to determine optical band gaps of buffers from whole-device measurements; specifically, E_g(InS(O,OH)) $\sim$ 2.8 eV was thus obtained.

A few practical implications of the results of this thesis may be of immediate interest in the field. (1) Higher V_{oc}-values in CdS/CGS or high-Ga CdS/CIGS should be obtained with the replacement of CdS with a buffer with smaller electron affinity χ, and InS(O,OH) may likely meet this requirement. (2) The relatively-large spike in CdS/CIS junctions could pose a practical problem for the utilization of CdS/CIS as the bottom junctions in thin-film solar-cell tandems. This issue, however, can be approached at least in two ways. First, even a fraction of solar-spectrum blue photons can be effective in removing the distortion from the CdS/CIS diode curves. Designing the tandem top cell to partially transmit high-energy photons is, therefore, recommended. Second, making the buffer layer(s) thinner can effectively reduce secondary barriers, and restore the standard behavior to the red-light J-V curves of CdS/CIS solar cells.

Bibliography

[1] A. Pudov, J. Sites, and T. Nakada. Performance and loss analyses of high-efficiency chemical bath deposition (CBD)-ZnS/$CuIn_{1-x}Ga_xSe_2$ thin-film solar cells. *Jpn. J. Appl. Phys.*, 41:L672–L674, June 2002.

[2] J.R. Sites. Quantification of losses in thin-film polycrystalline solar cells. In *Proc. 12^{th} International Photovoltaic Science and Engineering Conference*, page 627, June 2001.

[3] F.S. Hasoon. *to be published.*

[4] J.-B. Yoo, A.L. Fahrenbruch, and R.H. Bube. Preparation and properties of $CuInSe_2$ solar cells with ZnSe intermediate layer. In *Proc. 20^{th} IEEE Photovoltaic Specialist Conf.*, pages 1431–1436, 1988.

[5] C. Persson and A. Zunger. Anomalous Grain Boundary Physics in Polycrystalline $CuInSe_2$: The Existence of a Hole Barrier. *Phys. Rev. Let.*, 91(16):266401, 2003.

[6] I. Visoly-Fisher, S. R. Cohen, A. Ruzin, and D. Cahen. How Polycrystalline Devices Can Outperform Single-Crystal Ones: Thin Film CdTe/CdS Solar Cells. *Advanced Materials*, 16(11):879–883, June 2004.

[7] J.H. Werner, J. Mattheis, and U. Rau. Efficiency Limitations of Polycrystalline Thin Film Solar Cells: Case of $Cu(In,Ga)Se_2$. *Accepted to Thin Solid Films*, 2004.

[8] W. Shockley and H.J. Queisser. *J. Appl. Phys.*, 32:510–519, 1961.

[9] J.E. Granata. *The impact of deliberate sodium incorporation on $CuInSe_2$-based solar cells.* PhD thesis, Colorado State University, Spring 1999.

[10] S. B. Zhang, S.-H. Wei, A. Zunger, and H. Katayama-Yoshida. *Phys. Rev. B*, 57: 9642–9656, 1998.

[11] S.-H. Wei, S. B. Zhang, and A. Zunger. Effects of Ga addition to $CuInSe_2$ on its electronic, structural, and defect properties. *Appl. Phys. Lett.*, 72:3199–3201, 1998.

[12] A. Yamada, S. Chaisitsak, Y. Ohtake, and M. Konagai. High efficiency $cu(in,ga)se_2$ thin-film solar cells with novel $znin_xse_y$ buffer layer. In *Proc. 2^{nd} World Conf. Photovoltaic Energy Conversion*, volume 1, pages 1177–1180, 1998.

[13] A. Ennaoui, W. Eisele, M. Ch. Lex-Steiner, W. Riedl, and F. Karg. Cd-free Cu(Ga,In)$(SSe)_2$ Thin Film Solar Cells and Mini-modules. In *16th European Photovoltaic Sol. Energy Conf.*, pages 682–685, 2000.

[14] K. Ramanathan, G. Teeter, J.C. Keane, and R. Noufi. Properties of High Efficiency $CuInGaSe_2$ (CIGS) Thin Film Solar Cells. *Article in press in Thin Solid Films*, 2004.

[15] K. Ramanathan, H. Wiesner, S. Asher, D. Niles, R. N. Bhattacharya, J. Keane, M. A. Contreras, and R. Noufi. *Proc. of the 2nd World PVSEC Conf.*, page 477, 1998.

[16] T. Nakada, M. Hongo, and E. Hayashi. Band offset of high efficiency CBD-ZnS/CIGS thin film solar cells. *Thin Solid Films*, 431-432:242–248, 2003.

[17] S. B. Zhang, S. H. Wei, and A. Zunger. *J. Appl. Phys.*, 83:3192–3196, 1998.

[18] M. A. Contreras, T. Nakada, M. Hongo, A. O. Pudov, and J. R. Sites. ZnO/ZnS(O,OH)/Cu(In,Ga)Se_2/Mo solar cell with 18.6% efficiency. In *Proc. 3rd World Conf. Photovoltaic Energy Conversion*, pages 570–573, 2003.

[19] T. Nakada and M. Mizutani. Improved efficiency of Cu(In,Ga)Se_2 thin film solar cells with chemically deposited ZnS buffer layers by air-annealing -formation of homojunction by solid phase diffusion-. In *Proc. 28th IEEE Photovoltaic Specialist Conf.*, pages 529–534, September 2000.

[20] A.M. Fernández and P.J. Sebastian. Conversion of chemically deposited ZnS films to photoconducting ZnO films. *J. Phys. D: Appl. Phys.*, 26:2001–2006, 1993.

[21] R.A. Mickelsen, B.J. Stanbery, J.E. Avery, and W.S. Chen. Large area $CuInSe_2$ thin-film solar cells. In *Proc. 19th IEEE Photovoltaic Specialist Conf.*, pages 744–748, 1987.

[22] B. Dimmler, H. Dittrich, and H.-W. Schock. Structure and morphology of evaporated bilayer and selenized $CuInSe_2$ films. In *Proc. 20th IEEE Photovoltaic Specialist Conf.*, pages 1426–1430, 1988.

[23] K. Urabe, T. Hama, M. Roy, H. Sato, H. Fujisawa, M. Ohsawa, Y. Ichikawa, and H. Sakai. Properties of $CuInSe_2$ films for solar cell applications. In *Proc. 22nd IEEE Photovoltaic Specialist Conf.*, pages 1082–1087, 1991.

[24] D. Lincot, E.B. Yousfi, B. Canava, P. Cowache, and J.F. Guillemoles. Interfacial engineering of $CuIn_{1-x}Ga_xSe_2$ thin film solar cells based on atomic layer epitaxy. In *Proc. 16th European Photovoltaic Sol. Energy Conf.*, 2000.

[25] D. Hariskos, M. Ruckh, U. Rühle, T. Walter, and H.-W. Schock. A novel cadmium free buffer layer for $CuIn_{1-x}Ga_xSe_2$ based solar cells. In *Proc. 24th IEEE Photovoltaic Specialist Conf.*, 1994.

[26] T. Minemoto, H. Takakura, Y. Hamakawa, Y. Hashimoto, S. Nishiwaki, and T. Negami. Highly efficient Cd-free Cu(In,Ga)Se_2 solar cells using novel window later of (Zn,Mg)O films. In *Proc. 16th European Photovoltaic Sol. Energy Conf.*, pages 686–689, 2000.

[27] N. Dhere, D. Waterhouse, K. Sundaram, O. Melendez, N. Parikh, and B. Patnaik. Solution-grown CdS layers for polycrystalline-thin-film solar cells. In *Proc. 23rd IEEE Photovoltaic Specialist Conf.*, pages 566–571, 1993.

[28] M. A. Contreras, J. Tuttle, A. Gabor, A. Tennant, K. Ramanathan, S. Asher, A. Franz, J. Keane, L Wang, J. Scofield, and R. Noufi. High efficiency Cu(In,Ga)Se_2-based solar cells: processing of novel absorber structures. In *Proc. 24th IEEE Photovoltaic Specialist Conf.*, pages 68–75, 1994.

[29] M. A. Contreras, J. Tuttle, A. Gabor, A. Tennant, K. Ramanathan, S. Asher, A. Franz, J. Keane, L Wang, and R. Noufi. High efficiency graded bandgap thin-film polycrystalline $CuIn_{1-x}Ga_xSe_2$-based solar cells. *Sol. Energy Mat. Sol. Cells*, 41-42: 231–246, 1996.

[30] U. Rau and H. W. Schock. *Appl. Phys. A*, 69:131–147, 1999.

[31] D. Hariskos, M. Ruckh, U. Rühle, T. Walter, H.W. Schock, J. Hedström, and L. Stolt. *Sol. Energy Mat. Sol. Cells*, 41, 1996.

[32] R.H. Mauch, M. Ruckh, J. Hedström, D. Lincot, J. Kessler, R. Klinger, L. Stolt, J. Vedel, and H.W. Schock. *Proc. 9th European Photovoltaic Sol. Energy Conf.*, page 1415, 1991.

[33] ESTM E892.

[34] W. N. Shafarman, R. Klenk, and B. E. McCandless. *J. Appl. Phys.*, 79:7324–7328, 1996.

[35] H. W. Schock, U. Rau, T. Dullweber, G. Hanna, M. Balboul, T. Margorian-Friedlmeier, A. Jasenek, I. Kötschau, H. Kerber, and H. Wiesner. In *Proc. 16th European Photovoltaic Sol. Energy Conf.*, pages 304–308, 2000.

[36] J. Malmström, J. Wennerberg, M. Bodegård, and L. Stolt. In *Proc. 17th European Photovoltaic Sol. Energy Conf.*, pages 1265–1268, 2001.

[37] T. Minemoto, Y. Hashimoto, W. Shams-Kolahi, T. Satoh, T. Negami, H. Takakura, and Y. Hamakawa. *Sol. Energy Mat. Sol. Cells*, 75:121–126, 2003.

[38] W.N. Shafarman, S. Marsillac, P.D. Paulson, H.W. Haimdodi, T. Minemoto, and R.W. Birkmire. In *Proc. 29th IEEE Photovoltaic Specialist Conf.*, pages 519–522, 2002.

[39] S. Marsillac, P.D. Paulson, M.W. Haimdodi, R.W. Birkmire, and W.N. Shafarman. *Appl. Phys. Lett.*, 81(7):1350–1352, 2002.

[40] J. R. Sites and P. H. Mauk. *Solar Cells*, 27:411–417, 1989.

[41] J.E. Granata, J.R Sites, G. Puente-Contreras, and A.D. Compaan. Effect of CdS thickness on CdS/CdTe quantum efficiency. In *Proc. 25th IEEE Photovoltaic Specialist Conf.*, page 853, 1996.

[42] K. Ramanathan, M. A. Contreras, C. L. Perkins, S. Asher, F. S. Hasoon, J. Keane, D. Young, M. Romero, W. Metzger, R. Noufi, J. Ward, and A. Duda. Properties of 19.2% efficiency ZnO/CdS/$CuInGaSe_2$ thin-film solar cells. *Prog. Photovoltaics*, 11: 225–230, 2003.

[43] D. Schmidt, M. Ruckh, and H.-W. Schock. In *Proc. 1st World Conf. Photovoltaic Energy Conversion*, page 198, 1994.

[44] S.-H. Wei and A. Zunger. *Appl. Phys. Lett.*, 63:2549–2551, 1993.

[45] A. Kanevce, M. Gloeckler, A.O. Pudov, and J.R. Sites. *to be published.*

[46] I. L. Eisgruber, J. E. Granata, J. R. Sites, J. Hou, and J. Kessler. *Sol. Energy Mat. Sol. Cells*, 53:367–377, 1998.

[47] M. Burgelman, F. Engelhardt, J.F. Guillemoles, R. Herberholz, M. Igalson, R. Klenk, M. Lampert, T. Meyer, V. Nadenau, A. Niemegeers, J. Parisi, U. Rau, H.W. Schock, M. Schmitt, O. Seifert, T. Walter, and S. Zott. *Prog. Photovoltaics*, 5:121, 1997.

[48] A. Niemegeers, M. Burgelman, and A. DeVos. *Appl. Phys. Lett.*, 67:843–845, 1995.

[49] M. Gloeckler and J. R. Sites. Efficiency limitations for wide-band-gap chalcopyrite solar cells. *Accepted to Thin Solid Films.*

[50] A. Niemegeers, M. Burgelman, R. Herberholz, U. Rau, D. Hariskos, and H. W. Schock. *Prog. Photovoltaics*, 6:407–421, 1998.

[51] M. Gloeckler, C. R. Jenkins, and J. R. Sites. *Mat. Res. Soc. Symp. Proc.*, 763: 231–236, 2003.

[52] M. Igalson, M. Modegârd, L. Stolt, and A. Jasenek. The 'defected layer' and the mechanism of the interface-related metastable behavior in the ZnO/CdS/$Cu(In,Ga)Se_2$ devices. *Thin Solid Films*, 431-432:153–157, 2003.

[53] T.J. Couts, S. Ward, D. Young, K. Emery, T. Gessert, and R. Noufi. *Prog. Photovoltaics*, 11:359–375, 2003.

Extended bibliography on CIGS solar cells with various buffer layers from *Section 2.4* (until early 2003).

In_2S_3

D. Lincot et al., Buffer Layers for Cu(In,Ga)(S,Se)$_2$/BF/ZnO Solar Cells, In Proc. 13th European Photovoltaic Sol. Energy Conf. (1995), p. 1995

F. Karg et al., CIS-Module Development within the FORSOL Program: Structure and First Results, In Proc. 14th European Photovoltaic Sol. Energy Conf.(1997), p. 2012.

$In_x(OH,S)_y$

D. Hariskos et al., A Novel Cadmium Free Buffer Layer for Cu(In,Ga)Se$_2$ Based Solar Cells. (1) In Proc. 24th IEEE Photovoltaic Specialist Conf. (1994), p. 91 (data). (2) In Proc. 13th European Photovoltaic Sol. Energy Conf. (1995), p. 1995.

Y. Tokita et al., High Efficiency Cu(In,Ga)Se$_2$ Thin-Film Solar Cells with Novel $ZnIn_xS_y$ Buffer Layer, In Proc. 12th International Photovoltaic Science and Engineering Conf. (Jeju, Korea, 2001), p. 95.

C. Kaufmann et al., Growth Analysis of Chemical Bath Deposited $In(OH)_xS_y$ Films as Buffer Layers for $CuInS_2$ Thin Film Solar Cells, In Proc. 28th IEEE Photovoltaic Specialist Conf. (2000), p. 688.

C.H. Huang et al., A Comparative Study of Chemical-bath-deposited CdS, (Cd,Zn)S, ZnS, and $In(OH)_xS_y$ Buffer Layer for CIS-based Solar Cells, In Proc. 28th IEEE Photovoltaic Specialist Conf. (2000), p. 696.

ZnS(O,OH)

K. Kushiya et al., Development of Cu(In,Ga)Se$_2$ Thin-Film Solar Cells with Zn-Compound Buffer, In Proc. 13th European Photovoltaic Sol. Energy Conf. (1995), p. 2016.

K. Kushiya et al., Formation of Robust Junction Between Cu(In,Ga)Se$_2$-Based Absorber and $Zn(O,S,OH)_x$ Buffer Prepared on a 30cmx30cm Submodule, In Proc. 28th IEEE Photovoltaic Specialist Conf. (2000), p. 424.

T. Nakada and M. Mizutani, Improved Efficiency of Cu(In,Ga)Se$_2$ Thin Film Solar Cells with Chemically Deposited ZnS Buffer Layers by Air-Annealing -Formation of Homojunction by Solid Phase Diffusion-, In Proc. 28th IEEE Photovoltaic Specialist Conf. (2000), p.529.

H.-J. Muffler et al., ILGAR Technology, VIII Sulfidic Buffer Layers for Cu(In,Ga)(S,Se)$_2$ Solar Cells Prepared by Ion Layer Gas Reaction (ILGAR), In Proc. 28th IEEE Photovoltaic Specialist Conf. (2000), p. 610.

A.Ennaoui et al., Cd-Free Cu(Ga,In)(S,Se)$_2$ Thin Film Solar Cells and Mini-modules, In Proc. 16th European Photovoltaic Sol. Energy Conf. (2000), p.682.

C.H. Huang et al, A Comparative Study of Chemical-bath-deposited CdS, (Cd,Zn)S, ZnS, and $In(OH)_xS_y$ Buffer Layer for CIS-based Solar Cells, In Proc. 28^{th} IEEE Photovoltaic Specialist Conf. (2000), p. 696.

B. Sang et al., Investigation of Chemical-Bath-Deposited ZnS Buffer Layers for $Cu(In,Ga)Se_2$ Thin Film Solar Cells, In Proc. 29^{th} IEEE Photovoltaic Specialist Conf. (2002), p.632.

M.Contreras, T. Nakada et al., 18.6% CBD-ZnS/CIGS record non-Cd thin film solar cell, In Proc. 3^{rd} World Conf. Photovoltaic Energy Conversion (2003), p. 570.

CdZnS

R.A. Mickelsen et al., Large Area $CuInSe_2$ Thin-Film Solar Cells, In Proc. 19^{th} IEEE Photovoltaic Specialist Conf. (1987), p. 744.

B. Dimmler et al., Structure and Morphology of Evaporated Bilayer and selenized $CuInSe_2$ Films, In Proc. 20^{th} IEEE Photovoltaic Specialist Conf. (1988), p. 1426.

K. Urabe et al., Properties of $CuInSe_2$ Films for Solar Cell Applications, In Proc. 25^{th} IEEE Photovoltaic Specialist Conf. (1996), p. 893.

C.H. Huang et al., A Comparative Study of Chemical-bath-deposited CdS, (Cd,Zn)S, ZnS, and $In(OH)_xS_y$ Buffer Layer for CIS-based Solar Cells, In Proc. 28^{th} IEEE Photovoltaic Specialist Conf. (2000), p. 696.

Superstrate CdS

T. Nakada et al., Superstrate-Type $Cu(In,Ga)Se_2$ Thin Film Solar Cells with ZnO Buffer Layer - a Novel Approach to 10% Efficiency, In Proc. 2^{nd} World Conf. Photovoltaic Energy Conversion (1998), p.413.

R.W. Birkmire et al., Options for Fabrication and Design of $CuInSe_2$ Based Solar Cells , In Proc. 21^{st} IEEE Photovoltaic Specialist Conf. (1990), p. 550.

ZnO

M. Bar et al., ILGAR-ZnO Window Extension Layer: An Adequate Substitution of the Conventional CBD-CdS Buffer in $Cu(In,Ga)(S,Se)_2$ - based Solar Cells with Superior Device Performance, Prog. Photovoltaics 2002, 10:173-184; In Proc. 29^{th}IEEE Photovoltaic Specialist Conf. (2002); In Proc. 12^{th} International Photovoltaic Science and Engineering Conf. (2001), p.489.

T. Minemoto et al., Highly Efficient Cd-Free $Cu(In,Ga)Se_2$ Solar Cells Using Novel Window Layer of (Zn,Mg)O Films, In Proc. 16^{th} European Photovoltaic Sol. Energy Conf. (2000), p.686; 28^{th} IEEE Photovoltaic Specialist Conf. (2000), p.634.

K. Ramanathan et al., (Properties of Cd and Zn Partial Electrolyte Treated CIGS Solar Cells), (1) In Proc. 29^{th} IEEE Photovoltaic Specialist Conf. (2002); (2) In Proc. 2^{nd} World Conf. Photovoltaic Energy Conversion p.477; (3) P. Johnson et al. In Proc. 29^{th} IEEE Photovoltaic Specialist Conf. (2002).

A. Yamada et al., Buried homojunction in Cu(In,Ga)Se_2 Solar Cells Formed by Intentional Zn Doping, (1) In Proc. 28^{th} IEEE Photovoltaic Specialist Conf. (2000), p.462; (2) S. Chaisitsak et al., In Proc. 12^{th} International Photovoltaic Science and Engineering Conf. (2001), p. 97.

L. Olson et al., High Efficiency CIGS and CIS cells with CVD ZnO Buffer Layers, (1) In Proc. 26^{th} IEEE Photovoltaic Specialist Conf. (1997), p.363; (2) In Proc. 28^{th} IEEE Photovoltaic Specialist Conf. (2000), p. 458; (3) In Proc. 24^{th} IEEE Photovoltaic Specialist Conf. (1994), p.194.

J. Kessler et al.,Interface Engineering Between $CuInSe_2$ and ZnO, In Proc. 23^{th} IEEE Photovoltaic Specialist Conf. (1993), p.447.

J. Sterner et al., Atomic Layer Epitaxy Growth of ZnO Buffer Layers in Cu(In,Ga)Se_2 Solar Cells, In Proc. 2^{nd} World Conf. Photovoltaic Energy Conversion (1998), p.1145.

T. Nakada et al., Superstrate-Type Cu(In,Ga)Se_2 Thin Film Solar Cells with ZnO Buffer Layer - a Novel Approach to 10% Efficiency, In Proc. 2^{nd} World Conf. Photovoltaic Energy Conversion (1998), p.413.

SnO_2

D. Hariskos et al., Buffer Layers for Cu(In,Ga)(S,Se)$_2$/BF/ZnO Solar Cells, In Proc. 13^{th} European Photovoltaic Sol. Energy Conf. (1995), p. 1995.

In_2Se_3

Y. Ohtake, A.Yamada et al., High Efficiency $CuIn_{1-x}Ga_xSe_2$ Thin-Film Solar Cells with Novel $ZnIn_xSe_y$ Buffer Layer, (1) In Proc. 2^{nd} World Conf. Photovoltaic Energy Conversion (1998), p. 1177; (2) In Proc. 25^{th} IEEE Photovoltaic Specialist Conf. (1996), p. 793.

Se Han Kwon et al., Growth of $CuIn_3Se_5$ Layer on the $CuInSe_2$ Film and its Effect on the Photovoltaic Properties of $In_2Se_3/CuInSe_2$ Solar Cells, In Proc. 26^{th} IEEE Photovoltaic Specialist Conf. (1997), p. 395.

T. Nakada et al., Superstrate-Type $CuInSe_2$ Thin Film Solar Cells with Selenide Buffer Layers, In Proc. 25^{th} IEEE Photovoltaic Specialist Conf. (1996), p. 893.

$ZnIn_2Se_4$

A. Delahoy et al., Ternary Source Materials for CIGS Buffer Layers, In Proc. 16^{th} European Photovoltaic Sol. Energy Conf. (2000), p.767.

Y. Ohtake, A.Yamada et al., High Efficiency Cu(In,Ga)Se_2 Thin-Film Solar Cells with Novel $ZnIn_xSe_y$ Buffer Layer, (1) In Proc. 2^{nd} World Conf. Photovoltaic Energy Conversion (1998), p. 1177; (2) In Proc. 25^{th} IEEE Photovoltaic Specialist Conf. (1996), p. 793.

ZnSe

W.Eisele et al., XPS, TEM and NRA Investigations of the Cu(In,Ga)(S,Se)$_2$/ZnSe Het-

erostructure for Highly Efficient Solar Cells, (1) In Proc. 12^{th} International Photovoltaic Science and Engineering Conf. (2001), p.371; (2) In Proc. 28^{th} IEEE Photovoltaic Specialist Conf. (2000), p.692.

A.Ennaoui et al., Cd-Free $Cu(Ga,In)(S,Se)_2$ Thin Film Solar Cells and Mini-modules, In Proc. 16^{th} European Photovoltaic Sol. Energy Conf. (2000), p.682.

L.Olson, W.Addis, D.Huber, Investigation of Polycrystalline Thin Film $CuInSe_2$ Solar Cells Based on ZnSe Windows, In Proc. 23^{rd} IEEE Photovoltaic Specialist Conf. (1993), p.603.

F.Engelhardt et al., Interface Characterization of $Cu(In,Ga)Se_2$ Solar Cells Containing a New ZnSe Buffer Layer, In Proc. 2^{nd} World Conf. Photovoltaic Energy Conversion (1998), p.1153.

Y. Ohtake et al., Development of $ZnO/ZnSe/CuIn_{1-x}Ga_xSe_2$ Thin-Film Solar Cells with Band Gap of 1.3 to 1.5 eV, In Proc. 24^{th} IEEE Photovoltaic Specialist Conf. (1994), p.218; In Proc. 13^{th} European Photovoltaic Sol. Energy Conf. (1995), p.2088.

(In_xSe_y)
K. Mitchel et al., Single and Tandem Junction $CuInSe_2$ Cell and Module Technology, In Proc. 20^{th} IEEE Photovoltaic Specialist Conf. (1988), p. 1384.

A.Rumberg et al., ZnSe Buffer Prepared by Iodine Enhanced Chemical Vapour Deposition for CIGSS Based Solar Cells, In Proc. 12^{th} International Photovoltaic Science and Engineering Conf. (2001), p.89.